



Universiteit
Leiden
The Netherlands

Magnetism of a single atom

Otte, A.F.

Citation

Otte, A. F. (2008, March 19). *Magnetism of a single atom*. *Casimir PhD Series*. LION, AMC research group, Faculty of Science, Leiden University. Retrieved from <https://hdl.handle.net/1887/12660>

Version: Corrected Publisher's Version

License: [Licence agreement concerning inclusion of doctoral thesis in the Institutional Repository of the University of Leiden](#)

Downloaded from: <https://hdl.handle.net/1887/12660>

Note: To cite this publication please use the final published version (if applicable).

MAGNETISM OF A SINGLE ATOM

ISBN 978-90-8593-039-6

Casimir PhD Series, Delft-Leiden, 2008-01

Printed by Optima Grafische Communicatie, Rotterdam – www.ogc.nl

Cover: Topographic STM image (50×50 nm) of individual manganese, iron and cobalt atoms evaporated onto islands of copper-nitride on a copper crystal.

MAGNETISM OF A SINGLE ATOM

PROEFSCHRIFT

TER VERKRIJGING VAN
DE GRAAD VAN DOCTOR AAN DE UNIVERSITEIT LEIDEN,
OP GEZAG VAN RECTOR MAGNIFICUS PROF. MR. P. F. VAN DER HEIJDEN,
VOLGENS HET BESLUIT VAN HET COLLEGE VOOR PROMOTIES
TE VERDEDIGEN OP WOENSDAG 19 MAART 2008
KLOKKE 16:15 UUR

DOOR

ALEXANDER FERDINAND OTTE

GEBOREN TE EDE
IN 1979

Promotiecommissie

- Promotor: Prof. Dr. J. M. van Ruitenbeek
- Copromotor: Dr. A. J. Heinrich
IBM Research Division, San Jose, USA
- Referent: Prof. Dr. L. M. K. Vandersypen
Technische Universiteit Delft
- Overige leden: Dr. C. F. Hirjibehedin
London Centre for Nanotechnology, UCL, UK
- Prof. Dr. J. Aarts
- Prof. Dr. J. W. M. Frenken
- Prof. Dr. J. van den Brink
- Dr. Ir. T. H. Oosterkamp
- Prof. Dr. L. J. de Jongh

Contents

Introduction	7
1 ^3He Scanning Tunneling Microscope Design	11
1.1 Heliox ^{UHV} ^3He Refrigerator and Cryostat	12
1.1.1 Cooling Mechanism	12
1.1.2 Large-Scale Assembly	14
1.1.3 Suspension and Access to the Scanner	16
1.2 STM Head	18
1.2.1 Walker Design	18
1.2.2 Electronics and Dynamics	20
1.3 Performance	22
1.3.1 Superconducting Gap	22
1.3.2 Piezo Calibration	24
1.3.3 Tentative Assessment	25
1.4 Joule-Thomson Refrigerated ^3He STM	26
2 Probing Atomic Spin States	27
2.1 Spin Excitation Spectroscopy	27
2.2 Object of Study	28
2.2.1 Sample Preparation	28
2.2.2 Tip Preparation	29
2.3 Experimental Techniques	30
2.3.1 Measurement Procedure	30
2.3.2 Chemical Identification	30
2.3.3 Vertical Atom Manipulation	32
3 Magnetic Anisotropy	35
3.1 Introduction	35
3.2 Cu_2N : a Molecular Network	37
3.3 Anisotropy in Spin Excitations	39
3.3.1 Mn: a Weak Easy-Axis	40
3.3.2 Fe: Almost a Bit	42
3.3.3 Transition Intensities	42
3.4 Discussion	46

4	The Kondo Effect of a Single High-Spin Atom	49
4.1	Historical Overview	49
4.1.1	Anderson $S = \frac{1}{2}$ Impurity Model	49
4.1.2	Experimental Realizations of a Single Kondo Spin	51
4.2	The Kondo Effect of Co on Cu ₂ N	52
4.2.1	Temperature Dependence	52
4.2.2	Why Co is Kondo-Screened	55
4.3	A Kondo Spin and Its Environment	58
4.3.1	Anisotropic Field Dependence	59
4.3.2	Coupled Kondo Systems	62
4.3.3	Full Heisenberg Model	67
4.4	Discussion	78
5	Initial Results on Further Experiments	81
5.1	Distance Dependence of Spin Interaction	81
5.2	Coupling Along the N-Row	87
5.2.1	The Ising Chain: Ferromagnetic Coupling?	88
5.2.2	Closure of the Inelastic Channel	90
5.3	Single-Atom Spin Filter	92
5.4	Closing Remarks	95
	Bibliography	97
	Samenvatting	103
	Curriculum Vitae	109
	List of Publications	110
	Acknowledgements	111

Introduction

But I am not afraid to consider the final question as to whether, ultimately — in the great future — we can arrange the atoms the way we want; the very atoms, all the way down!

R. P. Feynman

Little could he know, when Feynman gave his classic lecture at the 1959 Annual Meeting of the American Physical Society [1], that this ‘great future’ was only just over 30 years away [2, 3]. And great it is. The two and a half decades following the Nobel Prize winning invention of the Scanning Tunneling Microscope [4] have not only witnessed the first demonstration of artificial atom arrangement (or atom *manipulation*, as it was eventually called), they also brought some of its incredible creations, including an atomic ‘fence’ for confining surface electrons [5] and an early dynamic molecular computer [6]. Having achieved such meticulous control over the atoms themselves it is only natural to ask the next question: can we also control the intrinsic properties of an atom? Here we will focus on one such property: the magnetism of a single atom.

Although magnetism, in the sense of a material property, has been around for technological purposes since medieval times (and even much longer than that as a topic of scholarly debate), its origin can be traced all the way down to the atomic scale. Whether a material is magnetic depends on whether each of its constituent atoms is magnetic. Further classifications such as ferro-, antiferro- or paramagnetism indeed do relate to the way the atoms interact and are oriented with respect to each other on a larger scale, but the overriding requirement for a material to be magnetic is that its atoms be magnetic.

Then, what makes an atom magnetic? In quantum-mechanical terms this is determined by the net amount of spin of its electrons. For a filled electronic shell this is zero, but partially filled shells should in principle always have a non-zero net spin according to Hund’s rules. When the atom binds to other atoms – either through covalent bonds in a molecule or through metallic bonds in a lattice – in the case of *s* and *p* orbitals this net spin is often consumed by the formation of these bonds. Having more closely localized orbitals, many *d* and *f* materials are indeed found to be magnetic. This demonstrates the enormous significance of spin: while its algebra is so simple and elegant as to serve in numerous textbook examples of basic quantum mechanics, the electron spin is responsible for all solid-state magnetism and plays a crucial role in chemistry.

Apart from its fundamental relevance, spin draws much attention as it is proposed as a candidate for carrying information in many designs of future computation and data-storage devices [7, 8]. Therefore, many experiments in condensed matter are aimed at (1) isolating a single spin, (2) finding a way to determine its orientation, i.e. ‘reading’ it and (3) manipulating its orientation or ‘writing’ it. Each of these steps has been achieved separately in nanofabricated heterostructures, where individual electrons are confined on artificially crafted two-dimensional quantum dots – a field that has great potential for eventually harnessing the electron spin for technological purposes [9, 10].

Yet, in order to be able to study a spin in a more natural environment, e.g. as a magnetic impurity interacting with a metal, one would have to have access to individual magnetic atoms. A tool that is very well suited for this task is magnetic resonance. Although conventional Nuclear Magnetic Resonance (NMR) and Electron Spin Resonance (ESR) – where one measures the absorbance of RF-radiation incident onto a sample – are only sensitive enough as to detect large ensembles of spins, some ingenious methods were developed that convert this technique into detecting a single spin. One of these methods is based on combining ESR with the Scanning Tunneling Microscope (STM) [11]. In this experiment a resonating spin, oscillating at the Larmor frequency, produces a specific AC-signal in the tunneling current. Another beautiful experiment exists by the name of Magnetic Resonance Force Microscopy (MRFM) [12], where the polarization of a spin is recognized by its effect on the oscillating frequency of a magnetic cantilever. In this configuration the spin can be ‘written’ by means of well-timed RF-pulses.

A fully electronic way of spin readout is provided by the field of spin-polarized STM, where magnetic tips are used to filter out one spin polarization from the tunneling electrons [13, 14]. Although single spin resolution has not yet been obtained with this technique, it has developed into a standard tool for investigating magnetism on the nanoscale.

In this thesis I present a study of atomic spins by means of the *excitations* that can be induced in them. For this purpose we use an adoption of a technique named Inelastic Electron Tunneling Spectroscopy (IETS), which is known best for its strength in detecting vibrational modes in ensembles of molecules trapped within a planar junction [15]. Its principle is based on observing small changes in the conductance of the junction at those voltages where the tunneling electrons have just enough energy to perform specific inelastic (in this case vibrational) excitations. Single molecule resolution has been obtained in an STM configuration [16] and later by means of a Mechanically Controllable Break-junction (MCB) [17].

Only recently did similar spectroscopic analysis of inelastic excitations become accessible on atomic spins [18] and structures consisting of multiple atomic spins [19]. When used for these purposes we will refer to the technique as *Spin Excitation Spectroscopy* (SES). This tool forms the basis for many new experiments described throughout this thesis. The outline of the thesis is as follows.

In **chapter 1** we review the technical equipment needed for high energy resolution SES measurements: an STM cooled to liquid ^3He temperatures, capable of generating high magnetic fields. Specifically we will discuss one such experimental set-up located at the Leiden Kamerlingh Onnes Laboratory, in the development of which I have been involved for several years. Although nearing completion, this apparatus is not yet in a proper condition for performing SES. Experiments presented in subsequent chapters were all carried out in a different ^3He STM system based at the IBM Almaden Research Center.

Chapter 2 gives a detailed description of the experimental techniques used, as well as a characterization of the specific system of choice for our experiments: magnetic d -shell atoms evaporated onto a monolayer of copper-nitride (Cu_2N) on $\text{Cu}(100)$. We will focus on the principles of SES and the possibilities of atom manipulation on this specific surface.

Chapter 3 is devoted to the magnetic anisotropy that an atomic spin experiences when it is placed onto a surface. Anisotropy is what makes a spin align (or *magnetize*) in a certain direction; a property that is of great importance for technological reasons such as non-volatile magnetic data storage. By placing manganese (Mn) and iron (Fe) atoms onto Cu_2N and following the evolution of their spin excitations as magnetic fields are applied in various directions, we find that this surface forms a strongly anisotropic environment for the spins of these atoms [20]. A comparison of the results to Density Functional Theory (DFT) calculations suggests that this may be explained in terms of the atoms being incorporated into a surface molecular network.

In **chapter 4** a third atom species is studied: cobalt (Co). In sharp contrast to both Mn and Fe, measurements performed on Co indicate the appearance of a remarkable resonance which we attribute to the Kondo effect: a many-body effect arising from the interaction of a localized spin with a bath of electrons. A brief introduction into this effect is given at the beginning of the chapter. Based on an analysis along the lines of chapter 3 we present an interpretation as to why this resonance occurs specifically on Co. We show that the magnetic anisotropy of the Cu_2N surface plays a crucial role in the question as to whether a spin becomes Kondo-screened or not. We conclude this chapter by investigating the effects of spin-coupling on the Kondo effect by placing other magnetic atoms close to the Co atom. An analytical model is presented, combining anisotropy, spin-coupling and the effect of a magnetic field, with which we can identify each excitation occurring on these structures with astounding precision.

Finally, **chapter 5** offers a future perspective. Several additional studies were initiated from which no clear conclusions can be drawn at this point. Yet a first step in their analysis is presented which may be useful in designing further experiments. These studies include an investigation into the physics behind the mechanism of spin-coupling on Cu_2N as well as an attempt to create a spin-polarized tip by picking up a single magnetic atom.

Each of these experiments provides new insights into the physics of atomic scale magnetism that are of importance for scientific as well as technological reasons. But above all they are fun. Never before did we have such an incredible degree of control over individual atoms and their spins. It enables us to perform the most basic experiments that one could think of doing with atomic magnets, and almost all of the spin excitations encountered while doing them can be modelled extremely well by elementary quantum mechanics. Few experiments can be as suited to get a *feel* for the peculiar quantum mechanical property named ‘spin’ as the ones described here.

Chapter 1

^3He Scanning Tunneling Microscope Design

At school the bully always picks the smallest kid as his victim. That is because the amount of energy involved in displacing, rotating or deforming a small object is usually less than for larger objects. It is for this reason that Scanning Tunneling Microscopy and cryogenic temperatures form such a natural combination: as the physical scale of the object of study decreases, temperature needs to be reduced in order to keep the experiment controlled.

Today these two techniques are so well integrated that Scanning Tunneling Microscopes (STM's) operating at temperatures as low as 4 K in Ultra-High Vacuum (UHV) are commercially available in reliable and user-friendly configurations. While this temperature range is mostly sufficiently low to disable *atomic* motion, it is still too high for many studies of *electronic* behavior. For example, as we will see in the course of this thesis, electron spin excitations often occur at energies of only a few meV such that small variations cannot be discerned above ~ 1 K. Additionally, various fascinating macroscopic phenomena such as superconductivity and the Kondo effect in some situations have critical or typical temperatures that are well below 4 K. For the purpose of studying these and other situations it is desirable to further cool down an STM with help of liquid ^3He .

In this chapter we will discuss two experimental STM systems that are designed to operate at or below 500 mK in UHV, and are each equipped with a superconducting magnet that can generate a magnetic field up to 7 T or higher. Sections 1.1 through 1.3 give a detailed description of a set-up that is currently under construction in the Kamerlingh Onnes Laboratory in Leiden, based on an Oxford Instruments Heliox^{UHV} ^3He refrigerator. This system is very similar in design to the facility described in [21]. In section 1.4 we will more briefly review an existing system, located at the IBM Almaden Research Center in San Jose, CA, that was used for the experiments described in the remainder of this thesis.

1.1 Heliox^{UHV} ³He Refrigerator and Cryostat

During operation the Heliox^{UHV} ³He refrigerator shown in fig. 1.1, a commercial product of Oxford Instruments plc, is suspended within the UHV central tube of a ⁴He cryostat with liquid N₂ outer shield. The He dewar has a total capacity of 69 ℓ, however in order to guarantee the magnet to maintain its superconducting state, the effective volume is reduced to 51 ℓ. At standard boil-off rate, specified for this cryostat to be ≤ 0.83 ℓ/h, this corresponds to a hold time of at least 61 hours. The N₂ can, with 52 ℓ capacity, is specified to hold for 130 hours.

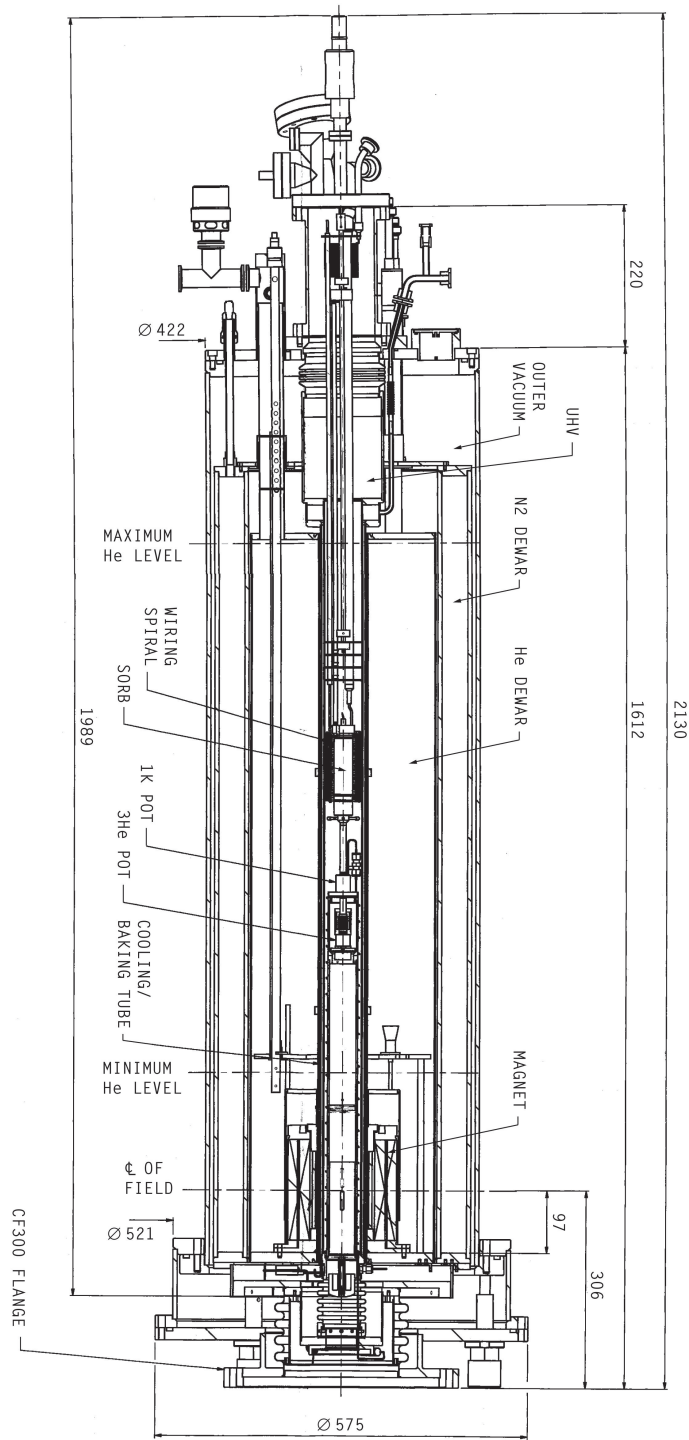
The superconducting magnet can generate a field of 10 T along the cryostat's vertical axis. Running the full current of 114 A through the dissipative leads (when ramping the field) gives rise to an additional 1.4 ℓ/h ⁴He boil-off. The size of the magnet's bore limits the central UHV tube to an inner diameter of 46 mm. The tube has a hollow wall through which liquid ⁴He can be pumped in order to cool it down to ~ 1.8 K, however, this only serves as a cold radiation shield and is not thermally coupled otherwise to the refrigerator.

1.1.1 Cooling Mechanism

Other than providing shielding, the cryostat does not directly cool the Heliox^{UHV} insert. Refrigeration occurs through a separate mechanism which is depicted schematically in fig. 1.2. The flow process can be divided into a ⁴He part and a ³He part, the latter of which is enclosed by a dashed line in the scheme.

We start with the ⁴He part. A spiralled capillary (“A”) carries liquid helium from the bottom of the dewar to a 1K pot. Its flow can be regulated by an electrically driven needle valve mounted close to the beginning of the line. By an external pump the vapor above the liquid accumulated in the 1K pot is pumped through a second, much wider spiralled capillary (“B”). As a result the liquid in the pot cools down to ~ 1.8 K. During normal operation the needle valve is set to maintain a flow of approx. 4 ℓ/min gas through the pump (approx. 9 ℓ/min during initial cool down to 4.2 K). A bypass in the pumping line cools a sorption pump which is part of the ³He flow system. Additionally, there is a strong thermal coupling between the 1K pot and part of the ³He line. Except for radiation these are the only thermal connections between the two parts of the process.

Figure 1.1: (*Opposite page*) Technical drawing of the Heliox^{UHV} refrigerator and accompanying cryostat (cross-section). All dimensions in mm. The insert is drawn in its retracted position. A 1K shield, extending from the 1K pot down to the bottom of the 1989 mm insert length indicator, encompasses everything that should reach the 350 mK base temperature. Thereof only the ³He pot is part of the commercial assembly; the rest (i.e. STM head and suspension, not shown here) was built and developed in our laboratory. With the insert retracted and the suspension in its equilibrium position, the STM scanner is designed to have the junction in the central plane of the magnetic field. Reprinted with permission from Oxford Instruments plc.



In contrast to many comparable systems, in our case the ^3He part of the flow system has a linear configuration (rather than looped) and can therefore only be used in single-shot mode (as opposed to continuous flow mode). At the end of the line it has a 4.5ℓ ^3He reservoir originally filled to a pressure of 1 bar. During the initial cool down stage its gate valve is kept open such that the gas can freely roam through the line. As the 1K bypass cools the charcoal filled sorption pump (hereafter referred to as *sorb*) below approx. 40 K, ^3He gas becomes bound such that the pressure in the reservoir decreases. When the reservoir is (almost) empty, the gate valve is closed; now most gas is trapped in the sorb.

Next the sorb is gently heated to a temperature just above 40 K such that the gas is released and the pressure in the line increases. For safety a relief valve is fitted to allow gas back into the reservoir if the pressure exceeds 3.5 bar, although in practice it is easy to stay below this point. The ^3He now acts as a contact gas between the portion of the line that is linked to the 1K pot and the ^3He pot that is mounted below it, thus slowly cooling it down. When it reaches 3.2 K – depending on the heat load attached to the ^3He pot (e.g. the STM head, wiring etc.) this may take many hours – the gas starts to condense and liquid accumulates in the ^3He pot. After 30 to 60 minutes all gas has been condensed.

The final stage of the cooling procedure consists of switching off the sorb heater and tuning the 1K flow such that the sorb stays cold and acts as a pump. Eventually this cools down the liquid ^3He to its base temperature (approx. 350 mK). The hold time of this single-shot mode is approx. 20 hours, after which the ^3He should be recondensed by once more heating the sorb.

Throughout the process the temperature can be probed at various stations. The sorb is fitted with a 100Ω Allen-Bradley resistor thermometer (range 2 – 300 K), while the 1K pot temperature can be monitored by a $2.2 \text{ k}\Omega$ RuO_2 thick film resistor (range 20 mK – 8 K). The ^3He pot is equipped with one of each type (Allen-Bradley and RuO_2) such that the full range of operating temperatures is covered. Finally, in the housing of the STM scanner itself a CERNOXTM thermometer (range 300 mK – 100 K) is mounted. Additional heaters are installed on the 1K and ^3He pots to precisely regulate their temperatures if desired.

1.1.2 Large-Scale Assembly

At the bottom of the cryostat a CF300 flange (300 mm inner diameter, copper gasket sealed) connects to a home-built 420 mm deep UHV chamber that is pumped by a $300 \ell/\text{s}$ ion-pump. A pair of copper doors connected to the N_2 dewar thermally shield the refrigerator from room temperature radiation. Via an external motor drive unit the Heliox^{UHV} insert can be extended by 476 mm such that it reaches the bottom of the chamber. The radiation doors are pushed open by the insert and close automatically through a spring mechanism upon retracting the insert back into the cryostat. Using a manipulator stick the user can manually replace sample carriers (or tip carriers; in this STM system these are identical and interchangeable) on the STM scanner. In section 1.1.3 we will discuss how the scanner can be accessed for this operation.

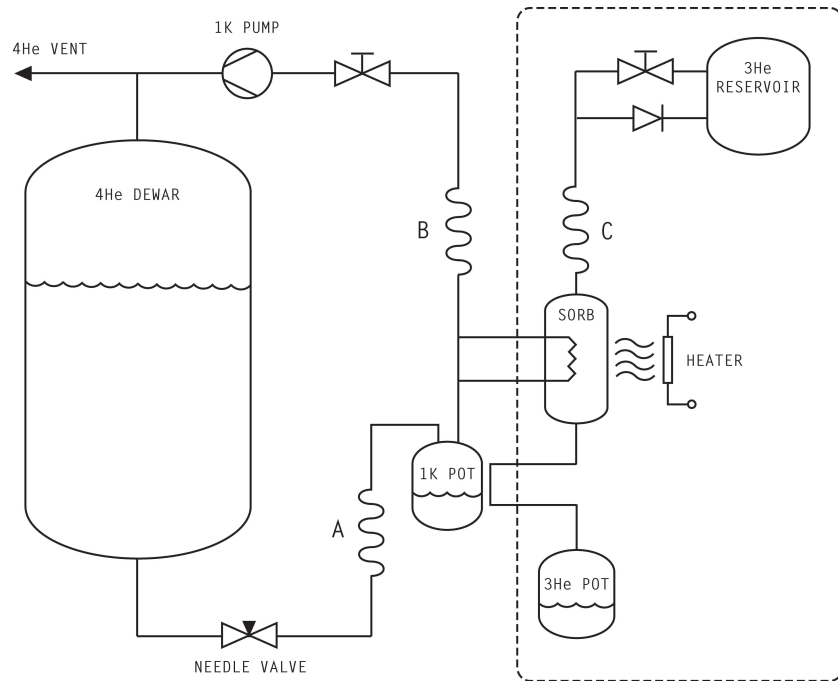


Figure 1.2: Flow diagram of the Heliox^{UHV} ³He refrigerator. The dashed line encloses the ³He part of the process to distinguish it from the ⁴He part. If the insert is extended in order to lower the STM into the main UHV chamber, spiral “A” is contracted whereas “B” and “C” are elongated.

In the main vacuum chamber up to 14 sample carriers can be stored in a fixed holder. Alternatively, samples can be transferred to a preparation chamber on a horizontal translator that can accommodate five carriers at once. Preparation techniques currently installed are a SPECS[®] IQE 11/35 ion-sputtering gun (0.2 – 5 kV) and a sample annealing station (approx. 600°C maximum). The preparation chamber additionally serves as a load-lock for adding new samples to the system and is pumped by a 60 ℓ/s turbo pump, which is also used for initial pumping of the total vacuum system (i.e. load-lock, main chamber, ion-pump and UHV part of cryostat).

The entire assembly is mounted in a rack that rests on four actively damped pneumatic pillars, two of which share one pressure regulator such that the system effectively rests on three points that move independently. The height of these points (i.e. the height of the top of the pillars) corresponds approximately to the height of the CF300 flange. The pillars stand on top of a separate ~ 10 tons concrete foundation, shared with one other experimental set-up, that is acoustically disconnected from the surrounding building.

1.1.3 Suspension and Access to the Scanner

Apart from the concrete foundation and the air-cushioned pillars there is a third step of vibration isolation. The STM head itself is attached to an approx. 25 cm long spring hanging freely below the ^3He pot. As shown in fig. 1.3, the spring hangs inside a gold-plated copper ^3He shield (that is named after the temperature it is supposed to assume). In order to ensure proper cooling of the scanner without creating an acoustic link, a copper ring is clamped to the inside of the shield. The suspension rod that holds the scanner assembly is connected to this ring by two bundles of approx. 250 flexible 0.05 mm \varnothing copper wires (not shown in the drawing to avoid cluttering) that are long enough not to generate any tension if the rod moves up or down.

Wires coming from the scanner pass through the copper ring and are then led through holes in the ^3He shield to proceed upward spiralling along the outside of the shield. Over a total length of approx. 35 cm they are glued onto the shield to provide a thermal anchor. For this purpose low vapor pressure glue is used, although as the shield is meant to be kept at cryogenic temperatures, contamination by degassing will in any case be strongly reduced.

The STM head, which will be described in detail in section 1.2, is mounted inside a 36 mm outer diameter gold-plated copper housing. After disconnecting all wires from the MACOR[®] connector plate, the entire housing can be easily removed from the suspension rod for repairs or alterations. Six ruby balls on the outside ensure that the contact area of the housing eventually touching the warmer shield around it is reduced to no more than a point. A threaded ring at the bottom of the housing is used to tightly clamp the scanner.

The 1K shield enveloping the parts mentioned above actually consists of two coaxial shields. The bottom of the outer shield is rounded for properly opening the N_2 -temperature radiation doors when the insert is lowered into the main chamber. This shape also acts as a 'seeker' when the insert reaches a metal cup it is supposed to rest in at the bottom of the chamber. In the center of this cup a rotatable 'screwdriver' protrudes upward that fits into a screw head that is part of the inner 1K shield. This stops the downward motion of the inner shield such that it rises with respect to the outer shield. As a result it pushes the STM scanner against the ^3He shield, which thus becomes fixed for transfer of sample carriers.

Both the inner and outer shields have windows that align vertically only if the inner shield is at its highest position with respect to the outer shield. By rotating the screwdriver the user can make them align horizontally as well. This provides access to the scanner for the manipulator stick. A spring between the two shields ensures that the window properly closes again once the insert is retracted into the cryostat. The screwdriver supporting the inner shield which in turn pushes the scanner against the ^3He shield creates a direct thermal connection between the ^3He pot and ambient temperatures. An experienced user can perform a complete tip and sample exchange in about 10 minutes. The heat that is thus introduced (through the screwdriver, the new sample carriers and radiation) necessitates an additional cooling time of several hours.

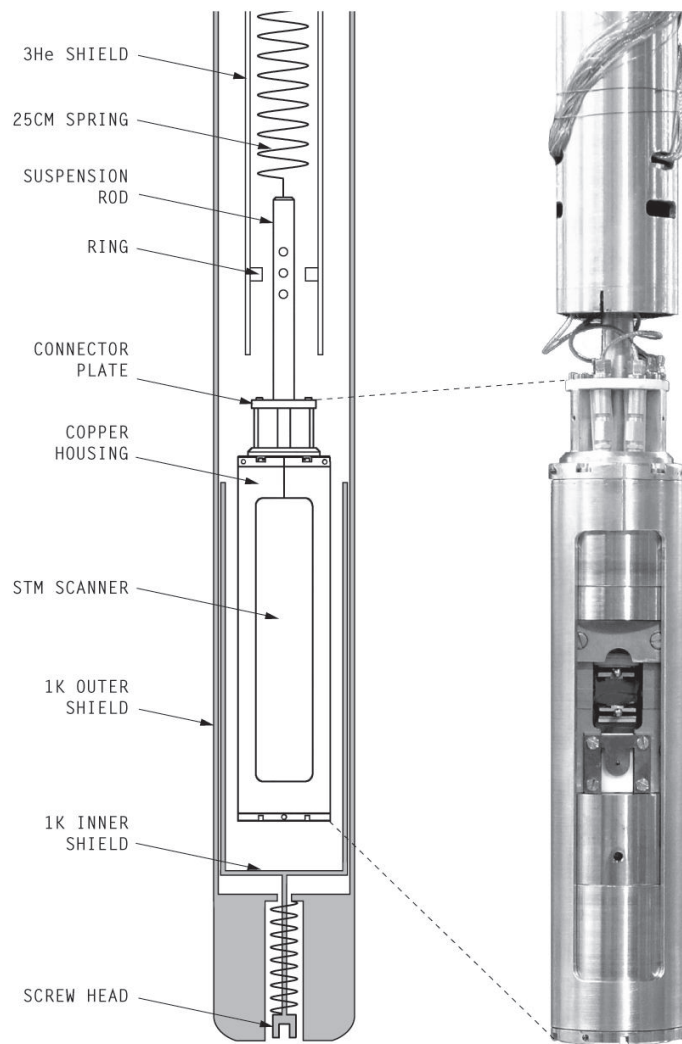


Figure 1.3: **Left:** Schematic drawing of the suspension of the STM scanner (not to scale). Parts that are colored white are thermally anchored to the ^3He pot, while grey parts are attached to the 1K pot. Bundles of copper wires connecting the suspension rod to the clamping ring, as well as the wires coming from the scanner are left out to avoid cluttering. **Right:** Photograph of the scanner mounted to the refrigerator. The 1K shields are not shown in the picture.

1.2 STM Head

¹ The STM head currently used is a home-built device with a walker-type coarse approach mechanism based on a design by Pan *et al.* [23], which is a reliable concept that is used in several comparable systems [21, 24]. Where most STM's of this type have a tube scanner mounted onto the slider that performs the scanning once the tip is in tunneling range, in the current design feedback is done by the same piezo actuators that are used for the coarse approach.

1.2.1 Walker Design

Figure 1.4 shows an expanded drawing of the assembly. Due to the dimensions of the copper housing mentioned in section 1.1.3 it is shaped as a 33 mm \varnothing cylinder. The main body is made of titanium for reasons of thermal expansion: in a design like this it is desirable to have all components expand roughly equally such that at any temperature all relative dimensions are the same. All piezo actuators used are stacked shear-elements from the PICATM-Shear series of PI Ceramic which have a coefficient of linear thermal expansion $\alpha = 4 - 8$ (in units of 10^{-6}K^{-1}) perpendicular to the polarization direction, whereas Ti has $\alpha = 8.6 \times 10^{-6}\text{K}^{-1}$.

Four X-shear piezo actuators² (3×3 mm, 5.5 mm high), each capped with a pad of aluminium-oxide (Al_2O_3), are glued onto the titanium body in two pairs that make an angle of 120° with each other. These support a 30 mm long prism-shaped walker (again made of titanium for the same reason), the sides of which have been polished and coated with titanium-carbide (TiC). Two additional X-shear actuators, identical to the others, are glued onto a small beam of MACOR[®] which is pushed down onto the walker by a 0.1 mm thick phosphorous-bronze leaf spring. To guarantee a point-like force at the center of the beam, a 1.5 mm \varnothing ruby ball is placed between the leaf spring and the beam. All actuators were glued into the assembly using STYCAST[®] 1266 A/B (a clear two-component epoxy). While baking the glue (1 hour at $60 - 70^\circ\text{C}$), the actual walker prism was used to apply pressure such that the surfaces would end up perfectly parallel ensuring maximum contact area.

Since the feedback (i.e. scan direction z) is taken care of by the same set of actuators, no tube scanner is required. Instead, a tip/sample station is glued directly onto the walker (separated by a thin MACOR[®] plate for insulation). Horizontal scanning (the x and y -directions) is done by a $10 \times 10 \times 9.5$ mm XY-shear stack glued onto a separable part of the body, also with a tip/sample station directly mounted onto it. Depending on whether the stations are occupied or not, the walker has a walking range of approx. 1.0 – 1.5 cm. In order to prevent a tip crash in case of the piezo stacks eventually losing grip on the walker the STM head is intended to be mounted with the XY-stack on top, although in principle it could work either way.

¹A general introduction into the principles of STM can be found in [22].

²Here the 'X' indicates that the piezo elements have only one direction of displacement as opposed to XY or XYZ-shear piezo actuators. It does not signify a specific direction in the coordinate frame of the scanner.

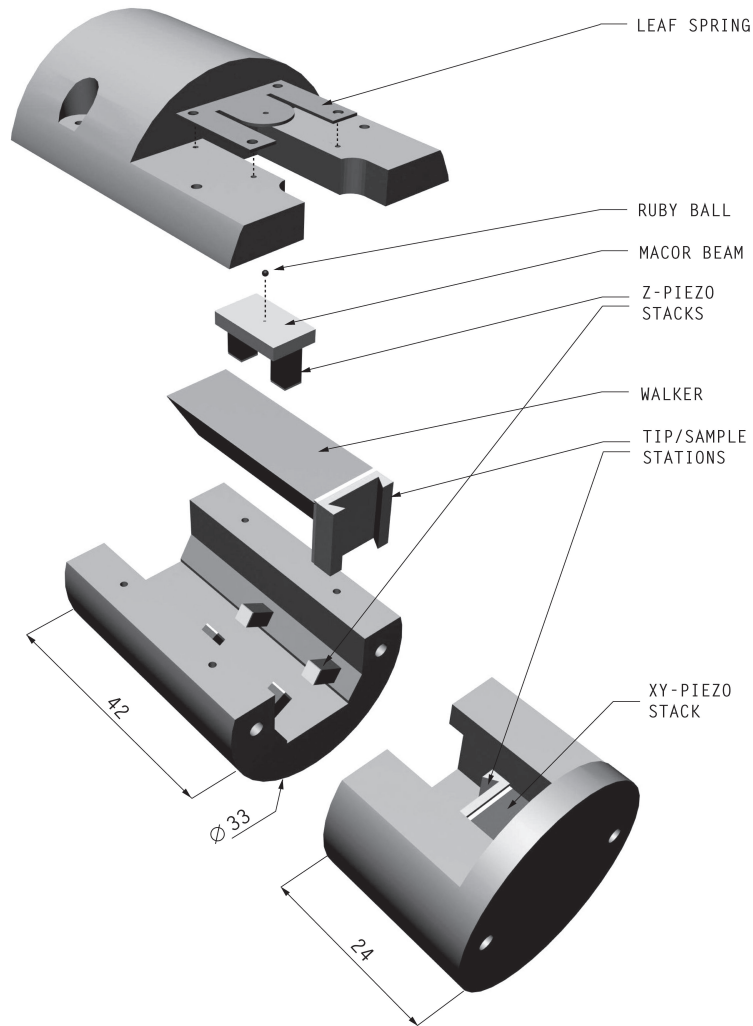


Figure 1.4: Expanded rendered drawing of the home-built Pan-design STM head. All dimensions in mm. The body, as well as the walker and the tip and sample stations are made of titanium; the walker is additionally coated with TiC. All piezo actuators are capped with an Al_2O_3 pad. The leaf spring consists of phosphorous-bronze. A thin insulating plate separates the walker electrically from the station glued onto it.

In figure 1.5 the sample mounting mechanism is demonstrated: a sample carrier fits onto a station through a dovetail joint (both are made of titanium). After sliding it in place it is pushed upward by a bent phosphorous-bronze leaf spring. This not only fixes the carrier but also ensures a strong thermal and electrical connection. A 9×9 mm object table provides ample space for

mounting samples, although only a very small portion of it can be scanned as no coarse movement in the x and y -directions is allowed for. Tip carriers are identical to sample carriers except for an additional 0.3 mm \varnothing hole in the center of the table. Tips mounted in the hole are fixed in place by a small screw in the body of the carrier.

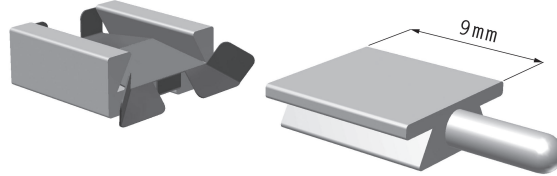


Figure 1.5: Sample station (left) and carrier, each made of titanium, form a dovetail joint. A phosphorous-bronze leaf spring holds the carrier in place.

1.2.2 Electronics and Dynamics

Two stainless steel coaxial cables run down from the top of the insert to the tip and sample electrodes. Spiralling down along capillary “B” of fig. 1.2, their length is set to approx. 6 m corresponding to a capacitance of 1.2 nF each. Directly at the top of the insert the measurement signal is amplified by a Stanford Research Systems Inc. SR570 pre-amplifier, which combined with the input impedance of the wires has a noise level of ~ 0.3 pA/ $\sqrt{\text{Hz}}$ at 10^{-9} A/V sensitivity. Feedback and scanning is performed by an RHK Technology Inc. SPM 100 controller with accompanying software.

Coarse Approach

The coarse approach piezo motor has been demonstrated to function properly at temperatures down to 350 mK in inertia-mode. In this mode all six piezo actuators are operated simultaneously. The actuators have a combined capacity of 8.6 nF and are specified to each have a total displacement of $3 \mu\text{m}$ ($\pm 30\%$) over a voltage range of 500 V at room temperature; at low temperature this reduces to approximately $0.35 \mu\text{m}$ (see section 1.3.2). They are driven by half parabola voltage pulses that in an automated approach are alternated by slow voltage ramps to check for tunneling current (see fig. 1.6); during the initial manual approach these are omitted to save time. Reliable values at low temperatures are 250 – 500 μs pulse width with an amplitude of 160 V, with a ramp of typically 200 V or higher amplitude and a few hundreds of milliseconds width. Here the leaf spring is bent such that the maximum friction force (i.e. the maximum force one can apply onto the walker before it starts to slide) at ambient conditions is between 0.5 and 0.8 N. At these settings the step size is such that several steps

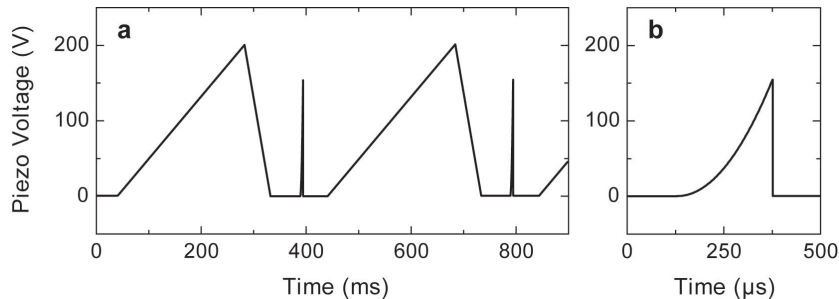


Figure 1.6: (a) Typical pulse train used for an automated approach, consisting of short driving pulses alternated with slow probing ramps. (b) Detailed plot of a driving pulse: a half parabola with a sharp cutoff. Reliable values are 160 V/250 μ s for the pulses, 200 V/200 ms for the ramps. Waiting times \gtrsim 10 ms.

(in the order of ten) fit in the walker’s total z -range. When moving downward the steps are larger than when moving upward by a factor of ~ 1.3 .

Manual approach can be performed while the insert is lowered such that there is visual access to the motor. Depending on how close the user brings the tip to the sample during this stage, the automated approach (performed after the insert has been retracted and the STM has cooled down) takes between 15 minutes and two hours. Between two measurements, e.g. while recondensing the ^3He , the tip is retracted by a few tens of steps such that experiments can be resumed almost immediately.

Walker Resonances

The scanner was designed to have high resonance frequencies in order to improve immunity against external vibrations. According to specifications the X-shear piezo stacks have their resonant frequency at 210 kHz. However, the walker assembly as a whole can have much lower-lying resonances. As these can seriously interfere with the feedback mechanism it is important to chart the motor’s vibrational spectrum. In fig. 1.7 we see such spectra in a range of 1 – 10 kHz; the upper curve corresponds to an ‘empty’ walker (total mass 6.87 g) while the lower was taken after mounting a 0.82 g sample carrier onto the walker. A strong resonance peak shifts downward from 8.4 tot 7.7 kHz upon placing the carrier and can therefore probably be assigned to a vibration mode of the system consisting of the walker being suspended by six piezo stacks. Here the ratio of the frequencies is 1.09 while the square root of the mass changes by a factor of 1.06. A weaker resonance occurs at 5.3 kHz in the upper curve which seems to split into multiple small peaks when the sample is loaded. Although it is more difficult to identify this mode, it could be related to the leaf spring being a free object in one case and becoming clamped in the other. In any case, no significant resonance takes place below an onset of 3.3 kHz which seems to be independent of the walker mass.

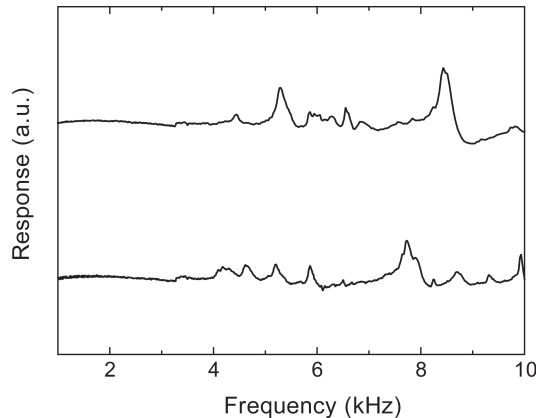


Figure 1.7: Resonance spectra of the six combined X-shear piezo stacks with (lower curve) and without (upper curve) a sample carrier mounted onto the walker, offset with respect to each other. Voltage response is measured over a $100\ \Omega$ resistor connected in series with the piezo elements, driven by a 1 V amplitude AC-signal at frequencies ranging from 1 to 10 kHz (measurements below 1 kHz did not show any resonances). From each curve a smooth background was subtracted. Before this measurement the maximum friction force of the walker was set to 0.75 N.

These resonances are not expected to cause any trouble during scanning. For example, images with a line-resolution of 512 data points can be scanned up to 6 Hz line-frequency before reaching the 3.3 kHz onset and even up to 15 Hz when only considering the main resonance.

1.3 Performance

Although the system is currently not yet fully operational, several test experiments have been performed for characterization and calibration purposes. Here we will review some of their results. All measurements presented were performed with a manually cut 0.25 mm \varnothing platinum-iridium tip (90% Pt, 10% Ir).

1.3.1 Superconducting Gap

The actual temperature of a tunnel-junction can be studied very well using a superconducting sample. For this purpose an α - $\text{Mo}_{2.7}\text{Ge}$ film, covered with a thin gold capping layer, was mounted in the scanner and cooled down. α - $\text{Mo}_{2.7}\text{Ge}$ is a type II superconductor, the critical temperature T_c of which depends strongly on the film thickness d , but saturates around 6.3 K for $d \gtrsim 40$ nm [25]. Measurements of the differential conductance dI/dV were performed at various temperatures, two of which are shown in fig. 1.8: at 2.5 K and 400 mK as indicated on the thermometer that is mounted in the body of the STM head (the latter value corresponds to the base temperature of 350 mK on the ^3He pot).

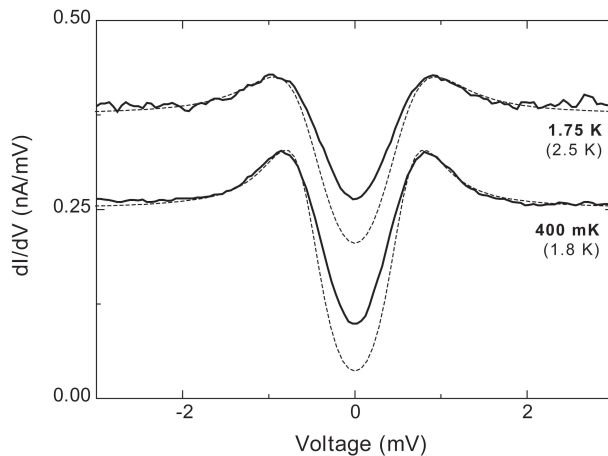


Figure 1.8: Conductance spectra taken on a Au-capped α -Mo_{2.7}Ge film at 1.75 K and 400 mK (as indicated by the thermometer mounted in the STM head) at 80 mV/20 nA quiescent settings. The upper curve is offset by 0.125 nA/mV for clarity. Measurements were performed by lock-in technique (100 μ V AC-modulation at 716 Hz, 20 mV sensitivity, 30 ms integration time). The smooth dashed lines are thermally broadened BCS densities of states at effective temperatures of 2.5 and 1.8 K, manually fitted to the shape of the peaks (rather than to the gap).

The spectra were fitted by hand using the Bardeen-Cooper-Schrieffer (BCS) density of states [26],

$$\frac{\rho_{\text{BCS}}(\varepsilon)}{\rho_0} = \begin{cases} \frac{\varepsilon}{\sqrt{\varepsilon^2 - \Delta^2}} & \text{if } \varepsilon > \Delta, \text{ and} \\ 0 & \text{if } \varepsilon < \Delta, \end{cases} \quad (1.1)$$

being broadened with an effective temperature T_{eff} (see section 4.2.1 for details on thermal and modulation broadening). In the above expression ε is the energy and Δ half the width of the energy gap. The parameters Δ and T_{eff} were manually adjusted to obtain a best fit, resulting in $\Delta = 0.55$ meV for both spectra and $T_{\text{eff}} = 2.5$ and 1.8 K for the high and low-temperature measurements respectively. Using the expression $\Delta = 1.76k_B T_c$ (k_B is Boltzmann’s constant), which applies fairly well for $T \lesssim T_c/2$ [26], we find $T_c = 3.6$ K, corresponding to a layer thickness $d \simeq 10$ nm.

These high effective temperatures can be partly explained by the 0.1 mV AC-modulation signal added to the voltage for lock-in detection, resulting in an extra ‘modulation temperature’ $T_{\text{mod}} = 0.9$ K. Subtracting this we find actual temperatures $T = \sqrt{T_{\text{eff}}^2 - T_{\text{mod}}^2} = 2.3$ and 1.6 K respectively, which are still rather high. Two principal candidates for the source of this discrepancy are (1) inadequate thermal anchoring of tip and sample and (2) insufficient filtering of RF-noise leaking in through the leads.

1.3.2 Piezo Calibration

The x and y scan motions were calibrated by imaging the surface of a highly oriented pyrolytic graphite (HOPG) sample. In fig. 1.9 two images are shown, taken at 600 mK and 2 K. Although technically the 2 K results were used for calibration, sensitivity of the piezo-elements hardly varies at these temperatures. Large scale images such as the one on the left did not show any defects in the

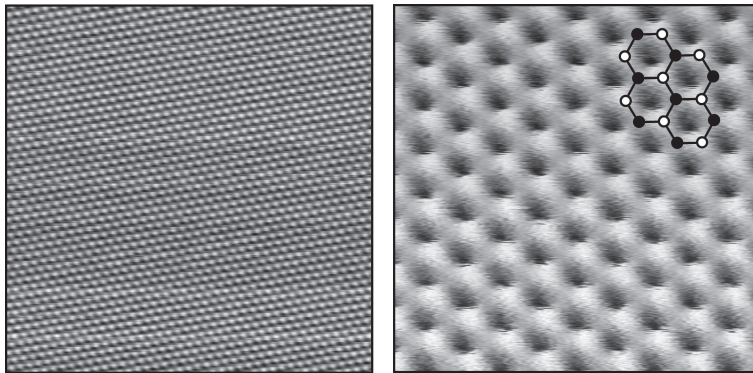


Figure 1.9: STM images of HOPG at 600 mK (**left**, 10×10 nm) and 2 K (**right**, 2×2 nm), recorded with 0.8 V/40 nA. The apparent height is represented in greyscale, with a maximum difference of approx. 5 Å. The overlay on the right image suggests a possible hexagonal lattice assignment.

hexagonal pattern. This might result from scanning with a non-ideal, multiple tip [22]. However, as several independent measurements at portions of the graphite surface with different orientations all produced equal lattice spacings, it is unlikely that the observed patterns result from mere interference between the sample and an eventual flake of graphite on the tip. Also, the resulting piezo calibration of 7.0 Å/V (both for the x and y -directions) agrees reasonably well with the specified sensitivity: 6 nm/V ($\pm 30\%$) at room temperature. With a voltage range of 500 V this gives a total low-temperature scan range of 350×350 nm.

On the right image an overlay indicates a possible identification of the lattice. Here carbon atoms from one sublattice (white circles) appear more brightly than those from the other sublattice (black), resulting from a variation in the local density of states. The correct assignment might be shifted with respect to the presented one, but both the scale and the orientation should be accurate.

Proper calibration of the z -motion, on a stepped surface with a known step height, has currently not yet been performed at low temperatures. However, as the X-shear actuators that move the walker are made of the same piezo-ceramic material as the XY-shear stack that is used for horizontal scanning, we can as a first approximation assume an equal reduction in sensitivity upon cooling down to cryogenic temperatures. This again results in 7.0 Å/V, or a total range of 0.35 μm as suggested in section 1.2.2.

1.3.3 Tentative Assessment

The ^3He STM system described in these first three sections is in an advanced stage of its development. Judging from the successes on an almost identical system [21] it is based on a design that has proven itself and each of the individual components has at some point functioned properly. However, several weaknesses have been detected during the assemblage and testing stages.

- The **1K capillary**, transporting ^4He from the dewar to the 1K pot, has developed leaks into the UHV chamber on multiple occasions. On either end (i.e. at the dewar and at the 1K pot) it is connected by a SWAGELOK VCR[®] fitting, which requires a considerable torque for proper sealing. Since one of these has to be resealed every time the insert is removed from the cryostat, the capillary is permanently at risk of being weakened until it rips.
- Similarly the **^3He capillary**, spiralling down to the sorb, is a notorious source of trouble. Made of copper-nickel, its wall is quite fragile. Repeatedly extending and retracting the insert can cause it to kink, with a blockage as result. It cannot be easily accessed for repairs and once reached it is very difficult to mend reliably. Opening the line leads to expensive ^3He losses and contamination of the sorption pump.
- The **vertical motion mechanism** for lowering the insert into the main chamber has failed several times. It consists of a rotating threaded rod along which a nut (that holds the weight of the entire insert) can move up or down. Friction wears the thread inside the nut until it fails after only tens of runs. MoS_2 powder is supposed to prevent this, but the rod cannot be easily accessed for replenishing the lubricant.

Each of these problems in itself can in principle be evaded by careful handling, but together they cumulatively reduce the chance of a successful measurement and thus weaken the design. In a scientific instrument that is intended to operate at and beyond the boundaries of technology we cannot afford those components that rely on conventional technology to be less than optimal.

All of the issues listed above are in a sense related to the fact that the cryostat is ‘bottom-loaded’: in order for samples to be replaced the entire refrigerator has to move through the vacuum and therefore everything has to be flexible and fragile. Mechanical motion should be avoided as much as possible, especially when the choice of materials is limited by the requirements of UHV and low-temperature compatibility.

The alternative is to make the cryostat accessible from top, such as the system briefly reviewed in the next section. This way the cooling mechanism can remain fixed and only the STM head (or even only the sample) is picked up and transferred to the main chamber above if desired. As an additional advantage, having the He dewar below the suspension enhances stability by lowering the center of mass, not to mention obviating the discomforts and hazards of having to refill a 3 m tall column with liquid helium.

1.4 Joule-Thomson Refrigerated ^3He STM

Built by A.J. Heinrich and coworkers, the ^3He STM system located at the IBM Almaden Research Center is inspired by an earlier design for a 4 K STM by D.M. Eigler. In this top-loaded construction, the scanner assembly permanently stays down in the cryostat while samples can be transferred to and from the preparation chamber via an ~ 150 cm long manipulator rod connected to an almost equally long UHV bellow (tip exchange is currently precluded).

In contrast to many other ^3He refrigerators, here the ^3He gas is cooled by the Joule-Thomson effect [27]. The UHV area, protruding down from the main chamber along the central axis of the cryostat, ends with a glass tube at the bottom of which the STM head is mounted. This glass tube hangs inside an exchange gas can, which is part of a closed ^3He cooling cycle. Gas expands into the can through a nozzle and is pumped through a much wider line, until it condenses and accumulates as a liquid at the bottom of the can. Note that in this system no ^4He -filled 1K pot is required. Other than cooling the superconducting magnet, the only purpose of the ^4He dewar around the can is to serve as a 4.2 K thermal shield.

Three modes of operation can be distinguished:

1. In **static mode**, the can is filled with static ^3He gas (i.e. nozzle and pumping line are closed), thermally linking the He dewar to the STM which thereby equilibrates to 4.2 K.
2. In **continuous-flow mode** the gas is cooled by Joule-Thomson expansion as discussed above. Both the nozzle and the pumping line are opened. This eventually results in a temperature of 1.4 K.
3. Finally the supply of new warm gas can be stopped by closing the nozzle. When being run in this **single-shot mode**, the system can reach 0.5 K.

Using an additional heater mounted in the STM head, intermediate temperatures can be realized, at least on the sample. As a result of the design, both the heater and the thermometer attached to the scanner are strongly coupled to the sample station but hardly to the tip, which is cooled almost directly by the liquid ^3He .

The cryostat is equipped with a superconducting 7 T split-coil magnet. Its field is oriented perpendicular to the cryostat's axis (i.e. horizontal). The field orientation within the horizontal plane can in principle be chosen freely, but is fixed once the cryostat is mounted in place. As the STM head is designed such that the sample stands upright (apart from a $\sim 7^\circ$ tilt), the magnetic field can be oriented either perpendicular or parallel to the sample surface. Switching from one situation to the other involves warming up the system and dismounting the dewar and cannot be done without having to prepare the sample anew.

All experiments presented in the remainder of this thesis were performed on this instrument.

Chapter 2

Probing Atomic Spin States

2.1 Spin Excitation Spectroscopy

Magnetism is carried by the spin of electrons. Therefore, it is electrons that might help us in the task at hand: to access the world of atomic scale magnetism and translate its properties into signals that we can understand. In the work described here, we study individual spin states by means of Inelastic Electron Tunneling Spectroscopy (IETS). This technique focuses on systems that have well-defined energy levels and are situated at a tunnel barrier. At low voltages V electrons flow through such a system elastically. But once eV (with e the elementary charge) exceeds the energy required to make an excitation to a higher level, electrons have the additional option of performing this excitation by tunneling inelastically. From this threshold voltage onward, there will be an extra contribution to the current for every voltage increment dV . This results in a step in dI/dV as a function of V , the height of which depends on the excitation probability and the relaxation time of the system.

Previously, IETS was used in an STM geometry to identify vibrational modes of a single C_2H_2 (acetylene) molecule adsorbed onto a Cu(100) surface [16]. In this case the gap between tip and molecule forms the tunnel barrier. The electrons that tunnel inelastically lose their energy by exciting the stretching mode of the C-H bonds. The resulting dI/dV -step has an intrinsic width of only ~ 8 meV which is very low compared to its energy (around 360 meV) and can therefore be considered well-defined.

If IETS is to be employed to study excitations of a single localized spin state rather than vibrational modes, we will refer to the technique as *Spin Excitation Spectroscopy* (SES). Spin excitations, however, occur at much lower energies. This is largely determined by the magnitude of the externally applied magnetic field in which the experiment is conducted. Since that is experimentally limited to a few Tesla, we can expect most SES features to be found below 10 meV. Furthermore, since the spin state is itself an electron state, its coupling to the electrons in the bulk is likely to be much stronger than that of a molecular

vibration mode. The resulting additional lifetime broadening combined with the low excitation energies makes observation of spin excitations unlikely to occur in magnetic atoms that are placed directly onto a metal surface.

For this reason, SES has so far only been performed successfully on atoms that lie on top of a thin insulating layer that separates them from the bulk. Such a layer has to meet several requirements, the most obvious of which is that it should be thin enough to still enable electron tunneling. But exactly how limited the choice is can best be estimated by considering the lifetime of the excited state, which strongly depends on the coupling strength and hence the layer thickness. On the one hand, in order to clearly resolve multiple excited levels their widths should not be much more than ~ 0.1 meV, corresponding to a relaxation rate $\omega_r \lesssim 100$ GHz. But on the other hand, the excitation events have to occur often enough for it to produce an observable effect. So in order to discern the signal on top of a 100 pA background, the inelastic current should be no less than a few pA, or $\omega_r \gtrsim 100$ MHz. Some materials that are known to meet these requirements are Al₂O₃ on NiAl(110) [18] and Cu₂N on Cu(100) [19]. In a similar fashion, NaCl was found to sufficiently decouple molecular orbitals (rather than spin states) of pentacene from both Cu(111) and Cu(100) substrates [28].

2.2 Object of Study

2.2.1 Sample Preparation

The experiments discussed in this thesis, all carried out in the experimental set-up described in section 1.4, were performed on Cu₂N/Cu(100). To produce this we started with a clean Cu(100) crystal surface that had been prepared with repeated Ar sputter (1 keV, 2×10^{-6} mbar) and anneal ($\sim 600^\circ\text{C}$) cycles, in a base vacuum of 1×10^{-9} mbar. Next, the sample was sputtered for two minutes at 1 keV in 5×10^{-6} mbar N₂ gas, followed by one minute annealing at $\sim 400^\circ\text{C}$. This results in approx. 5 nm wide Cu₂N islands that are one atomic layer thick and roughly square shaped (fig. 2.1a). Since the conductance of the islands is lower than that of the surrounding bare copper, they appear as 0.14 nm deep depressions (fig. 2.1c). The preference for the square geometry is believed to be the result of a mismatch of the Cu₂N lattice with the underlying Cu(100) [29]. Saturated nitrogen coverage of the copper surface causes the islands to arrange themselves in an array like fashion.

After this we transferred the sample into the STM scanner and left it to cool down to liquid helium temperature before evaporating the magnetic atoms. We evaporated three different metals that all exhibit *d*-shell magnetism: Mn, Fe and Co. What evaporation parameters should be used depends strongly on the geometry and temperature distribution of the vacuum chamber and can only be found by trial and error. We tuned the values such that they resulted in an almost equal dose of the three elements with a combined coverage of two to three atoms per island [30].

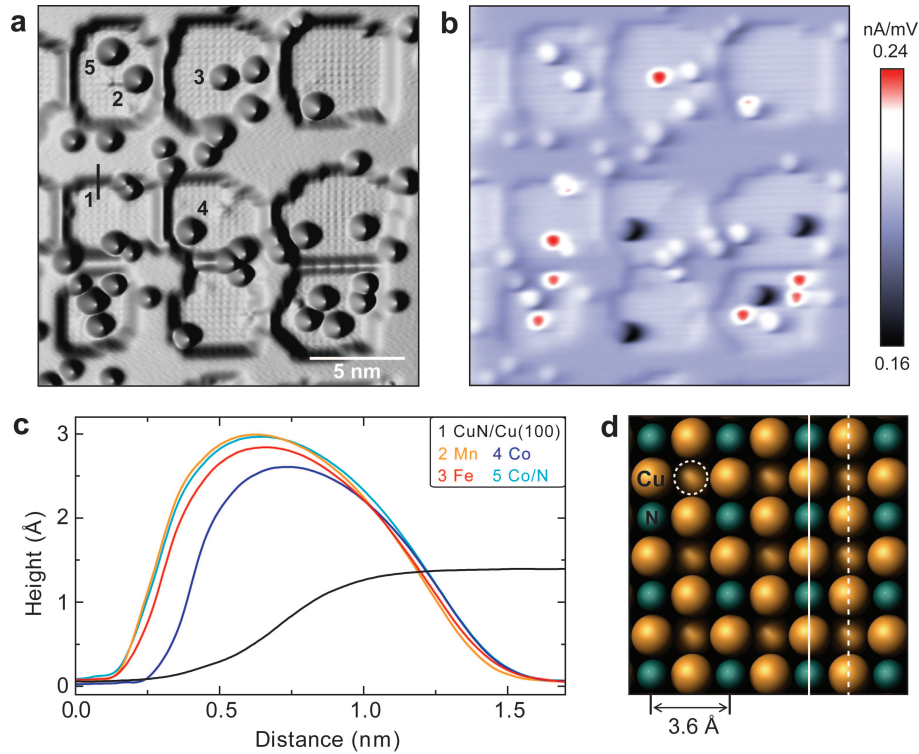


Figure 2.1: (a) STM image (20×20 nm, 1 mV/0.2 nA, 0.5 K) of Mn, Fe and Co atoms on $\text{Cu}_2\text{N}/\text{Cu}(100)$. (b) dI/dV -map taken simultaneously with (a) at $250 \mu\text{V}$ AC-modulation. Fe atoms appear as red and Co as black. Mn atoms and atoms on N sites are white. (c) Height profiles taken from (a), each in vertical direction (upward). (d) Crystal structure of the Cu_2N surface (top view). At the positions of the vacancies (dashed circle) Cu atoms in the second layer can be seen. The solid and dashed lines indicate a N-row and a vacancy-row respectively.

2.2.2 Tip Preparation

The STM tip we used was made out of a pure iridium rod (0.25 mm \varnothing) that was cut to have a somewhat sharp ending. While under vacuum, the tip was taken into field-emission range of a clean Cu sample (1 nA at -300 V tip voltage) and cleaned at $10 \mu\text{A}$ (corresponding to approx. -600 V) until the current became stable (~ 5 minutes, depending on tip cleanliness).

During operation of the STM the tip was further conditioned by indenting (‘poking’) it into the surface. In order to do so we positioned the tip over a region of bare copper in between the Cu_2N islands (at 10 mV/1 nA, i.e. ~ 3 Å tip height), opened the feedback loop and increased the voltage to 2 V. Then we lowered the tip by 10 Å where it stayed for a second after which we reduced the voltage to 1 mV and restored its original height. This procedure could be

repeated until a suitable tip for scanning or atom manipulation (section 2.3.3) was obtained. Hereafter we will refer to the ‘tip’ only as the microscopic object – meaning the last few atoms, presumably Cu – that remains after such poking.

2.3 Experimental Techniques

2.3.1 Measurement Procedure

Unless specified otherwise, all dI/dV -spectra shown in this thesis were taken in single-shot ^3He mode (section 1.4), corresponding to 475 mK indicated on a CERNOXTM thermometer that was mounted directly onto the scanner close to the sample. With the feedback loop closed, the tip was positioned roughly over the center of the atom of interest after which an automated ‘atom-lock’ procedure placed it exactly over the local maximum in the topography. The feedback parameters (typically 10 mV/1 nA, unless stated differently) serve as the quiescent settings for the measurement. Next, the feedback loop was opened and the voltage set to its start-of-sweep value where it stayed for at least one second before commencing the measurement sweep.

We recorded the dI/dV as a function of V by lock-in detection, using an SR830 lock-in amplifier at 200 mV sensitivity, 30 ms integration time. For this purpose a small AC-signal (~ 700 Hz, $50 \mu\text{V}_{\text{rms}}$ unless specified otherwise) was added to the bias voltage. Data was taken with a 16 bit analog-to-digital converter (ADC) for 1024 points in the voltage domain. One sweep (forward and backward) took approx. 2 minutes. After this the tip was relocked onto the atom (with closed feedback at quiescent settings) and the entire process repeated at least once for averaging.

Depending on the sweep rate, the forward and backward scans were slightly offset in voltage with respect to each other. This error was corrected for by shifting them back onto each other after which the forward scan was averaged with its backward counterpart to cancel out potential drift of the tip. During each set of measurements an off-atom spectrum was taken with the same tip on bare Cu or Cu_2N (as discussed above except for the atom-locking) and checked for non-linearities.

2.3.2 Chemical Identification

When working with different kinds of adsorbents simultaneously, one needs a way to tell them apart. As discussed above, vibrational spectroscopy has been used to identify isotope composition within otherwise identical molecules [6, 16, 31]. More recently, chemical identification of Si, Sn and Pb atoms on Si(111) was achieved non-electronically by means of Atomic Force Microscopy (AFM) [32]. In this section we will discuss the identification abilities that SES provides.

Fig. 2.1d shows the crystal structure of Cu_2N on top of Cu(100): a square lattice with a 3.6 Å wide unit cell containing two Cu atoms and one N atom [29]. The square pattern of this atomic structure is also clearly visible on the islands

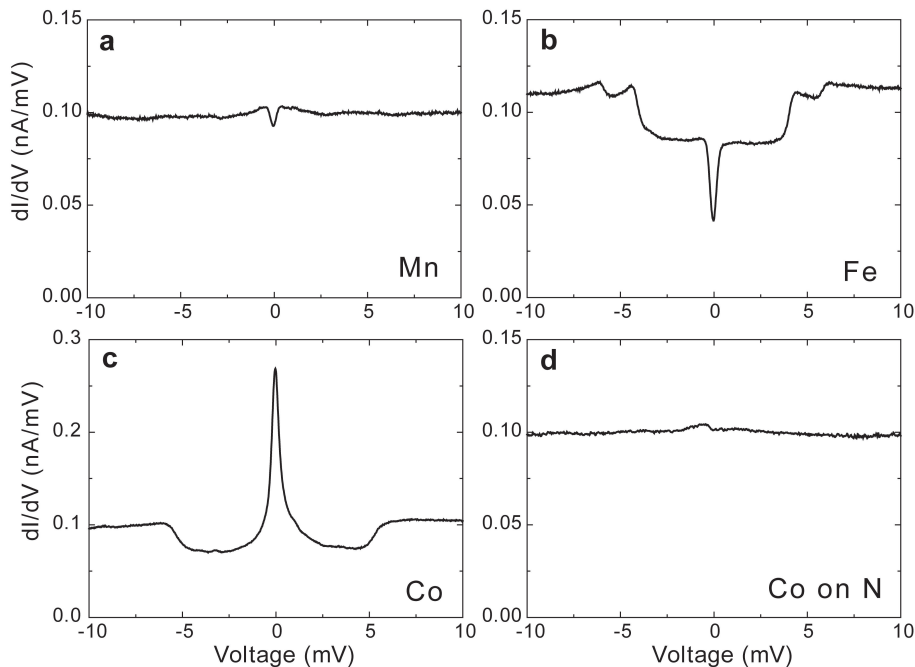


Figure 2.2: Conductance spectra ($50 \mu\text{V}$ modulation, $10 \text{ mV}/1 \text{ nA}$ quiescent, 0.5 K , $B = 0 \text{ T}$) taken on individual Mn (a), Fe (b) and Co (c) atoms located on Cu sites and a Co atom on a N site (d). Note that panel (c) has a different vertical scale.

in the topograph. The empty sites that are bordered by four Cu atoms will be referred to as ‘vacancies’. As a consequence of this arrangement there are rows of N-separated Cu atoms (N-rows) as well as rows of vacancy-separated Cu atoms (v-rows). The thinnest border between two islands (as seen for instance between the center island and its left neighbor in the image) is actually a row of ‘missing’ N atoms. These can be used to exactly locate the N-rows within the island and with that we can in principle pinpoint every lattice site. In section 2.3.3 we will discuss a more practical way to distinguish the N-rows from the v-rows.

Magnetic atoms on Cu_2N can be found either sitting on top of Cu atoms or on top of N atoms. At first sight they all appear to be identical (fig. 2.1a). This is where SES comes in: figures 2.2a–c show spin excitation spectra taken on each of the three species when located on a Cu site. The curves are remarkably different. Evaporating one element at a time enabled us to tell which is which: Mn has a small but distinct dip at zero bias, Fe features three steps on either side and Co can be recognized by a sharp peak around zero and a single step on either side. Spectra taken on other atoms of the same kind are identical except for only slight variations of less than 5% in the positions of the steps. Although the physics behind the exact shapes of these curves will not be discussed until chapters 3 and 4, it is evident that SES provides a way to accurately determine

the chemical identity of these atoms. At least, as long as the atoms are located on the Cu sites: the spectrum in fig. 2.2d was taken on a magnetic atom that sat on a N atom. Here, it shows no features whatsoever (except for a slight bump near the center which was only incidental). This particular atom later turned out to be Co (see section 2.3.3), but the other two elements appear similarly featureless when located on N¹.

Another way to visualize the strength of SES concerning chemical identification is by making a dI/dV -map. When doing this it is tempting to choose the bias voltage V_0 such that there is a high contrast between the atoms in $dI/dV|_{V=V_0}$. But we should not forget that during scanning the feedback loop is closed. The tip height is adjusted to maintain a constant current, or: each dI/dV -curve is scaled to keep its integral until $V = V_0$ constant. Therefore we should be looking for a bias voltage that gives maximum contrast in $(dI/dV)/I|_{V=V_0}$. The map shown in fig. 2.1b, taken at 1 mV, has enough contrast to instantly identify the three different atoms while lying on Cu sites.

The long integration time required to record such a map makes this method not too useful for quick reference. Possibly the fastest way distinguish the atoms is therefore by looking directly at the topography. The profiles of fig. 2.1c (constant current at 1 mV, 0.2 nA) indicate the heights of the three species located on Cu sites: 2.6 Å for Fe, 2.8 Å for Co and 3.0 Å for Mn. But we have to be careful here: as each of them has a different $I(V)$ characteristic because of spin excitations, their relative apparent heights will depend strongly on the bias voltage. It is therefore not surprising that a Co atom on N (atom 5 in fig. 2.1a), being spectroscopically similar, is not distinguishable from Mn on Cu by its ‘height’.

2.3.3 Vertical Atom Manipulation

The technique of controllably repositioning individual atoms with an STM tip can be divided into two categories. Most well-known is the original lateral atom manipulation [2], which is based on the notion that in general it takes less force to move an atom across a surface than it takes to pull the atom off the surface. Here the attractive force of the tip is tuned by adjusting its height and voltage, such that when the tip moves laterally the adatom either slides along smoothly [3, 33] or follows the tip’s path by hopping to stable lattice sites closest to it [34]. This manipulation mode, that stands at the basis of many experiments that involve increasingly complex atomically engineered structures [5, 6, 35], is limited to surfaces that have only little corrugation and therefore not suitable for Cu₂N.

The second category, vertical atom manipulation, uses the ability of an adatom to switch its position from surface to tip and vice versa as first seen for Xe on Ni(110) [36]. This process, occurring during voltage pulses that temporarily increase the current, results from vibrational heating caused by inelastic

¹For Mn on N most of the time the spectrum shows a weak but reproducible signal which we will ignore.

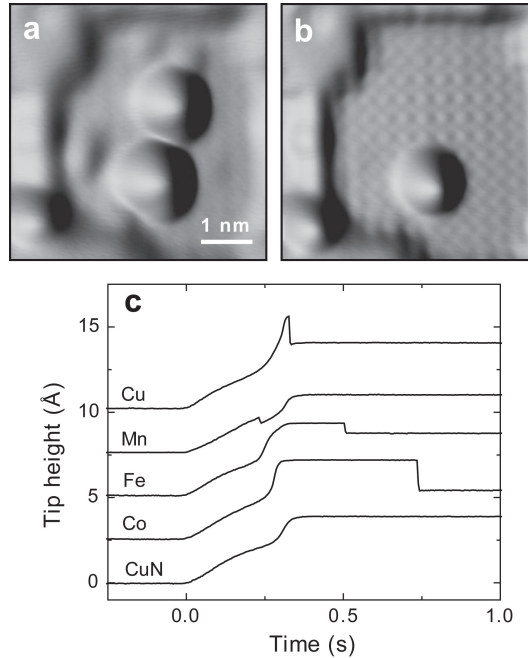


Figure 2.3: Topographs (10 mV/1 nA) taken before (a) and after (b) picking up a Co atom. The lower atom in both images is Mn. (c) Recording of the tip height during hopping. From $t = 0$ the tip voltage is ramped to 1.5 V in about 0.3 s over atoms that are located on N sites. The lower curve shows the same procedure when no adatom is present.

electron tunneling [37]. The direction of atom-transfer is found to be the same as that in which the electrons tunnel, such that by switching the polarity of the voltage pulse one can choose between picking up and dropping off an atom.

Pick Up and Drop Off

On Cu_2N we use the vertical manipulation method as follows. After scanning an image we position the tip over the atom we want to pick up with the feedback loop closed at 10 mV/1 nA. Next the loop is opened and the voltage set to a small value like 1 mV. Now we lower the tip by 2.0 Å and wait for one second, after which we set the tip voltage to +2.0 V for the atom transfer and wait another 200 ms. Finally we reset the tip height to its original value, followed by resetting the voltage. Putting down atoms goes exactly as picking up, the only changes being the stroke length (2.2 Å) and the transfer voltage (−0.5 V).

It should be noted that the success rate of this procedure depends strongly on the microscopic geometry of the tip. However, repeated tip pokes as discussed in section 2.2.2 have reproducibly generated tips that could reliably pick up and drop off one specific atom tens of times in a row. In these cases the ‘loaded’ tip,

having only one apex-atom, could be clearly distinguished from the ‘unloaded’ tip. A good example is shown in figs. 2.3a and b: the topograph produced by the loaded tip is sharp enough to reveal the atomic structure of the Cu_2N , whereas the unloaded tip creates ghost-images of nearby objects as a result of multiple-tip effects.

Although magnetic atoms can be encountered both on Cu and N sites, during a drop-off procedure they always land on a N site. As a result the potential drop-off sites are 3.6 Å apart. This turns out to be sufficient to select the exact landing site before putting down an atom with practically 100% accuracy, provided that the tip is in a good condition for manipulation.

Hopping Atoms

Surprisingly, the N sites are not the lowest energy positions for the adatoms. When being treated with a 1.5 V pulse (from a tip that is at ~ 3 Å distance, corresponding to 10 MΩ contact resistance), the Mn, Fe and Co atoms always hop to one of the four neighboring Cu sites, from where they cannot be removed other than via a pick-up. Whether this change of preferred configuration is caused by a voltage-induced reconstruction of the lattice we do not know. Also, we have not been able to control the direction of hopping. Nonetheless, this property can be very useful in determining an adatom’s exact position: by recording its hopping direction we can tell whether it ended up on a N-row (and v-column) or on a v-row (N-column), lifting the need to ‘count from the edges’ as discussed in section 2.3.2.

Sometimes an adatom hops diagonally instead, towards a vacancy site. This behavior is atom-specifically reproducible (i.e. once an atom has been observed to hop diagonally it will do this repeatedly and exclusively, while other atoms never make diagonal hops) and must therefore be an intrinsic property of the atom. As this happens more often with atoms that fall off the tip after poking (section 2.2.2), we believe that it is specific to Cu adatoms. Additional indications for this hypothesis are that the diagonal-hopping atoms appear smaller in topography than the magnetic adatoms and that they show no spectroscopic feature whatsoever, regardless whether located on a vacancy or a N site.

The hopping behavior provides another way to identify a certain adatom. As shown in fig. 2.3c each atom hops at a slightly different voltage, giving rise to characteristic tip-height traces. Intriguing is the delay involved in Fe and especially Co, which can stay on a N site for several seconds after the tip voltage has reached 1.5 V before hopping.

To summarize, spin excitation spectroscopy has developed into a very precise and powerful tool for studying individual magnetic atoms, and Cu_2N seems to be an ideal surface on which to place those atoms. The stage is set for some beautiful experiments that will be presented in the following three chapters.

Chapter 3

Magnetic Anisotropy

The work presented in this chapter was published as *Large Magnetic Anisotropy of a Single Atomic Spin Embedded in a Surface Molecular Network*, by C. F. Hirjibehedin, C.-Y. Lin, A. F. Otte, M. Ternes, C. P. Lutz, B. A. Jones, and A. J. Heinrich, *Science* **317**, 1199 (2007).

3.1 Introduction

Anisotropy is what makes the difference between spin and magnetism. A free atom, regardless of its electronic structure, is always perfectly spherical. Although it may possess a finite amount of spin (as a result of some electron orbitals being half-filled), the lack of anisotropy makes the orientation of the spinning axis intrinsically undetermined and therefore it will never exhibit magnetism. The tendency to align the angular momentum in a certain direction and the ability to maintain the resulting magnetization over an extended amount of time is governed entirely by the atom's immediate environment.

The same is true for large ensembles of spins. Current non-volatile magnetic storage devices (hard drives) are based on a continuous thin film of ferromagnetic material, the magnetic domains of which are much smaller than the bits we intend to write on it. The anisotropy of the material will make sure that each domain has an 'easy-axis' along which it would like to magnetize either up or down. In order to flip a domain one would have to overcome an energy barrier $\Delta\varepsilon = K_u V$ [38]. Here K_u is the anisotropy constant and V the volume of the domain. At a finite temperature T this will happen spontaneously with a rate

$$\frac{1}{\tau} = f_0 e^{-\Delta\varepsilon/k_B T}, \quad (3.1)$$

where f_0 is a measure of the attempt frequency, typically taken to be 10^9 s^{-1} , and k_B is Boltzmann's constant. A reliable storage medium has $\Delta\varepsilon/k_B T = 50$ or higher. If however from here we reduce the domain volume V by only a factor of 2, the decay time τ will decrease by a factor e^{25} ($\sim 10^{11}$)! Clearly, we are

extremely limited in reducing the domain size and hence the bit size as long as we cannot control the anisotropy. This impending technological barrier, that currently threatens to halt the decades-long trend toward ever higher storage densities at room temperature, is called the *superparamagnetic limit*.

Much larger anisotropies per atom than the ones found in current thin-film magnetic materials have been reported in magnetic structures consisting of only a few atomic spins, such as single atoms and clusters on metal surfaces [39, 40] and molecular magnets [41, 42, 43]. These systems are of technological interest as they have energy barriers that are already high enough to maintain a stable spin orientation at low temperatures.

To lowest order, the energy of a spin in an environment with uniaxial anisotropy (i.e. where only one axis is unique) can be described by [43]:

$$\hat{\mathcal{H}} = -g\mu_B\mathbf{B} \cdot \hat{\mathbf{S}} + D\hat{S}_Z^2. \quad (3.2)$$

Here the first term is the Zeeman splitting of the states in the presence of a magnetic field, where g is the g -factor, μ_B the Bohr magneton and $\hat{\mathbf{S}} = (\hat{S}_X, \hat{S}_Y, \hat{S}_Z)$ the spin operator. The anisotropy is represented by the second term which splits the zero-field degeneracy of the spin-states based on the magnitude of the spin's Z -projection m . If

$D < 0$, large values of $|m|$ are favored and we can speak of an ‘easy-axis’. With $D > 0$, the spin would like to minimize the Z -component of its magnetic moment such that the system has an ‘easy-plane’ orthogonal to the unique axis. For the first case the effect of this term is sketched in fig. 3.1: a barrier of height $-DS^2$ for integer spin and $-D(S^2 - \frac{1}{4})$ for half-integer spin separates the two metastable configurations.

If all three axes are unique we add another term to the Hamiltonian expressing the difference between the remaining two directions (transverse anisotropy):

$$\hat{\mathcal{H}} = -g\mu_B\mathbf{B} \cdot \hat{\mathbf{S}} + D\hat{S}_Z^2 + E(\hat{S}_X^2 - \hat{S}_Y^2). \quad (3.3)$$

By convention, the axes are assigned as to maximize $|D|$ and have $E > 0$. Note that we use the coordinate symbols (X, Y, Z) to distinguish from the real-world axes (x, y, z) , which will be defined in section 3.3. The transverse term does not commute with \hat{S}_Z , such that it mixes states with different m . This means that the two magnetization directions no longer represent stationary states as a result of which the system cannot be used as a bit anymore. We can now conclude that an ideal situation for data storage occurs when S is large, D is large and negative and E is very small.

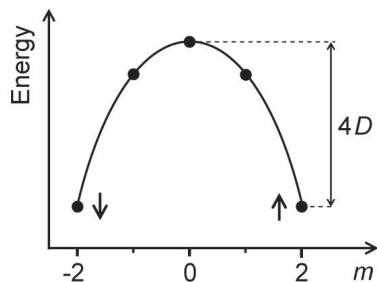


Figure 3.1: Schematic view of the \hat{S}_Z eigenvalues of an $S = 2$ system under axial anisotropy with $D < 0$.

3.2 Cu_2N : a Molecular Network

When an atom is placed upon a surface, obviously the out-of-plane direction becomes unique. In the particular case of atoms bound on the Cu sites of Cu_2N there is a distinction between the two in-plane directions as well: if the atom is positioned on a N-row it is part of a v-column in the other direction or vice versa (a schematic drawing can be found further on in fig. 3.4a). In this section we will look at the exact composition of the Cu_2N surface in more detail.

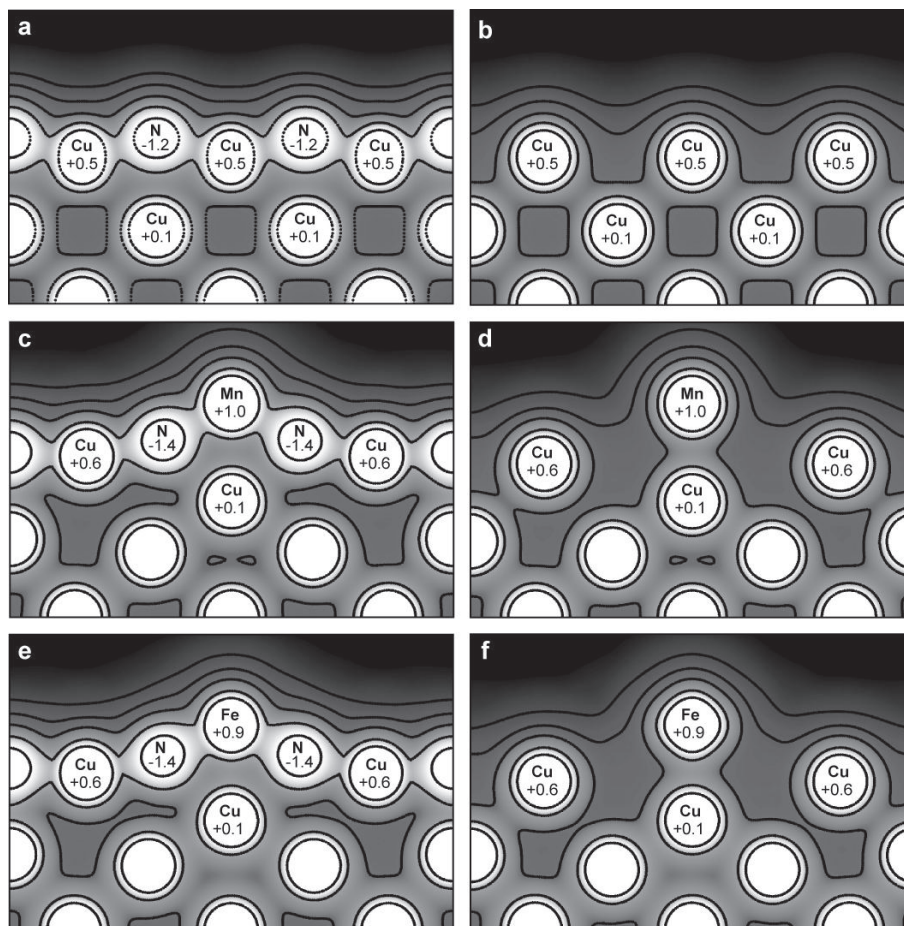


Figure 3.2: DFT calculations of the electron density in the Cu_2N lattice. (a, b) Cross-sectional views of bare Cu_2N through a N-row (a) and through a v-row (b). (c–f) Same for Cu_2N with a Mn or Fe atom adsorbed onto it. Dark (*high*) regions indicate low (*high*) electron density. The black equal density lines are spaced logarithmically at powers of $10^{1/2} e/a_0$, where e is the elementary charge and a_0 the Bohr radius. The line at highest density corresponds to $10^{-1/2} \simeq 0.3 e/a_0$. At each atom the net charge is given in units of e .

To better understand the structure formed by magnetic atoms on Cu_2N , we used density functional theory (DFT) calculations of the electron density performed by C.-Y. Lin and B.A. Jones. These were done using the all-electron full-potential linearized augmented plane wave (FLAPW) method [44] with the exchange-correlation potential in the generalized gradient approximation (GGA) [45]. For details of the calculation see [46]. Figures 3.2a and b show cross-sections of the calculated charge density of Cu_2N on $\text{Cu}(100)$ in the absence of any adatom, respectively along a N-row and a v-row. The N atoms are seen to be slightly above the plane of the surface Cu atoms. In addition, there is a net transfer of (negative) charge from the Cu atoms to the N atoms. A comparison of the charge densities along the two orientations shows that the Cu_2N has formed a network of polar covalent bonds along the N-rows that is distinct from the underlying bulk copper.

Placing an Mn or Fe atom on top of a Cu atom causes a substantial rearrangement of the atomic structure. As seen in figs. 3.2c–f for both Mn and Fe, the Cu atom directly below the magnetic atom has moved toward the bulk and is no longer part of the polar covalent Cu_2N network. The magnetic atom transfers charge to the Cu_2N surface and creates bonds with its neighboring N atoms: the magnetic atom is thus incorporated into the extended molecular network on the surface. In view of these significant structural and electronic changes involved in placing an atom on the surface, it is all the more surprising that we can reverse the process by removing an adatom as described in the previous chapter without permanently changing the Cu_2N surface.

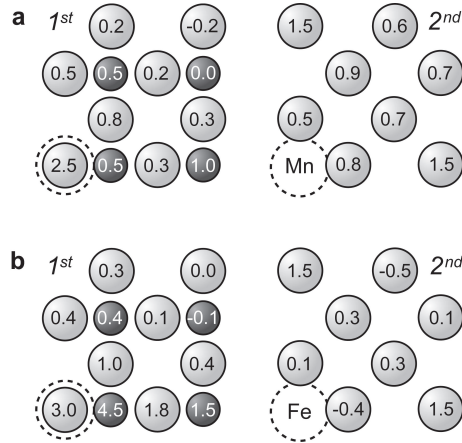


Figure 3.3: Calculations of the local spin density on each atom for (a) Mn and (b) Fe on Cu_2N . In either case the left (*right*) image shows the first (*second*) layer of atoms. Cu atoms are depicted as large light grey spheres while N atoms are smaller and dark. Dashed circles indicate the position of the adatom above the first layer. The numbers give the net spin ($\times 100$) on each atom and its surrounding interstitial region. Including the spin on the adatoms, these add up to 250 for Mn and 200 for Fe.

The calculations can also give information on the local distribution of spin, determined by evaluating $S = (N_{\uparrow} - N_{\downarrow})/2$ where N_{\uparrow} and N_{\downarrow} are the total number of electrons with spin up and down in a specified volume. In the case of Mn, the spin on the atom itself and the surrounding interstitial region is $S = 2.28$, whereas for Fe $S = 1.73$. These values are slightly lower than the free-atom spins (i.e. $S = \frac{5}{2}$ for Mn and $S = 2$ for Fe), however, a substantial amount of spin density extends into the surrounding atoms, as illustrated in fig. 3.3. By including the spin on all of the atoms, the net spin of the total structure is calculated to be the same as that of the free atoms (2.50 and 2.00). Specifically in the case of Fe we find that the spin spreading occurs primarily along the direction of the N-row, while for Mn there seems to be a slightly stronger tendency to spread down into the second layer. This spreading of spin density, here up to 5 Å from the binding site, is similar to that reported in DFT calculations of molecular magnets [48]. In comparison, no substantial net spin density is found for bare Cu₂N on Cu(100).

3.3 Anisotropy in Spin Excitations

The existence of zero-field excitations as seen in the spectra of fig. 2.2, indicating that the different spin orientations (quantum number m) are non-degenerate, suggests that the atomic spins on Cu₂N are subject to strong magneto-crystalline anisotropy. We studied the anisotropy of Mn and Fe atoms on the Cu sites of Cu₂N by following the evolution of their spin excitations when a magnetic field is applied in three orthogonal directions. As discussed in section 1.4 the He dewar in which the 7 T superconducting magnet was mounted could be rotated such that the field was either in the plane of the sample or perpendicular to it. In the second case there was a $\sim 7^\circ$ tilt of the magnetic field with respect to the sample's normal vector which we will ignore during further analysis. When the magnetic field was in the plane, the orientation of the sample was such that the field aligned with the (001)-direction of the crystal, i.e. parallel to the N-rows and v-rows in one direction (in this situation there was a $\sim 5^\circ$ misalignment that we will ignore). Distinction between the two in-plane field directions was made by separately regarding adatoms that were located either on a N-row or on a v-row. As a result, multiple field directions could not be realized on a single atom (without repositioning it). Switching from an in-plane to a perpendicular field even required preparing a whole new sample (section 2.2.1) as it involved dismantling the entire cryostat. For each individual atom lying on a Cu site, we will use the coordinate system as defined for Mn in fig. 3.4a, where x is directed along the N-row, y along the v-row and z is the surface's normal vector.

In the subsequent analysis we will describe each of the atomic spin systems by a single spin vector \mathbf{S} . It is important to note that this 'spin' is a resultant quantity which comprises both the intrinsic spin of the electrons and their orbital angular momentum. As the crystal field can only directly influence the latter, spin-orbit coupling plays an important role in translating the effects of magnetic anisotropy to the actual electronic spins.

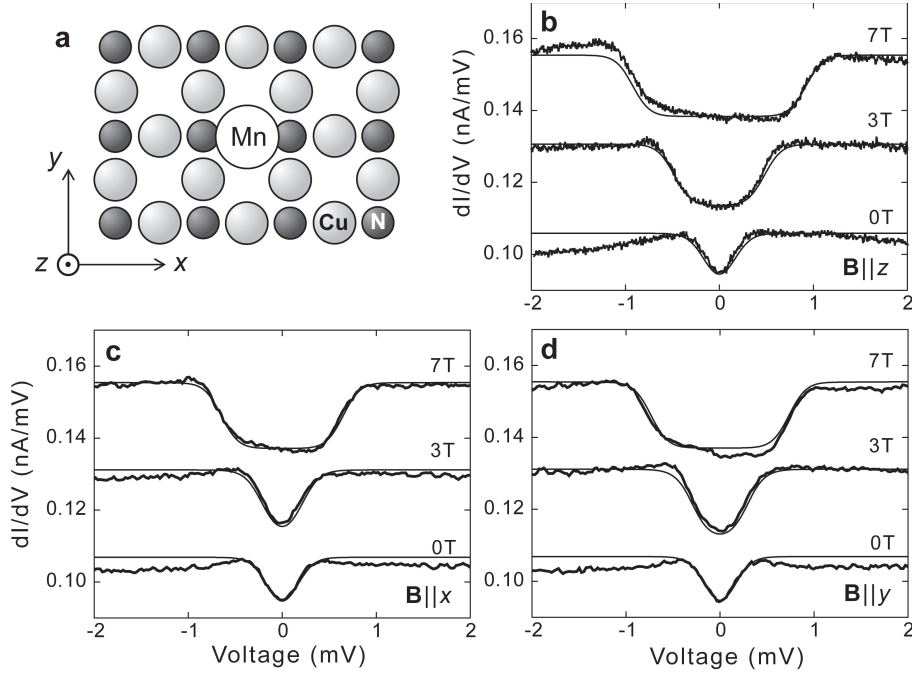


Figure 3.4: (a) Schematic top view of Mn on Cu₂N. This assignment of the axes will be used for any single atom on Cu₂N. (b–d) dI/dV -spectra on a individual Mn atoms in various magnetic fields oriented along z , x and y in (b), (c) and (d) respectively. Smooth curves show the calculated conductance based on (3.5), scaled to fit the data.

3.3.1 Mn: a Weak Easy-Axis

Figures 3.4b–d show spin excitation spectra taken on three different Mn atoms, each corresponding to one field direction, at 0 T, 3 T and 7 T. In each situation the energy of the single step that is found symmetrically around zero bias grows with the field strength. The rate at which it grows is nearly equal for $\mathbf{B} \parallel x$ and $\mathbf{B} \parallel y$ (the two in-plane directions), but is markedly higher when $\mathbf{B} \parallel z$. We shall try to explain these observations using the anisotropy Hamiltonian (3.3). Mn is a $3d^5$ metal so we expect its spin to be $\frac{5}{2}$. Since the x and y field orientations give similar results we can expect the main anisotropy axis \mathcal{Z} to coincide with the z -direction, and E to be very small. Fig. 3.5a shows the qualitative effect the anisotropy Hamiltonian has on the energy levels of an $S = \frac{5}{2}$ system when $D < 0$, $E = 0$ and $\mathbf{B} \parallel \mathcal{Z}$. If we assume the transitions to obey the selection rules¹ $\Delta m = 0$ or ± 1 , a single transition from the ground state ($m = \frac{5}{2}$) to $m = \frac{3}{2}$ is allowed, the energy of which is finite at $B = 0$ and grows linearly with the field. Note that if we choose $D > 0$, $m = \frac{1}{2}$ would become the ground state and we would have two allowed transitions (to $m = \frac{3}{2}$ and $m = -\frac{1}{2}$).

¹We will discuss these rules in section 3.3.3.

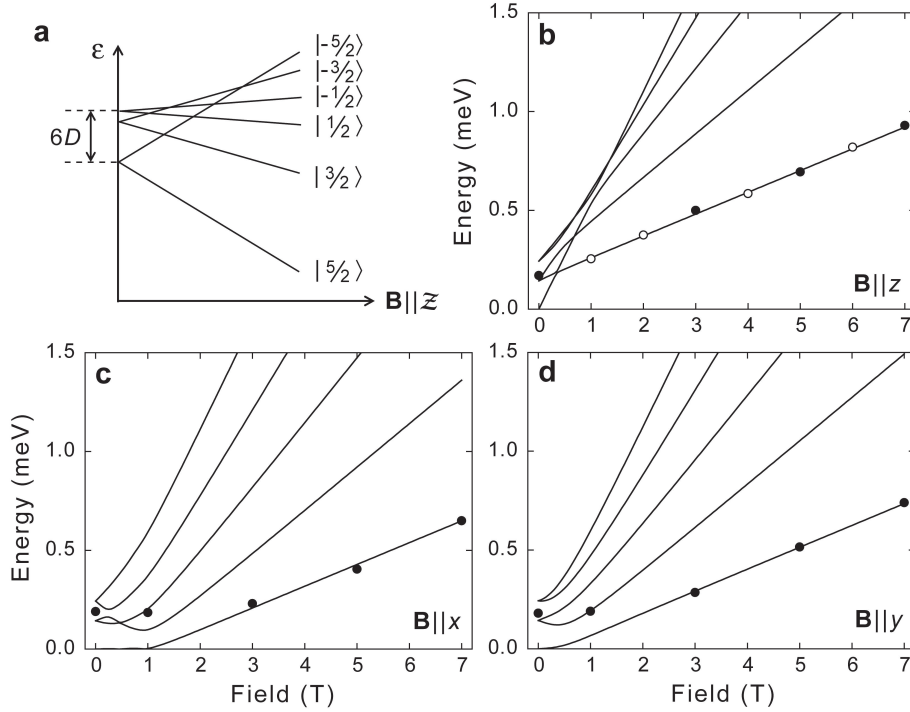


Figure 3.5: (a) Sketch of the qualitative effect of a negative D -value on an $S = \frac{5}{2}$ system when the field is oriented along the primary axis \mathcal{Z} . (b–d) Step energies taken from fig. 3.4. The solid lines indicate excitation energies obtained by diagonalization of 3.3. In (b) the open circles label step energies measured on a different Mn atom.

We obtained the best fit of the step positions when $g = 1.90 \pm 0.01$, $D = -0.039 \pm 0.001$ meV, and $E = 0.007 \pm 0.001$ meV with $(\mathcal{X}, \mathcal{Y}, \mathcal{Z}) = (x, y, z)$. The calculated transition energies for these values are shown in figures 3.5b–d. Due to the weakness of the anisotropy there are many level crossings at low magnetic field. Especially in the x and y -directions, where even at $E = 0$ the levels are not eigenstates of \hat{S}_z , this complicates the exact assignment of the spin excitations.

The resulting parameters correspond to a magnetic easy-axis pointing out of the plane (i.e. $\mathcal{Z} = z$). The value of D , which is much smaller than the anisotropy of Fe as will be discussed shortly, is consistent with anisotropy values observed for Mn in molecular magnetic clusters [49]. Small anisotropy is also expected for half filling of the d -orbitals. Hund’s rule coupling leads to alignment of the electron spin and single occupation of all d -states, giving rise to a symmetric charge distribution within the d -shell. Although the results indicate a finite value for E , its magnitude is still too small to cause observable transitions to other levels that could arise from mixing of the eigenstates.

3.3.2 Fe: Almost a Bit

The zero-field spectrum of Fe, which based on its electronic configuration ($3d^6$) we expect to behave as an $S = 2$ system², features three steps at $|V| \simeq 0.2, 3.8$ and 5.7 mV. These excitation energies change by less than $\sim 5\%$ between various measurements performed on Fe atoms adsorbed on different Cu_2N islands and measured with different tips. This variation may arise from slight changes in the local environment caused by the inherent strain in the Cu_2N islands [50]. The appearance of three spin excitations can be explained by choosing the anisotropy parameters $D < 0$ and $E \neq 0$, as illustrated qualitatively in fig. 3.7a. The result of having a substantial E (and the absence of Kramers degeneracy for integer S , see chapter 4) is that all zero-field degeneracy is broken, including that for equal $|m|$. Now the 0.2 meV step can be assigned to an excitation between $|m| = 2$ states, while the steps at higher energies are signatures of $|m| = 2 \rightarrow 1$ transitions. Excitations to $m = 0$ are forbidden by the selection rules.

The field dependence of the step positions (figs. 3.6a–c) is much more anisotropic than in the case of Mn. A clear example is the 5.7 meV step, that goes up in energy with increasing $\mathbf{B} \parallel x$ and down when $\mathbf{B} \parallel y$. The evolution of the heights of the steps, which is similarly anisotropic, especially for the 0.2 meV excitation, will be discussed in the next section. Calculations of the energy levels, fitting the measured step positions, are plotted in figs. 3.6d–f. The parameters used here are $g = 2.11 \pm 0.05$, $D = -1.55 \pm 0.01$ meV and $E = 0.31 \pm 0.01$ meV, with the anisotropy axes assigned as $(\mathcal{X}, \mathcal{Y}, \mathcal{Z}) = (y, z, x)$. This translates into a strong easy-axis (\mathcal{Z}) along the N-direction (x), with a significant contribution from transverse anisotropy. Similar values, although usually with positive D (corresponding to planar or hard-axis anisotropy), have been observed in crystals formed from molecular magnet structures with single Fe atoms [49].

3.3.3 Transition Intensities

In order to better understand the inelastic tunneling process that governs the spin excitations we can additionally analyze the intensity of the observed transitions. We find that the relative step heights in the Fe spectra, which should be a measure of the excitation intensities, are well-described by:

$$\begin{aligned} I_{0 \rightarrow n} &= \left| \langle \psi_n | \hat{S}_{\mathcal{X}} | \psi_0 \rangle \right|^2 + \left| \langle \psi_n | \hat{S}_{\mathcal{Y}} | \psi_0 \rangle \right|^2 + \left| \langle \psi_n | \hat{S}_{\mathcal{Z}} | \psi_0 \rangle \right|^2 \\ &= \frac{1}{2} \left\{ \left| \langle \psi_n | \hat{S}_+ | \psi_0 \rangle \right|^2 + \left| \langle \psi_n | \hat{S}_- | \psi_0 \rangle \right|^2 + 2 \left| \langle \psi_n | \hat{S}_{\mathcal{Z}} | \psi_0 \rangle \right|^2 \right\}, \end{aligned} \quad (3.4)$$

where $\hat{S}_{\pm} = \hat{S}_{\mathcal{X}} \pm i\hat{S}_{\mathcal{Y}}$ and the $|\psi_n\rangle$ states are obtained directly from diagonalization of (3.3), with $|\psi_0\rangle$ being the ground state. This expression was also used for analysis of neutron scattering experiments on a similar magnetic system [51]. The first two terms enable $\Delta m = \pm 1$ transitions and the third term

²See section 3.4 for a discussion on the validity of using the free-atom value of S .

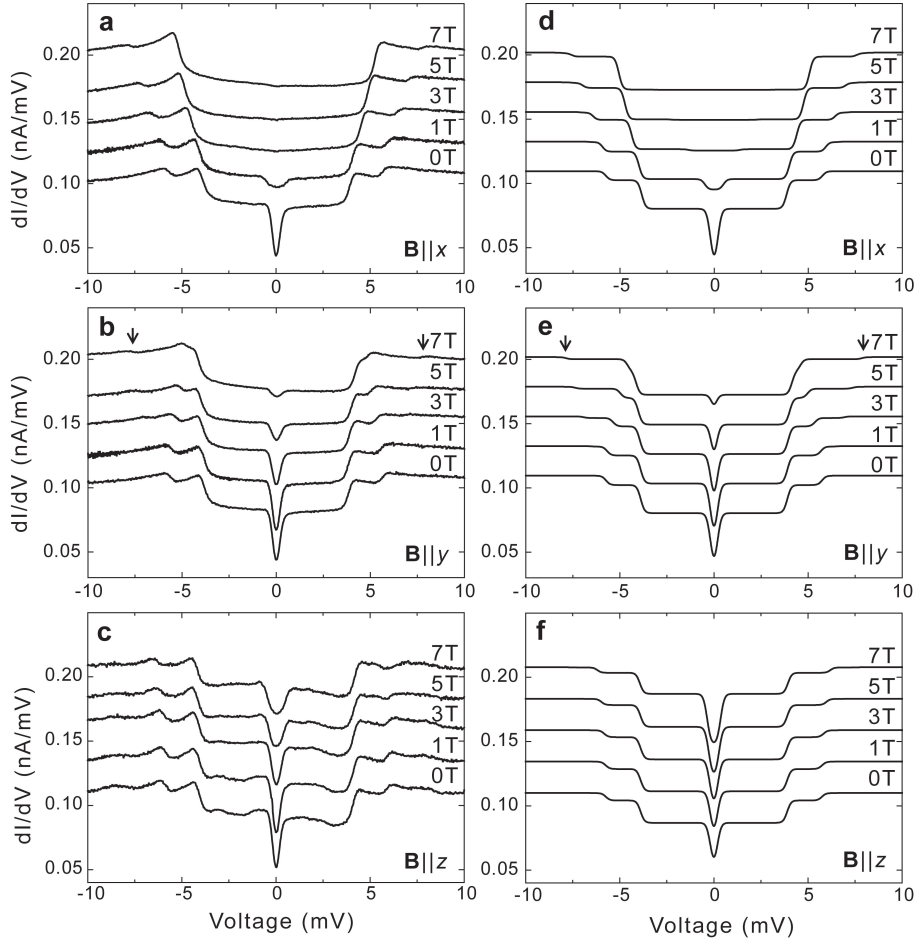


Figure 3.6: Conductance spectra on Fe in various magnetic fields oriented along x (a), y (b) and z (c). (d–f) Calculated conductance curves based on (3.5). The arrows indicate the appearance of the $|\psi_0\rangle \rightarrow |\psi_4\rangle$ transition.

allows $\Delta m = 0$. These selection rules are consistent with previous empirically observed transitions in STM spin-excitation experiments [19].

Table 3.1 lists the $|\psi_n\rangle$ vectors (still for Fe) in the basis of \hat{S}_Z -eigenstates $|m\rangle$. When $B = 0$ T, the ground state $|\psi_0\rangle$ has most weight in the $|-2\rangle$ and $|+2\rangle$ states. From here, transitions to $|\psi_1\rangle$ ($\Delta m = 0$) and $|\psi_2\rangle$ and $|\psi_3\rangle$ ($\Delta m = \pm 1$) are strong, whereas transitions to $|\psi_4\rangle$ are forbidden. At $B = 7$ T along Z (i.e. x , the N-row), the situation changes substantially: because most of the weight in $|\psi_0\rangle$ is now in the $|+2\rangle$ state, $\Delta m = \pm 1$ transitions to $|\psi_2\rangle$ and $|\psi_3\rangle$ remain visible while transitions to $|\psi_1\rangle$ (now mostly $|-2\rangle$) and $|\psi_4\rangle$ are too weak to be observed. This is consistent with the observed disappearance of the 0.2 meV step for $B > 1$ T in the x -direction.

Table 3.1: Eigenvectors for Fe on Cu₂N, written as a sum of $|m\rangle$ states and obtained by diagonalization of (3.3) with $S = 2$, $g = 2.11$, $D = -1.55$ meV and $E = 0.31$ meV, at $B = 0$ T and $B = 7$ T oriented along \mathcal{Z} .

Eigenstate	$ -2\rangle$	$ -1\rangle$	$ +0\rangle$	$ +1\rangle$	$ +2\rangle$
$B = 0$ T					
$ \psi_0\rangle$	0.697	0	-0.166	0	0.697
$ \psi_1\rangle$	0.707	0	0	0	-0.707
$ \psi_2\rangle$	0	0.707	0	-0.707	0
$ \psi_3\rangle$	0	0.707	0	0.707	0
$ \psi_4\rangle$	0.117	0	0.986	0	0.117
$B = 7$ T					
$ \psi_0\rangle$	0.021	0	-0.097	0	0.995
$ \psi_1\rangle$	0.987	0	-0.157	0	-0.036
$ \psi_2\rangle$	0	0.402	0	-0.916	0
$ \psi_3\rangle$	0	0.916	0	0.402	0
$ \psi_4\rangle$	0.159	0	0.983	0	0.092

Calculated values for $I_{0 \rightarrow n}$ with $\mathbf{B} \parallel \mathcal{Z}$ are shown in fig. 3.7b. They are normalized to fit the relative step heights as extracted from the measurements. Note that it would be senseless to compare the absolute step heights. As certain transitions die out the total inelastic current decreases, but each spectrum is started at the same quiescent settings such that other inelastic contributions (i.e. excitation intensities) are rescaled. Therefore we look at the relative composition of the inelastic current, which gives meaningful quantities at any field. A similar calculation with $\mathbf{B} \parallel \mathcal{X}$ (i.e. y , the v-row) indicates that starting from ~ 2 T in this direction the $|\psi_0\rangle \rightarrow |\psi_4\rangle$ transition should open up. This may explain the small steps around $|V| = 8$ meV indicated by the arrows in the 7 T spectrum of fig. 3.6b.

We can even model the full conductance spectra as the sum of a voltage-independent elastic conductance and a series of thermally broadened IETS transitions. For the inelastic part of the conductance we use:

$$\sigma_{ie} \propto \sum_m \sum_{n>m} I_{m \rightarrow n} P_m(T) (1 - P_n(T)) \times \left\{ \Phi \left(\frac{eV + (\varepsilon_n - \varepsilon_m)}{k_B T} \right) + \Phi \left(-\frac{eV - (\varepsilon_n - \varepsilon_m)}{k_B T} \right) \right\}, \quad (3.5)$$

where each IETS step is weighted by the calculated intensity $I_{m \rightarrow n}$ as given by (3.4) and by the Maxwell-Boltzmann distribution:

$$P_i(T) = \frac{e^{-\varepsilon_i/k_B T}}{\sum_j e^{-\varepsilon_j/k_B T}}. \quad (3.6)$$

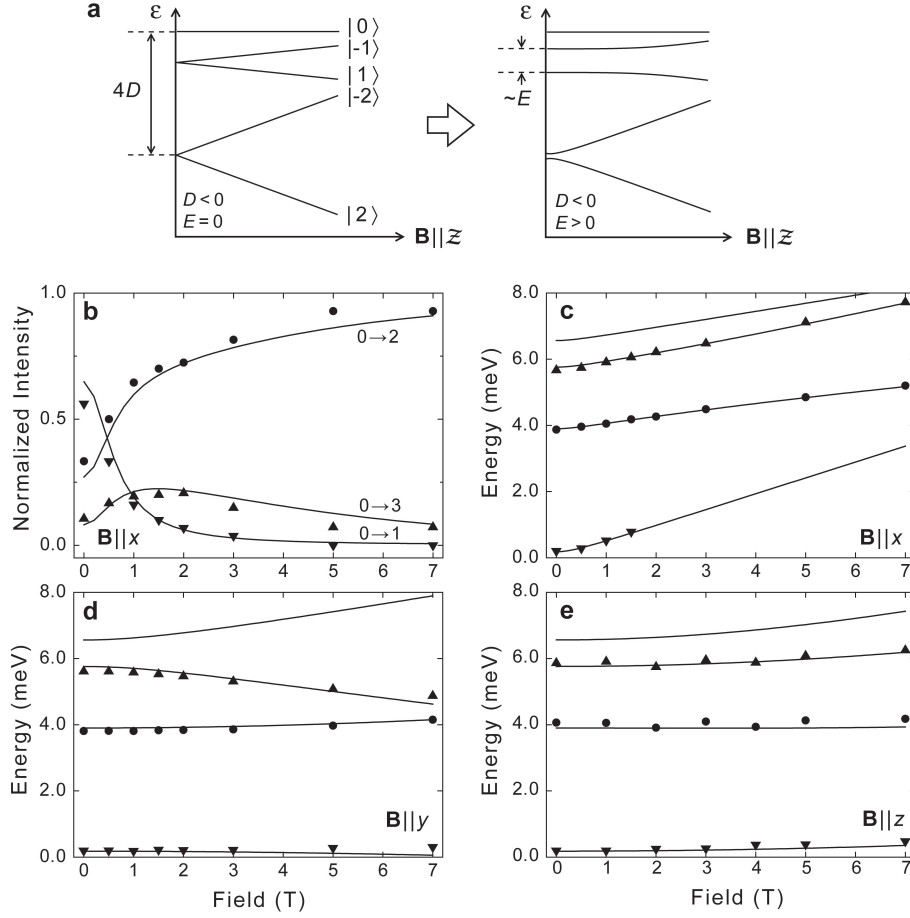


Figure 3.7: (a) Sketch of the qualitative effect of a finite E -value on an $S = 2$ system with negative D . (b) Step heights taken from fig. 3.6a. The solid lines show the calculated transition intensities based on (3.4). (c–e) Step positions acquired from fig. 3.6a–c, plotted together with the calculated excitation energies for Fe.

Thus $P_m(T)(1 - P_n(T))$ quantifies the probability of simultaneously having a filled initial state $|\psi_m\rangle$ and an empty final state $|\psi_n\rangle$. The shape of the IETS transitions is given by:

$$\Phi(x) = \frac{1 + (x - 1)e^x}{(e^x - 1)^2}. \quad (3.7)$$

This was derived for molecular vibration spectra [52, 53] and incorporates the thermal broadening caused by the finite temperature of the electrodes. To make sure that the summation runs only over positive energy excitations, the eigenstate indices n are assumed to be ordered with increasing energy ε_n . The

resulting modelled spectra for Fe (figs. 3.6d–f) correspond extremely well to the experimental data. Similar modelcurves for Mn are plotted together with the data in fig. 3.4.

The level of agreement between those modelled spectra and the experimental data is astonishing, considering that (apart from an overall scaling factor) no additional fitting is performed. For each type of atom the parameters S , g , D and E are determined once from the field dependence of the step energies and that information is sufficient to reconstruct a spectrum taken at any field strength or orientation.

3.4 Discussion

In this chapter we have presented a method to map the magnetic anisotropy of individual atoms using spin excitation spectroscopy. We find that Mn on Cu₂N has a weak easy-axis that is oriented out of plane with very little transverse contribution. Fe is shown to have an easy-axis along the N-row that has much higher anisotropy energy. Although the origin of these specific preferential directions remains to be explained, it is interesting to note that in either case it coincides with the directionality of the spin spreading calculated by DFT. The weakness of the anisotropy for Mn most likely results from the fact that a Mn atom has zero orbital angular momentum. Therefore the crystal field has no channel through which to influence the electronic spins.

For Fe we find $D = -1.55$ meV, corresponding to an energy barrier with height 6.2 meV. According to (3.1) this would result in a bit that is stable below ~ 2 K, if it were not for the significant transverse anisotropy $E = 0.31$ meV. Let us discuss the precise influence of this E -term on the magnetic stability. As shown in table 3.1, at zero field the two lowest-energy eigenstates are (almost) $\frac{1}{\sqrt{2}}(|-2\rangle \pm |+2\rangle)$. Regardless of whether the bit is set to ‘0’ or to ‘1’, one will measure $m = -2$ for 50% of the time and $m = +2$ for the other 50% of the time, making the system unsuitable for data storage. If, however, we were to apply a magnetic field of 2 T permanently over the bit in the \mathcal{Z} -direction, the two lowest states become:

$$\begin{aligned} |\psi_0\rangle &= 0.99|+2\rangle - 0.12|+0\rangle + 0.09|-2\rangle, \text{ and} \\ |\psi_1\rangle &= 0.10|+2\rangle + 0.12|+0\rangle - 0.99|-2\rangle. \end{aligned}$$

These are stationary states that are still separated by a 6.0 meV barrier (i.e. stable at $T \lesssim 2$ K), but now one would measure $m = +2$ for 98% of the time if the bit is set to ‘0’, and $m = -2$ for 98% of the time if set to ‘1’. This way Fe on Cu₂N can be considered a candidate for future laboratory demonstrations of an atomic bistable (albeit metastable in one of the two states) magnetic bit at low temperature.

Throughout the analysis we have used the free-atom spin values, $\frac{5}{2}$ for Mn and 2 for Fe, even though these are not at all necessarily correct for bound atoms. The DFT calculations presented in section 3.2 indicate that part of the

spin density spreads along the surface and into the bulk, suggesting a decrease in the effective spin on the atom. However, as a result of the discrete nature of the system, we can only adjust the quantum number S in steps of $\frac{1}{2}$ while the spin spreading is rather small.

Previously, for the case of Mn on Cu_2N , $S = \frac{5}{2}$ was found to explain the observed excitations better than any of the adjacent values [19]. For Fe, we use the following reasoning. Since we can clearly discern three excitations in the zero-field spectrum there should be at least four energy levels, ruling out any $S < \frac{3}{2}$. As will be derived in the next chapter, for any half-integer spin the zero-field degeneracy between states with equal $|m|$ cannot be broken by an E -term (Kramers degeneracy). This way we can additionally rule out any half-integer $S < \frac{7}{2}$. The remaining spin values are integer $S \geq 2$ or half-integer $S \geq \frac{7}{2}$, but as $S = \frac{5}{2}$ is the highest spin a d -shell magnet can adopt $S = 2$ is the only possibility left³.

A point that remains unclear is the role of the orbital angular momentum of the electrons in the d -shell. Both the values for S and for g that we find (in each case close to $g = 2.00$ as expected for a pure electron spin) suggest that the orbital moment makes no substantial contribution to the effective spin vector \hat{S} . One possibility is that the crystal field either quenches the orbital angular momentum or suppresses the spin-orbit coupling. However, this would in turn make the electron spins invulnerable to the influence of the crystal field which is clearly not the case.

The matrix elements (3.4) that were found to accurately determine the transition intensities are identical to those used for explaining inelastic neutron scattering in a magnetic molecular cluster (Fe_8) [51]. This could indicate that the observed inelastic tunneling arises from similar dipolar magnetic interactions between the spin of the tunneling electron and that of the magnetic atom. Especially for Fe the intensity of this process is remarkably large: at $B = 0$, the combined inelastic conductance (i.e. the sum of the IETS step heights) is larger than the elastic conductance (as measured at $V = 0$). Even the step of one of the individual transitions ($|\psi_0\rangle \rightarrow |\psi_1\rangle$) is at least as high as the background. This is surprising: not only does the excitation open a new inelastic conduction channel, its transmission is possibly even enhanced compared to the elastic path. A more detailed study of the inelastic excitations in comparison to the elastic current may provide insight into which electronic orbitals are involved in either process. In chapter 5 we will discuss a possible first step in that direction.

³In principle the interaction with the surface might destroy the d -shell character enough as to enable $S \geq 3$ (although the DFT calculations indicate a decrease of spin). This, however, does not fit our data as well as $S = 2$ does.

Chapter 4

The Kondo Effect of a Single High-Spin Atom

The work presented in this chapter and the following chapter was performed in collaboration with C. F. Hirjibehedin, M. Ternes, C. P. Lutz, and A. J. Heinrich.

4.1 Historical Overview

The story of the Kondo effect starts in the 1930's, when De Haas and coworkers in Leiden measured the resistance of some metals at very low temperatures. They found that surprisingly, the resistance of their gold samples increased rather than decreased when being cooled down below approximately 8 K [54]. Although they already suspected the appearance of this resistance-minimum to be related to the purity of the sample material, the presently accepted explanation was not proposed until 1968 when Kondo attributed the phenomenon to the presence of magnetic impurities [55]. In the following we will discuss the Kondo effect within the framework of the Anderson Impurity Model [56].

4.1.1 Anderson $S = \frac{1}{2}$ Impurity Model

We consider an atomic impurity that is coupled to a bath of electrons with Fermi energy ε_F . The impurity has an orbital that can host two electrons with opposite spin orientations σ (\uparrow or \downarrow). Each electron on the impurity has an energy ε_d and if the orbital is doubly filled there is an additional Coulomb repulsion energy U . This can be summarized in the Anderson Hamiltonian:

$$\hat{\mathcal{H}} = \sum_{\sigma} \left\{ \varepsilon_d \hat{d}_{\sigma}^{\dagger} \hat{d}_{\sigma} + \sum_{\mathbf{k}} \varepsilon(\mathbf{k}) \hat{c}_{\mathbf{k}\sigma}^{\dagger} \hat{c}_{\mathbf{k}\sigma} + \sum_{\mathbf{k}} \left(V \hat{d}_{\sigma}^{\dagger} \hat{c}_{\mathbf{k}\sigma} + V^* \hat{c}_{\mathbf{k}\sigma}^{\dagger} \hat{d}_{\sigma} \right) \right\} + U \hat{d}_{\uparrow}^{\dagger} \hat{d}_{\uparrow} \hat{d}_{\downarrow}^{\dagger} \hat{d}_{\downarrow}, \quad (4.1)$$

where $\hat{c}_{\mathbf{k}\sigma}^{\dagger}$ and $\hat{c}_{\mathbf{k}\sigma}$ are the creation and annihilation operators of the electrons in the bath (with wave vector \mathbf{k}) while $\hat{d}_{\sigma}^{\dagger}$ and \hat{d}_{σ} create and annihilate electrons

on the impurity. The coupling strength between the impurity and the bath is quantified by V . We choose ε_F and ε_d such that the impurity orbital is half filled in its ground state $|d_\sigma^1\rangle$, which thereby becomes degenerate in σ :

$$|d_\sigma^1\rangle = \hat{d}_\sigma^\dagger \prod_{\mathbf{k}}^{\mathbf{k}_F} \hat{c}_{\mathbf{k}\uparrow}^\dagger \hat{c}_{\mathbf{k}\downarrow}^\dagger |\text{vac}\rangle. \quad (4.2)$$

Here \mathbf{k}_F is the Fermi wave vector and $|\text{vac}\rangle$ the vacuum state. For simplicity we also assume that excitations to $|d^2\rangle = \hat{d}_\sigma^\dagger \hat{c}_{\mathbf{k}\bar{\sigma}}^\dagger |d_\sigma^1\rangle$ and to $|d^0\rangle = \hat{c}_{\mathbf{k}\sigma}^\dagger \hat{d}_\sigma |d_\sigma^1\rangle$ (where $\bar{\sigma}$ denotes the opposite spin orientation of σ), i.e. respectively adding an electron to or removing an electron from the impurity, cost the same amount of energy $U/2$. As a result the situation becomes electron-hole symmetric: there are two Hubbard bands at the same energy which are each other's mirror image through electron-hole inversion. Effectively the impurity is now a localized $S = \frac{1}{2}$ system that can switch its magnetization through either of two virtual processes, each with a transition rate $2V^2/U$:

$$\begin{aligned} |d_{\bar{\sigma}}^1\rangle &= \hat{c}_{\mathbf{k}'\sigma}^\dagger \hat{d}_\sigma \hat{d}_{\bar{\sigma}}^\dagger \hat{c}_{\mathbf{k}\bar{\sigma}} |d_\sigma^1\rangle \quad (\text{i.e. via } |d^2\rangle), \text{ or} \\ |d_{\bar{\sigma}}^1\rangle &= \hat{d}_{\bar{\sigma}}^\dagger \hat{c}_{\mathbf{k}'\bar{\sigma}} \hat{c}_{\mathbf{k}\sigma}^\dagger \hat{d}_\sigma |d_\sigma^1\rangle \quad (\text{i.e. via } |d^0\rangle). \end{aligned} \quad (4.3)$$

Note that such a process – which has to be energy conserving – can only occur around the Fermi energy as it extracts an electron from the bath and replaces it with an electron that has opposite spin. Therefore it requires both filled and empty states at one energy. By performing a canonical transformation [57], it is possible to approximate (4.1) as:

$$\hat{H} \simeq \sum_{\sigma} \sum_{\mathbf{k}} \varepsilon(\mathbf{k}) \hat{c}_{\mathbf{k}\sigma}^\dagger \hat{c}_{\mathbf{k}\sigma} + \frac{2V^2}{U} \sum_{\mathbf{k}\mathbf{k}'} \hat{\mathbf{S}}_d \cdot \hat{\mathbf{S}}_{\mathbf{k}\mathbf{k}'}, \quad (4.4)$$

which is known as the Kondo Hamiltonian. Here $\hat{\mathbf{S}}_d$ is the spin of the impurity and $\hat{\mathbf{S}}_{\mathbf{k}\mathbf{k}'}$ is a second SU(2) (i.e. spin $\frac{1}{2}$) system defined as:

$$\begin{aligned} \hat{S}_{\mathbf{k}\mathbf{k}'}^+ &= \hat{c}_{\mathbf{k}\uparrow}^\dagger \hat{c}_{\mathbf{k}'\downarrow}, \\ \hat{S}_{\mathbf{k}\mathbf{k}'}^- &= \hat{c}_{\mathbf{k}\downarrow}^\dagger \hat{c}_{\mathbf{k}'\uparrow}, \\ \hat{S}_{\mathbf{k}\mathbf{k}'}^z &= \frac{1}{2} \left(\hat{c}_{\mathbf{k}\uparrow}^\dagger \hat{c}_{\mathbf{k}'\uparrow} - \hat{c}_{\mathbf{k}\downarrow}^\dagger \hat{c}_{\mathbf{k}'\downarrow} \right). \end{aligned} \quad (4.5)$$

This effective spin can be seen as the net collective magnetization of the electrons in the bath surrounding the impurity, the two spin orientations of which we shall denote as \uparrow and \downarrow . Since $2V^2/U > 0$, $\hat{\mathbf{S}}_{\mathbf{k}\mathbf{k}'}$ is coupled antiferromagnetically to the impurity spin $\hat{\mathbf{S}}_d$, which is oriented \downarrow and \uparrow respectively. At higher temperatures the system can occupy either of the two degenerate states $|\downarrow, \uparrow\rangle$ and $|\uparrow, \downarrow\rangle$. However, if the temperature T sinks below a characteristic Kondo temperature T_K – where $k_B T_K$ is a measure for the coupling strength between bath and impurity – energy can be gained by forming a spin-singlet

Kondo state $\frac{1}{\sqrt{2}}(|\downarrow, \uparrow\rangle - |\uparrow, \downarrow\rangle)$ [58]. This leads to a sharp resonance in the electron density of states (DOS) of the Kondo system, exactly at the Fermi energy. Although in quantum mechanics the singlet-triplet formation is a common phenomenon when two doublets are coupled, it should be noted that the current system involves many spins that are distributed over a wide area that has unclear boundaries. The Kondo state is therefore a macroscopic many-body quantum state, the exact properties of which are still under debate in many theoretical studies.

As the conduction electrons in the vicinity of the impurity freeze into this singlet state the transport properties of the conductor change significantly, giving rise to the anomalous increase of the resistance that so much puzzled the Dutch scientists in 1936. But it is important to stress that the Kondo effect itself is not a transport property. In the model discussed above we used only one conducting lead that was coupled to a magnetic impurity. Translated to an STM geometry this means that if a magnetic atom is coupled to the metal surface, the tip is not needed to form a Kondo system. So unlike the inelastic electron excitations of the previous chapters, the Kondo effect just happens; even if you don't measure it.

4.1.2 Experimental Realizations of a Single Kondo Spin

In 1998 research on the Kondo effect experienced a revival when it became possible to experimentally isolate and study a single Kondo-screened spin. This milestone was achieved almost simultaneously through the use of two independently evolved techniques. First, artificially crafted quantum dots in GaAs/AlGaAs semiconductor heterostructures were depleted until they effectively held one electron [59, 60]. The half-integer spin that was thus isolated interacted with neighboring leads via a coupling that could be tuned with great precision. This method provides an extreme level of control that has led to many advanced Kondo experiments [61, 62, 63]. The second technique that enabled the study of individual Kondo spins was the STM, that was used to address individual magnetic atoms lying directly on top of and strongly interacting with a metal surface [64, 65]. Using either method, dI/dV measurements performed on the Kondo system yielded a strong resonance around zero bias voltage. As a hallmark of the Kondo effect, for $T > T_K$ the amplitude of the resonance decreases linearly with the logarithm of T . Its width in energy is a measure for the coupling strength of the Kondo spin to the bath and therefore also for T_K . Typically for magnetic atoms on a metal surface T_K ranges between 50 and 100 K [66], whereas in the quantum dots it can be tuned to values from about 1 K to < 50 mK [60].

Following these first demonstrations, other experimental systems have been found suitable for isolating and addressing an individual Kondo spin as well. These include carbon nanotubes [67, 68, 69] and single-molecule transistors constructed in electromigration junctions [70, 71].

4.2 The Kondo Effect of Co on Cu₂N

In the discussion above we have used an $S = \frac{1}{2}$ impurity. Without losing any of its applicability the model can be generalized to any system with a twofold degenerate ground state, as long as a single-electron process can cause it to switch, i.e. $|\Delta m| = 1$. However, the ground state of a system having $S > \frac{1}{2}$ is more-than-twofold degenerate, making the problem much more complicated. Therefore theoretical considerations of the Kondo effect are often limited to $S = \frac{1}{2}$. Although this assumption is justified for most quantum dot experiments, where the amount of spin on the dot is set precisely to $\frac{1}{2}$, this is not the case in general. Based on their d -shell populations, many magnetic elements have free-atom spin values that are higher and there is no reason to believe that these should all reduce to $\frac{1}{2}$ when the atom is placed upon a surface. Yet the $S = \frac{1}{2}$ model suffices for accurately explaining the Kondo results of such systems. In this section we will investigate this contradiction using the Kondo effect of an $S = \frac{3}{2}$ Co atom on Cu₂N.

4.2.1 Temperature Dependence

As we could already see in fig. 2.2, the spin excitation spectrum of Co on Cu₂N looks dramatically different from the ones obtained on Mn and Fe. The bold curve in fig. 4.1a, taken at 0.5 K, shows apart from a ‘regular’ spin excitation step at ± 5.5 mV a large resonance peak at zero bias. The portion of the spectrum

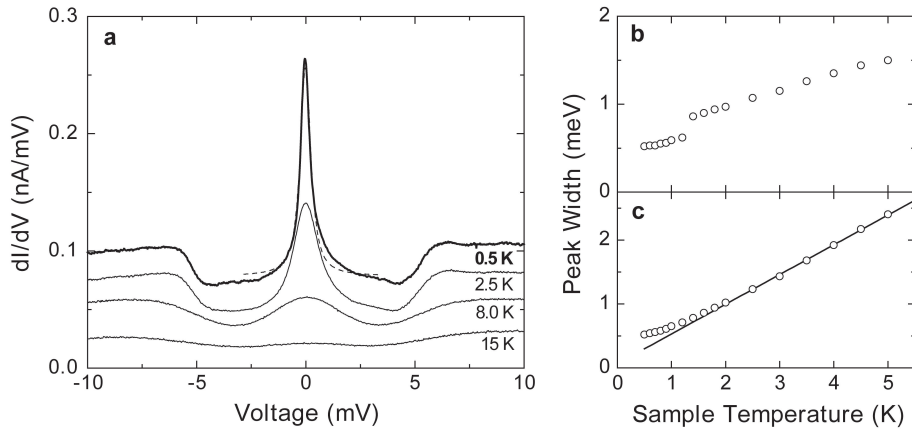


Figure 4.1: (a) Conductance spectra taken on a single Co atom on Cu₂N at various temperatures. Curves measured at temperatures higher than 0.5 K (thin lines) are offset by 0.025 nA/mV each. (b) Plot of the full widths at half maximum (FWHM) of the Lorentzian fits (obtained by deconvolution using the sample temperature) versus the sample temperature. (c) Similar as (b), but with the approximate tip temperature (0.5 and 1.8 K) used for deconvolution. At higher sample temperatures the plot approaches linear behavior (solid line).

between -3 and 3 mV can be fitted quite well with a thermally broadened Lorentzian (dashed curve), where we use $T = 0.5$ K for the broadening. The Lorentzian lineshape is one of the appearances of the Fano lineshape [72], which is characteristic for the observation of the Kondo effect in an STM configuration [64]. Measurements at higher temperatures are plotted as thinner lines.

Obtaining the Intrinsic Resonance by Deconvolution

In order to identify the peak as a Kondo resonance we should look for an intrinsic temperature dependence in its shape, i.e. a dependence that persist even if the effects of thermal broadening are removed. One quantity that is often plotted as function of temperature is the height of the (deconvoluted) peak, which should decrease linearly with the logarithm of the temperature with a low-temperature roll-off [70, 71]. For STM experiments this is not very useful as the tip height can vary from one measurement to the other because of the normalization condition imposed by the feedback loop. This complication makes the vertical scale of the spectrum uncertain. As an alternative one can also consider the intrinsic width of the spectroscopic feature, which in the case of a Kondo resonance should grow linearly with temperature and at very low temperature saturate at a value $\sim k_B T_K$ [60, 73].

Removing the effects of thermal broadening can be achieved by an iterative deconvolution procedure that involves repeatedly fitting the curve with a convoluted lineshape [73]:

$$\frac{dI}{dV}(V, T) \propto \int_{-\infty}^{\infty} \rho_s(\varepsilon, T) \frac{d}{dV} f(\varepsilon - eV, T) d\varepsilon. \quad (4.6)$$

Here $\rho_s(\varepsilon, T)$ is the intrinsic DOS of the sample we would like to extract (note that in case of a Kondo effect it can still depend on T), while we assume the tip DOS to be independent of either ε or T . The above expression also includes the Fermi-Dirac distribution function

$$f(\varepsilon, T) = \frac{1}{e^{\varepsilon/k_B T} + 1}, \quad (4.7)$$

the voltage-derivative of which is a Gaussian peak with full width at half maximum (FWHM) $3.2k_B T$. Apart from the temperature, also the voltage modulation we add to the bias for lock-in detection broadens the spectroscopic features. In the following, whenever we refer to deconvolution performed with a temperature T , we actually use an effective temperature giving rise to a Gaussian with an effective FWHM of $\sqrt{(3.2k_B T/e)^2 + (2\sqrt{2}V_{\text{mod}})^2}$ [74], where V_{mod} is the RMS modulation voltage (in this case $50 \mu\text{V}$).

In fig. 4.1b the full widths at half maximum of the deconvoluted Lorentzian fits are plotted against the temperature of the sample T_s (as read off from the thermometer mounted on the scanner), where for each curve T_s (combined with the modulation broadening) was used for the deconvolution. The plot shows a sharp discontinuity between 1.2 and 1.4 K, which corresponds to the switching

point between two different cooling methods: measurements at $T_s \leq 1.2$ K were performed in single-shot mode whereas at $T_s > 1.2$ K the ^3He was flowing continuously (section 1.4). This jump is likely to be caused by unequal tip and sample temperatures. Both the thermometer and the heater were thermally anchored strongly to the sample, whereas the tip was cooled almost directly by the liquid ^3He without being influenced much by heating. Therefore in many cases the temperature of the tip was much lower than the thermometer indicated. In the following paragraph we will discuss the influence of unequal tip and sample temperatures on the thermal broadening in tunneling spectroscopy and the proper treatment of this discrepancy in the deconvolution process.

Thermal Broadening with Unequal Temperatures

In general the net tunnel-current I flowing from tip to sample can be expressed as the difference between the currents caused by electrons tunneling from tip to sample $I_{t \rightarrow s}$ and vice versa $I_{s \rightarrow t}$ [74]:

$$\begin{aligned}
I &= I_{t \rightarrow s} - I_{s \rightarrow t} \\
&\propto \frac{4\pi e}{\hbar} \int_{-\infty}^{\infty} \left\{ \rho_t(\varepsilon - eV) \rho_s(\varepsilon) f(\varepsilon - eV, T_t) (1 - f(\varepsilon, T_s)) \right. \\
&\quad \left. - \rho_t(\varepsilon - eV) \rho_s(\varepsilon) f(\varepsilon, T_s) (1 - f(\varepsilon - eV, T_t)) \right\} d\varepsilon \\
&\propto \frac{4\pi e}{\hbar} \int_{-\infty}^{\infty} \rho_t(\varepsilon - eV) \rho_s(\varepsilon) (f(\varepsilon - eV, T_t) - f(\varepsilon, T_s)) d\varepsilon. \quad (4.8)
\end{aligned}$$

Here \hbar is the reduced Planck constant while $\rho_t(\varepsilon)$ and $\rho_s(\varepsilon)$ are the densities of states of the tip and sample respectively. Again $f(\varepsilon, T)$ is the Fermi-Dirac distribution function that in this case can depend on either tip temperature T_t or sample temperature T_s . In the above expression we assume that the tunneling matrix element coupling the tip and the sample is independent of energy (hence the proportionality sign). Taking the derivative to V we find:

$$\begin{aligned}
\frac{dI}{dV} &\propto \frac{4\pi e}{\hbar} \int_{-\infty}^{\infty} \left\{ \frac{d}{dV} [\rho_t(\varepsilon - eV)] \rho_s(\varepsilon) f(\varepsilon - eV, T_t) \right. \\
&\quad \left. + \rho_t(\varepsilon - eV) \rho_s(\varepsilon) \frac{d}{dV} [f(\varepsilon - eV, T_t)] \right. \\
&\quad \left. - \frac{d}{dV} [\rho_t(\varepsilon - eV)] \rho_s(\varepsilon) f(\varepsilon, T_s) \right\} d\varepsilon. \quad (4.9)
\end{aligned}$$

If we assume the tip DOS to be independent of energy and we once more allow the intrinsic DOS of the sample to depend on T_s , the expression reduces to:

$$\frac{dI}{dV} \propto \frac{4\pi e}{\hbar} \int_{-\infty}^{\infty} \rho_t \rho_s(\varepsilon, T_s) \frac{d}{dV} f(\varepsilon - eV, T_t) d\varepsilon. \quad (4.10)$$

Comparing this to (4.6), we see that remarkably, in absence of thermal equilibrium the thermal broadening is caused exclusively by the temperature of the tip, provided that its DOS is flat.

As no sensor was connected to the tip, we can only estimate its temperature. We will therefore assume that the tip was not sensitive to heating and adopted only two different temperatures; one corresponding to each cooling method. For the measurements taken in single-shot mode ($T_s \leq 1.2$ K) we use $T_t = 0.5$ K. As shown in fig. 4.1c, choosing $T_t = 1.8$ K for the continuous flow measurements ($T_s > 1.2$ K) causes the two segments of data points to line up very well¹. Now we see that the temperature dependence of the intrinsic width approaches linear behavior (with a slope of $5.4 \pm 0.1k_B$) at high temperatures, whereas at low temperature it saturates as expected for a Kondo resonance. If we follow the convention of choosing the zero-temperature FWHM of the resonance to be $2k_B T_K$ we find a Kondo temperature $T_K = 2.7 \pm 0.2$ K. For the extrapolation to zero temperature we assume the width – being determined by whichever is the highest of T_K and T_s – to go like $\sqrt{(2k_B T_K)^2 + (5.4k_B T_s)^2}$.

4.2.2 Why Co is Kondo-Screened

Now that we have established the presence of a Kondo resonance in Co on Cu_2N , the question arises why it appears in this specific case and why no such effect is observed in either Mn or Fe on Cu_2N . Let us therefore once more review the requirements for a Kondo effect. As discussed in section 4.1.1, in order for a spin to become Kondo-screened it needs to have a twofold degenerate ground state which is coupled to a bath of electrons. Also, the difference in the magnetization quantum number, $|\Delta m|$, should be equal to 1 in order to enable electrons to initiate the virtual switching process. In chapter 3 we found that both Mn and Fe have a negative axial anisotropy parameter D , causing the high $|m|$ values to be favored over the lower values. For Mn this leads to a twofold degenerate ground state with $|\Delta m| = 5$ while for Fe $|\Delta m| = 4$. Moreover, as in the latter case the transverse anisotropy parameter E is finite, the ground state of Fe is not even degenerate. So we find that for these two atoms Kondo behavior can be easily excluded based on their magnetic anisotropy. Similarly, the anisotropy of Co on Cu_2N can – as we will see in this section – explain why this particular atom does become Kondo-screened.

¹For continuous flow mode, 1.8 K is somewhat high (1.4 K would have been expected). However, forcing the tip temperature to 1.4 K in continuous flow would suggest it to become significantly smaller than 0.5 K in single shot which is highly unrealistic. Nonetheless, this freedom in fixing tip temperatures has been taken into account in determining the error in T_K . The larger than expected difference between the two T_t values does not influence our statement that this is a Kondo resonance. By choosing it to be 1.8 K for the $T_s = 1.4$ K peak we assign more of its width to thermal broadening, yet the remaining width is still much larger than that of the intrinsic $T_s = 0.5$ K resonance.

Kramers Degeneracy

Kramers' degeneracy theorem states that in an arbitrarily asymmetric but purely electrostatic (crystal) field, any system that consists of an odd number of electrons (and therefore has a half-integer spin) will remain at least twofold degenerate in the absence of a magnetic field [75]. This follows from the time reversal invariance of a Hamiltonian that describes an electrostatic field, of which our anisotropy Hamiltonian (3.3) is an example if we choose $\mathbf{B} = 0$. The consequence of this statement is that for Mn ($S = \frac{5}{2}$) and Co (which has $3d^7$, so probably $S = \frac{3}{2}$; we will verify this later) the zero-field degeneracy between states with equal $|m|$ cannot be broken by a finite E value unlike the case of Fe ($S = 2$).

It is illustrative to verify this theorem by perturbation theory. Since by definition $E \leq \frac{1}{3}D$ (otherwise the axes are reassigned), we will treat the transversal anisotropy term as a perturbation, i.e.:

$$\hat{\mathcal{H}} = \overbrace{-g\mu_B\mathbf{B} \cdot \hat{\mathbf{S}} + D\hat{S}_z^2}^{\hat{\mathcal{H}}_0} + \overbrace{E(\hat{S}_x^2 - \hat{S}_y^2)}^{\hat{\mathcal{H}}'}. \quad (4.11)$$

The eigenstates of $\hat{\mathcal{H}}_0$ are simply the $|m\rangle$ states, whereas in general $\hat{\mathcal{H}}'$ mixes these. Using $\hat{S}_{\pm} = \hat{S}_x \pm i\hat{S}_y$ we can rewrite the Hamiltonian to:

$$\hat{\mathcal{H}} = \hat{\mathcal{H}}_0 + \frac{E}{2}(\hat{S}_+^2 + \hat{S}_-^2). \quad (4.12)$$

Now it becomes evident that $\hat{\mathcal{H}}'$ to first order only couples states that have $\Delta m = \pm 2$ and to higher order only if $\Delta m = \pm 2n$, where n is an integer (this is why in the case of Fe the $|m| = 2$ states are split much less than the $|m| = 1$ states: it is only a higher order correction). So the perturbation mixes the $|m\rangle$ states, but does so only from two separate subgroups. For example, if $S = 2$ the resulting eigensystem will consist of three states that are linear combinations of $|+2\rangle$, $|+0\rangle$ and $|-2\rangle$ and two states that are linear combinations of $|+1\rangle$ and $|-1\rangle$. Here, original eigenstates with equal $|m|$ are coupled by the perturbation giving rise to avoided crossings, i.e. lifted degeneracies. But if $S = \frac{3}{2}$, the combinations are $|+\frac{3}{2}\rangle$ and $|-\frac{1}{2}\rangle$ on the one hand and $|+\frac{1}{2}\rangle$ and $|-\frac{3}{2}\rangle$ on the other, leaving the degeneracy in $|m|$ untouched. This is true for any half-integer spin and although here we have discussed it only in approximation, the result is exact and holds for any value of E .

The Role of Anisotropy

As we did before for Mn and Fe, we can use the spin excitation energies to determine the anisotropy parameters. In the zero-field spectrum of fig. 4.1a there is one pair of steps symmetrically at ± 5.5 mV (measurements up to ± 25 mV did not reveal additional excitations). Assuming that Co maintains its free-atom spin value of $S = \frac{3}{2}$ and taking Kramers degeneracy into account, these steps can either be assigned to $|\pm \frac{1}{2}\rangle \rightarrow |\pm \frac{3}{2}\rangle$ excitations if $D < 0$, or to

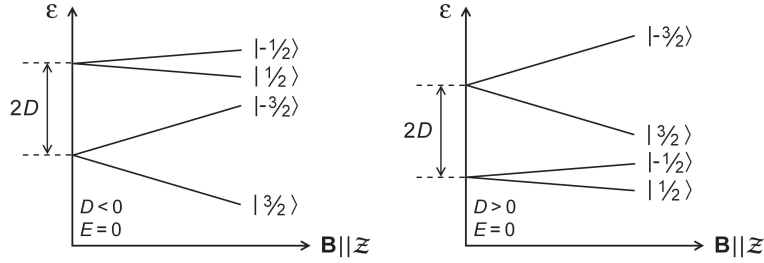


Figure 4.2: (a) Qualitative energy diagrams for an uniaxially anisotropic $S = \frac{3}{2}$ system with negative and positive values of D , with the field oriented along the unique axis. For $D > 0$, a low-energy $|\pm \frac{1}{2}\rangle$ Kramers doublet is formed.

$|\pm \frac{3}{2}\rangle \rightarrow |\pm \frac{1}{2}\rangle$ if $D > 0$ (for now we will neglect E as it cannot influence the zero-field excitations anyhow). Figure 4.2 shows qualitative energy diagrams for either situation. If D were negative, the situation would be very similar to Mn with a twofold degenerate ground state having $|\Delta m| = 3$. However, for $D > 0$ the two ground states are separated by $|\Delta m| = 1$: the ideal system for Kondo-screening!

In the next section we will show by field-dependent measurements that this interpretation (i.e. $S = \frac{3}{2}$, $D > 0$) is indeed correct. Not only does that make this the first report of a Kondo effect in a known high-spin (i.e. $S > \frac{1}{2}$) system, it also demonstrates the importance of magnetic anisotropy in enabling the Kondo effect. By breaking the degeneracy in $|m|$, the crystal field reduces the large spin into an effective $S = \frac{1}{2}$ Kramers doublet that can become Kondo-screened at low temperatures. This finding, which agrees with theoretical predictions on

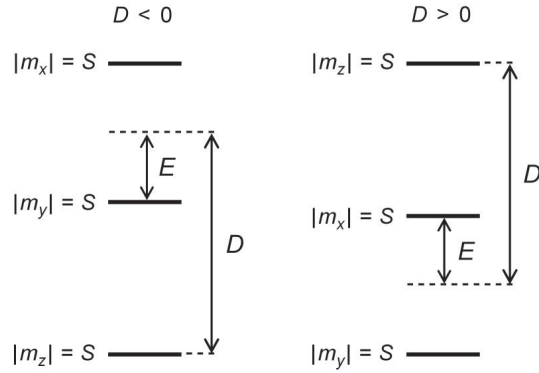


Figure 4.3: (a) Energy eigenvalues of (3.3) with $\mathbf{B} = 0$ and E just smaller than $|D|/3$ for negative and positive values of D , in case maximum magnetization is assigned to each of the primary axes. Physically the two situations are almost identical, yet one is labelled ‘easy-axis’ and the other ‘hard-axis’. This picture is valid for any $S > \frac{1}{2}$.

the role of anisotropy in a Kondo system [76, 77], implies that Co in a different environment might not show any Kondo effect at all. Similarly, atoms with half-integer spin that are not a Kondo system in one case (like Mn on Cu₂N) may become so in another situation. In fact, this could retrospectively explain previous findings in [18] where Mn atoms on Al₂O₃ islands on a NiAl surface were studied by spin excitation spectroscopy. Although no Kondo behavior was observed on most of them, some atoms (presumably Mn, as judged from their apparent height) that were located close to the edge of an island did show a zero-bias resonance that was attributed to Kondo-screening. This might very well be caused by a local change in the anisotropy energies.

The interpretation presented above also raises some questions. Because although each anisotropic system can be discretely labelled as either ‘easy-axis’ ($D < 0$) or ‘hard-axis’/‘easy-plane’ ($D > 0$), the boundary separating these two possibilities is quite subtle. In fig. 4.3 two situations are depicted schematically, each having an E -value that is only slightly smaller than $\frac{1}{3}|D|$ but with different signs of D . Physically the two situations are very close, except for rearrangement of the axes, yet according to our model one of them should result in a Kondo resonance and the other not at all. It is unclear how the system would precisely behave in this crossover region.

4.3 A Kondo Spin and Its Environment

When a sufficiently large magnetic field B is applied to a Kondo-screened spin, Zeeman splitting will lift the degeneracy in its ground state (4.2) as a result of which the Kondo effect is quenched. However, for smaller fields where the Zeeman energy is comparable to $k_B T_K$, what remains of the Kondo-resonance peak splits into two peaks. This was observed both in quantum dot [59, 60] and STM Kondo systems [18]. The effect of a magnetic field can be incorporated into the Anderson Hamiltonian (4.1) by making ε_f spin-dependent: $\varepsilon_{f\uparrow} = \varepsilon_{f0} - \Delta\varepsilon/2$ and $\varepsilon_{f\downarrow} = \varepsilon_{f0} + \Delta\varepsilon/2$, where $\Delta\varepsilon$ is the Zeeman energy. Calculations based on this model predict the splitting between the peaks in the DOS to be $2\Delta\varepsilon$ [78, 79]. Although these calculations are beyond the scope of this thesis, we can verify their result through a simple model.

Let us start in state $|d_{\downarrow}^1\rangle$ which is $\Delta\varepsilon = g\mu_B B$ higher in energy than the ground state $|d_{\uparrow}^1\rangle$. We will now flip its spin by performing one of the virtual processes of (4.3):

$$|d_{\uparrow}^1\rangle = \hat{c}_{\mathbf{k}'\downarrow}^\dagger \hat{d}_{\downarrow} \hat{d}_{\uparrow}^\dagger \hat{c}_{\mathbf{k}\uparrow} |d_{\downarrow}^1\rangle. \quad (4.13)$$

The energy that was lost by the impurity spin during this process has been absorbed by the bath in the form of an electron-hole excitation. In order to get back to the original situation we can for example perform the following operation:

$$|d_{\downarrow}^1\rangle = \hat{d}_{\downarrow}^\dagger \hat{c}_{\mathbf{k}'\downarrow} \hat{c}_{\mathbf{k}\uparrow}^\dagger \hat{d}_{\uparrow} |d_{\uparrow}^1\rangle, \quad (4.14)$$

where the impurity reclaims the lost energy from the bath by destroying the electron-hole pair. Note that during the entire exercise the whole system was

excited by $g\mu_B B$. If we would have started in the true ground state of the system $|d_{\uparrow}^1\rangle$ (and the Fermi sea unexcited), none of the above could happen because the impurity has no source to extract energy from. The Kondo resonance therefore takes place at an energy $\varepsilon_F + g\mu_B B$, but since the situation is electron-hole symmetric (because we chose the energy to ionize the impurity to be $U/2$ either way) it shows up as two peaks at $V = \pm g\mu_B B/e$ in the conductance spectrum.

Incidentally, those are exactly the positions where we expect to find the dI/dV steps in spin excitation spectroscopy. Of course that is not surprising: after all it is the same spin excitation that now occurs resonantly *at* the excitation energy rather than driven by tunneling electrons *at and beyond* the excitation energy. Therefore it appears as a peak rather than a step in the differential conductance. Consequently we can expect the split peaks to follow the positions of the spin-excitation steps whenever the excitation energies are changed. In the remainder of this chapter we will verify this hypothesis by modifying the excitations through various environmental factors. First we will study the evolution of the peak positions under the influence of a magnetic field in combination with the strong magnetic anisotropy that the Cu_2N surface provides. In section 4.3.2 other atomic spins will be placed near the Kondo-screened Co atom, giving rise to changes in the excitation spectra due to spin-coupling.

4.3.1 Anisotropic Field Dependence

Figures 4.4b-d show spin excitation spectra taken on individual Co atoms, each corresponding to a different field direction. As expected the peak splits into two, but the rate at which it splits depends strongly on the field direction. Plotting the observed excitation energies against the field strength (fig. 4.5) suggests that whereas the $\mathbf{B} \parallel x$ and $\mathbf{B} \parallel z$ directions yield very similar spectra, both the step and peak positions are markedly different for $\mathbf{B} \parallel y$. Such anisotropic field dependence of the Kondo peak positions has not been observed before and is a noteworthy result that is directly related to the high-spin nature of the system. A true $S = \frac{1}{2}$ system cannot be sensitive to magnetic anisotropy as presented in (3.3) because none of the second-order $|\Delta m| = 1$ terms can link the $|\pm \frac{1}{2}\rangle$ eigenstates. So even though the crystal field has reduced the Co spin to an *effective* spin $\frac{1}{2}$ as far as creating a Kondo system is concerned, it clearly still carries the signature of a true high-value spin.

Since we want to use these spectra for studying the relation of the peak positions to the underlying excitation energies, we will mainly use the step positions for determining the anisotropy parameters of Co on Cu_2N . Especially when taking into account the $\sim 5\%$ variations in the excitation energies that were encountered between different atoms of the same kind in chapter 3, we can consider the $\mathbf{B} \parallel x$ and $\mathbf{B} \parallel z$ dependence to be sufficiently equal to model this system exclusively with uniaxial anisotropy (i.e. $E = 0$ and $\mathcal{Z} = y$). However, it is important to realize once more that even if E would have been finite, Kramers' theorem would have prevented it from harming the degeneracy needed for Kondo-screening. Fitting the step positions to the energy of the

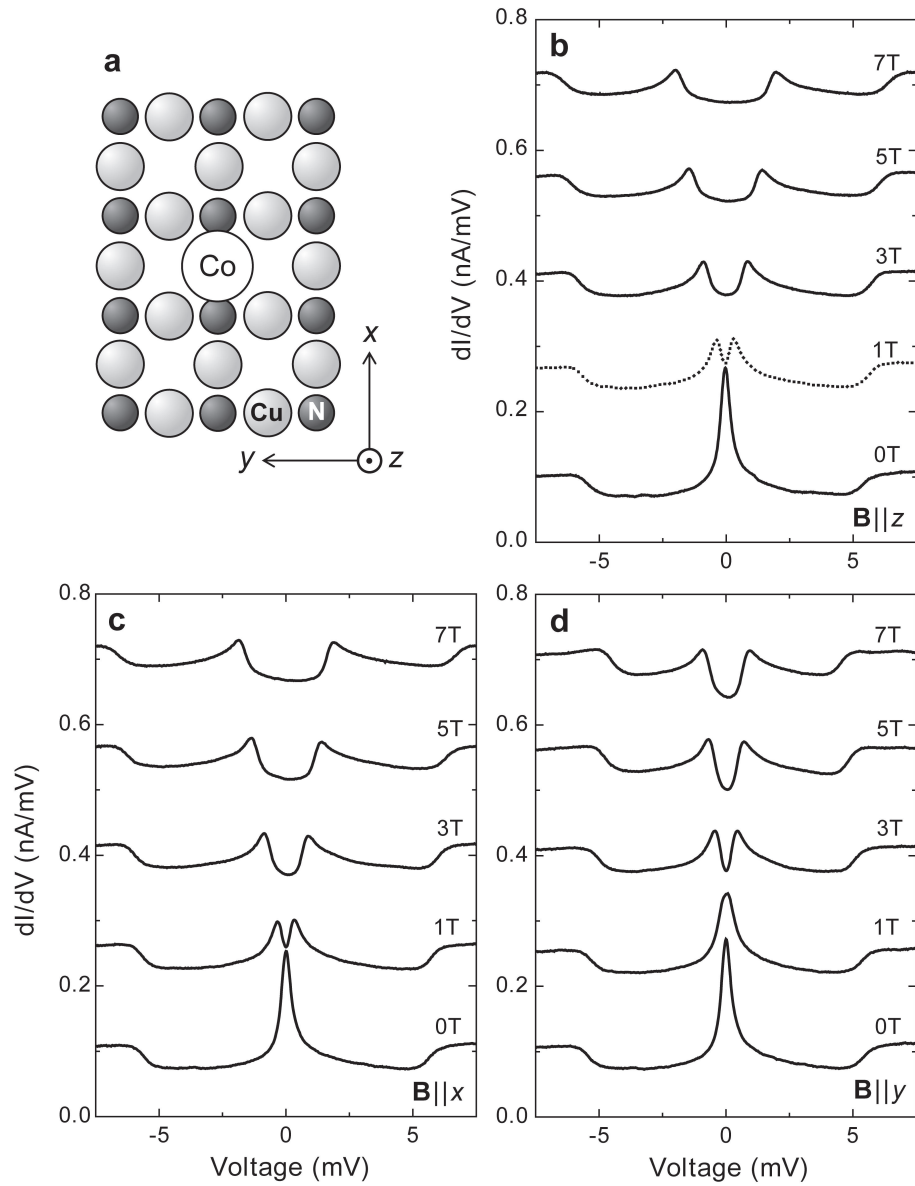


Figure 4.4: (a) Axis-assignment for Co on Cu₂N (identical to what was used earlier for Mn and Fe). (b–d) dI/dV -spectra on individual Co atoms in various magnetic fields oriented along z , x and y in (b), (c) and (d) respectively. Curves corresponding to non-zero fields are offset by 0.15 nA/mV. The dotted spectrum in (b) was measured on a different atom than those with other field strengths in the same direction.

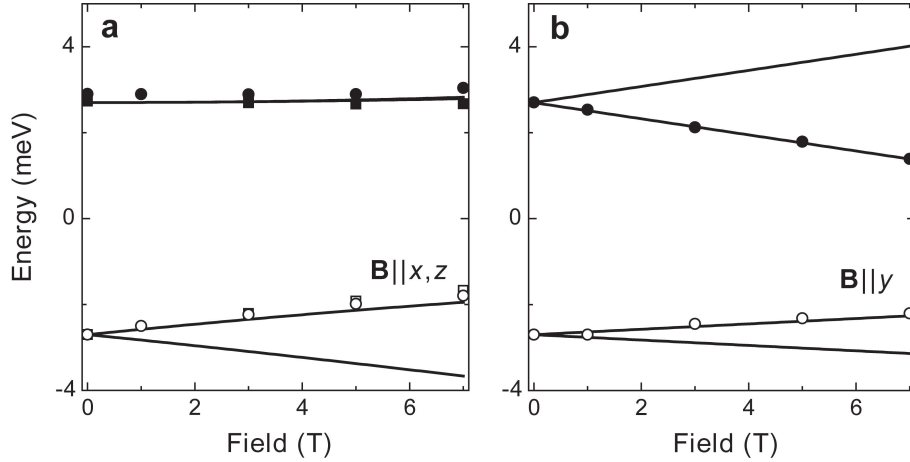


Figure 4.5: Graphs of the peak and step positions taken from fig. 4.4b–d against the field strength for $\mathbf{B} \parallel x$ (circles) and $\mathbf{B} \parallel z$ (squares) in (a) and $\mathbf{B} \parallel y$ in (b). Peak (step) positions are indicated by open (filled) symbols. For the x and z -directions the peak positions are quite similar and therefore hard to distinguish. In contrast to the graphs presented in chapter 3 showing directly the measured excitation energies, here the final energies at the end of the excitation process are plotted: each data point indicates a measured excitation energy added to the calculated ground state energy at the corresponding field. Accordingly, the solid lines show the calculated eigenenergies (rather than the calculated excitation energies as before).

second excitation yields² $g = 2.1 \pm 0.2$ and $D = 2.7 \pm 0.1$ meV, indicating that our reasoning in section 4.2.2 – which was based on hard-axis anisotropy ($D > 0$) – was indeed correct. The solid lines in fig. 4.5 show the calculated eigenenergies of the anisotropy Hamiltonian for these values.

At this point we turn to the field dependence of the peaks in the spectra. According to our understanding of the Kondo effect, the peaks should closely follow the $|+\frac{1}{2}\rangle \rightarrow |-\frac{1}{2}\rangle$ excitation energies. As can be seen from the open symbols in fig. 4.5 they do so very well for all field directions. The data points seem to be consistently slightly high compared to the calculated energy, but this might result from the fact that the maximum of a peak that is superimposed on top of an upward step (which should still be there) is shifted towards higher values. Although not surprising, this result is quite remarkable: the entire model we used to calculate the transition energies was based on the anisotropy of a single spin in a one-particle picture, yet it precisely captures the behavior of the many-body Kondo system.

²The error margins here are much larger than for Mn and Fe. This probably results from forcing E to be 0. Leaving E free as a fit-parameter unfortunately does not resolve this problem, since the $|+\frac{1}{2}\rangle \rightarrow |+\frac{3}{2}\rangle$ energy is very insensitive to changes in E which can therefore not be determined. However, the choice of $E = 0$ is justified by the similarity of the $|+\frac{1}{2}\rangle \rightarrow |-\frac{1}{2}\rangle$ excitations (i.e. the peaks) – which are sensitive to transverse anisotropy – in the $\mathbf{B} \parallel x$ and $\mathbf{B} \parallel z$ measurements.

4.3.2 Coupled Kondo Systems

Having studied the interplay of a Kondo-screened spin with nonmagnetic atoms (i.e. the crystal field), we now shift our attention to the influence of magnetic atoms on a Kondo impurity. Similar studies in quantum dots [80] and electromigration junctions [81] have shown remarkable changes in the properties of a Kondo system through spin-spin coupling. The ease with which vertical atom manipulation can be performed on Cu_2N makes this an ideal surface for doing such experiments in an STM configuration. Here we will discuss various measurements performed on a class of atomic structures that exhibit spin-coupling that is of the proper strength to compete with the effects of magnetic anisotropy and Zeeman splitting.

Weak Coupling Through Vacancies

As shown schematically in fig. 4.6a, a magnetic atom “X” (which can be Fe, Mn or Co) and a Co atom are separated by 7.2 \AA along a vacancy row. Such a structure is built by first positioning either one of the atoms on a Cu site and then placing the second atom on one of the two N sites closest to the desired final position (dashed circle in the figure, assuming the Co atom was positioned first). Finally the atom is hopped in place by a 1.5 V pulse (see section 2.3.3) with $\sim 50 \%$ success rate³. In the following we will refer to such structures using the shorthand “ $\text{X}_{\text{vv}}\text{Co}$ ” (where the v’s correspond to the two vacancy sites between the atoms).

These nano-engineered structures differ in three ways from those used in earlier spin-coupling studies on Cu_2N [19], where **(1)** the inter-atomic spacing was half as large, i.e. 3.6 \AA , **(2)** the atoms were positioned along a N-row rather than a v-row and **(3)** all atoms were identical (Mn). In that situation the atoms were coupled quite strongly (because of their proximity as well as the high electron density along the N-rows) as a result of which they formed one entity, both in topography and in spectroscopy. Also, once constituted the structures could not be controllably disassembled. In contrast, in a topograph of the current dimers (fig. 4.6b) one can clearly recognize each constituent atom. Each of these can be removed without causing lasting damage and be replaced by a different atom at will. As we will see shortly, at these relative positions the two atoms produce individual excitation spectra that still resemble those of the corresponding single atoms and the effects of spin-coupling on the Co atom are comparable in magnitude to the field-induced splitting of the previous section.

In fig. 4.6b we see three vertically oriented dimers: a $\text{Mn}_{\text{vv}}\text{Co}$ (atoms 1 and 2), a $\text{Fe}_{\text{vv}}\text{Co}$ (atoms 3 and 4) and a $\text{Co}_{\text{vv}}\text{Co}$ structure (atoms 5 and 6). The horizontally oriented dimer on the central island is $\text{Co}_{\text{vv}}\text{Co}$ as well. Each combination was built in both orientations to enable field-direction dependent measurements (in the current image the magnetic field was oriented vertically). In addition each structure was built once more on a sample where the field was

³We did not perform statistics on the success rate of hopping so this number is based on general impression. If any, there might be a slight bias in favor of success.

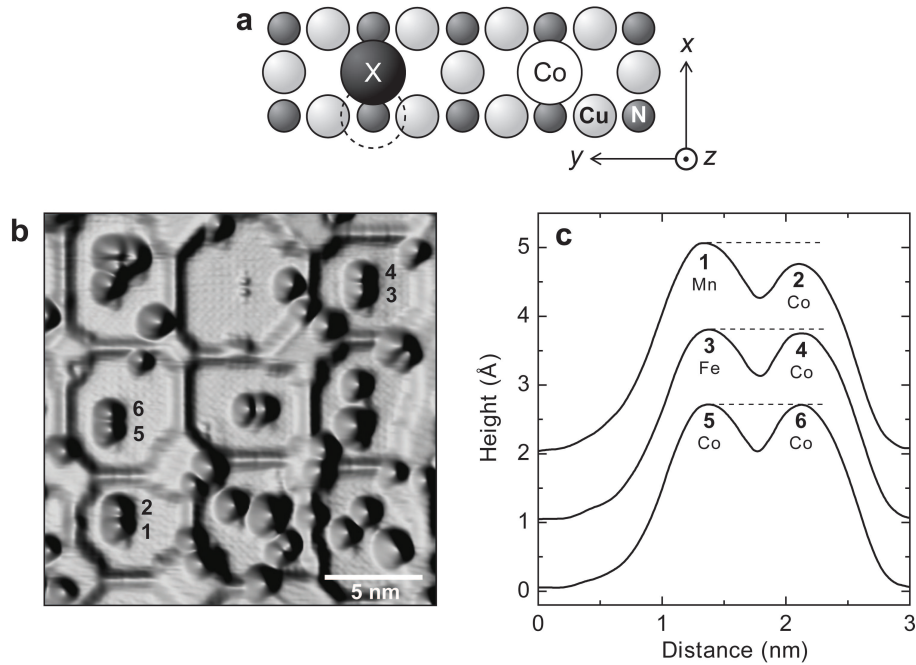


Figure 4.6: (a) Structural drawing of the $X_{vv}Co$ dimer with axis-assignments. The dashed circle indicates where the second atom has to be put down in case the Co atom was positioned first. (b) Topographic image (20×20 nm, 10 mV/1 nA) showing four dimers on separate Cu_2N islands: one $Mn_{vv}Co$ (atoms 1 and 2), one $Fe_{vv}Co$ (atoms 3 and 4) and two $Co_{vv}Co$'s (atoms 5 and 6 and the structure on the central island). (c) Height profiles taken from (b) in vertical direction. The zero of the lower profile corresponds to the surface of the Cu_2N island; the other two are offset by 1 Å each. The dashed lines are meant as a guide to compare the apparent heights of the atoms.

oriented perpendicular to the surface. All dimers were placed such that no lattice defect, island edge or other adatom was present within a range of 14.4 \AA (i.e. 4 unit cells). As fig. 4.6c shows, the apparent height (at 10 mV/1 nA) of the Fe and Co atoms was nearly identical whereas that of Mn was slightly higher. Because the combination of two Kondo-screened spins in the $Co_{vv}Co$ structures introduces an extra complication we will first focus on the effects of coupling non-Kondo spins to Co.

The World's Tiniest Compass

The lowest curves in fig. 4.7 show the zero-field spectra for each of the two atoms in $Fe_{vv}Co$ (for this the same atom-lock procedure was used as discussed in section 2.3.1 for measurements on individual atoms). Although the typical Co spectrum can still be recognized by its spin excitation steps, the central Kondo feature has changed dramatically: the resonance peak seems to have split

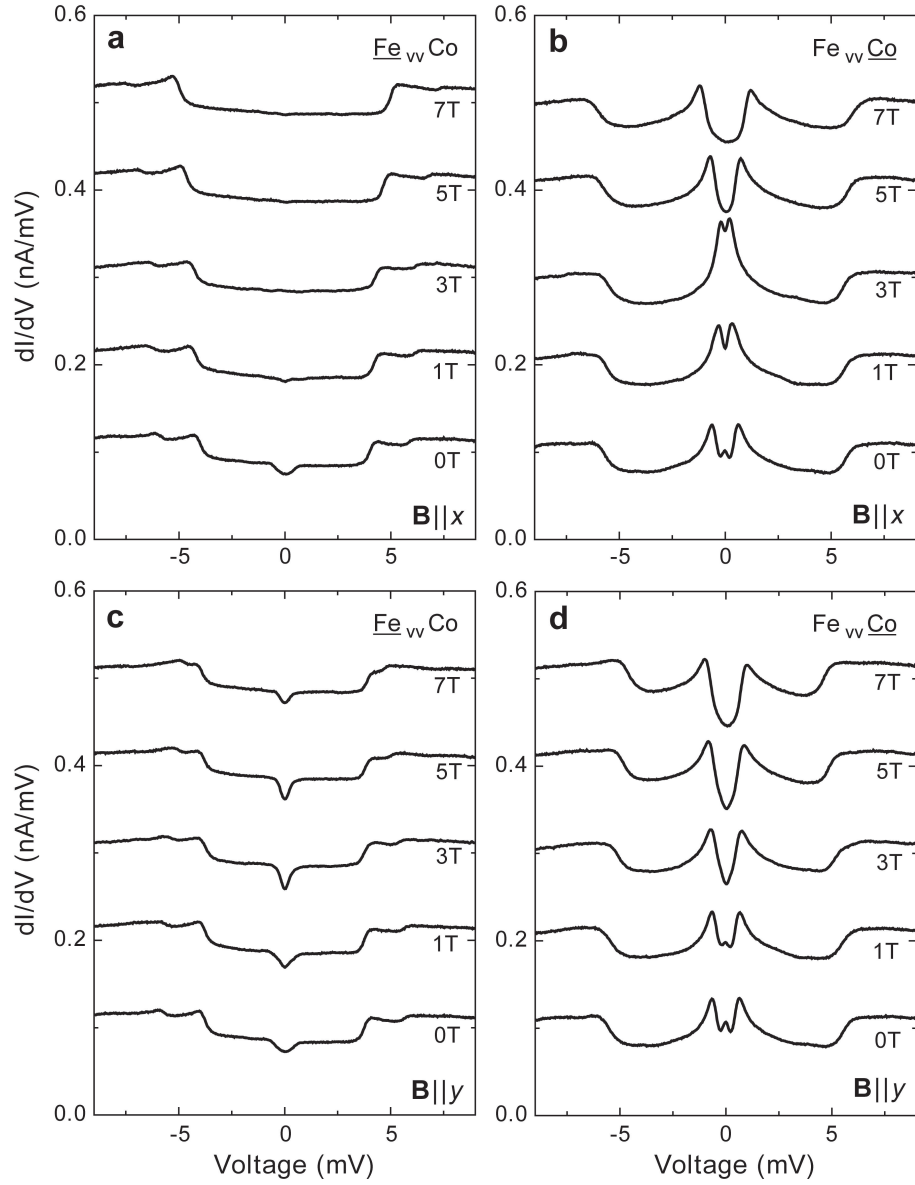


Figure 4.7: dI/dV -spectra measured on $\text{Fe}_{\text{v}}\text{Co}$ when the tip was positioned over the Fe atom (**a**, **c**) and Co atom (**b**, **d**) at various magnetic fields oriented along x (**a**, **b**) and y (**c**, **d**).

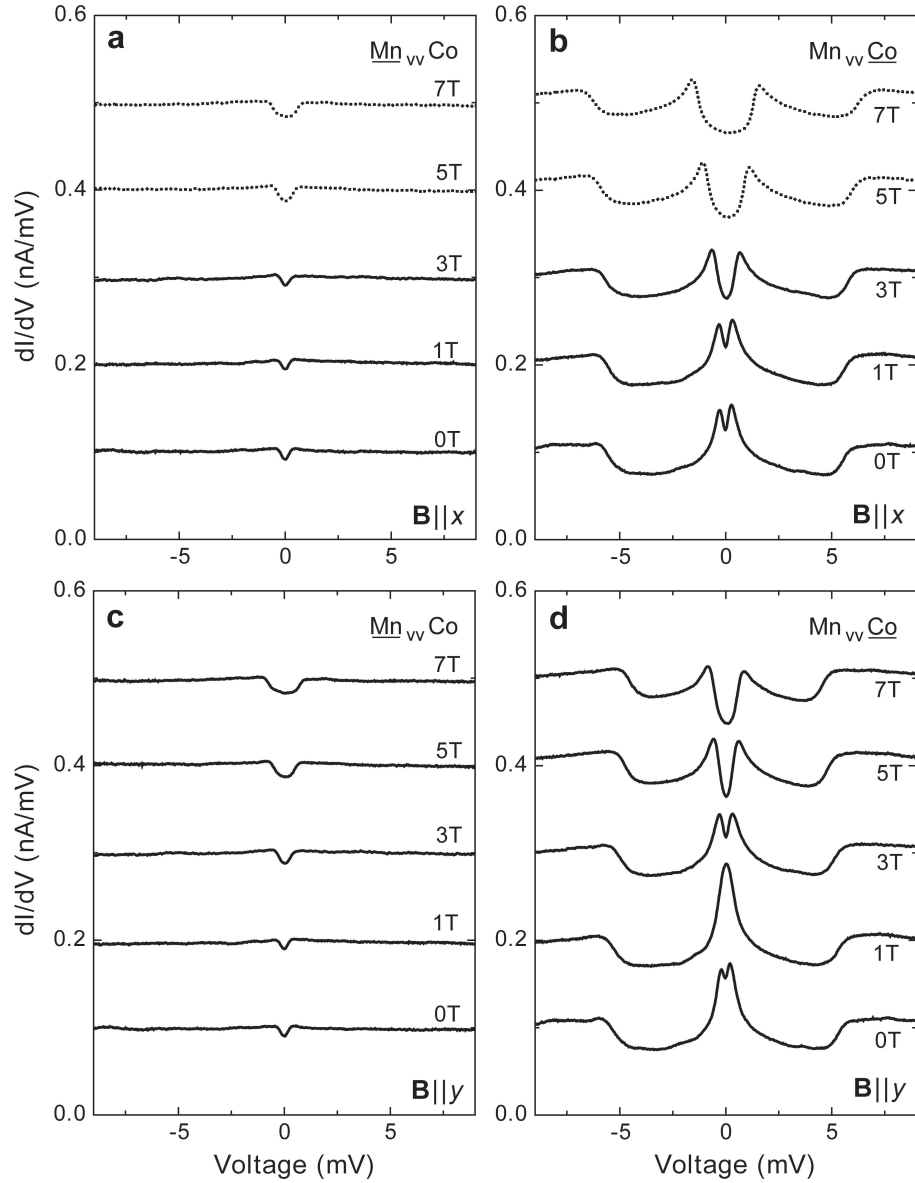


Figure 4.8: dI/dV -spectra measured on $Mn_{vv}Co$ with the tip over the Mn atom (**a, c**) and Co atom (**b, d**) at various magnetic fields oriented along x (**a, b**) and y (**c, d**). Dotted spectra were taken on a different structure (identical but built elsewhere on the Cu_2N surface) than those with other field strengths in the same direction.

and a small extra peak has appeared at zero-bias. If we neglect this central peak for now (it will be taken into consideration further on) it looks like the proximity of the Fe atom is experienced by the Co atom as an effective magnetic field.

This interpretation is confirmed surprisingly well by measurements at finite fields. If $\mathbf{B} \parallel x$ (i.e. measured on the horizontal structure in fig. 4.6b) the separation between the two peaks decreases until $B \simeq 2$ T after which it grows again. If however $\mathbf{B} \parallel y$ no such crossing occurs: the separation stays roughly constant and grows only slightly beyond $B \sim 3$ T. Measurements at $\mathbf{B} \parallel z$ (to be discussed further on⁴ in chapter 5, fig. 5.11a) indicate qualitatively similar behavior as for $\mathbf{B} \parallel y$. So it seems as if the external magnetic field is able to cancel the effect induced by the Fe atom’s effective field if it is oriented along x , but cannot do so in the other directions. The Co atom experiences a net field $B_{\text{net}} = |\mathbf{B} + \mathbf{B}_{\text{eff}}|$, where the effective field \mathbf{B}_{eff} points in the opposite direction of the external magnetic field’s x -component. As a result $B_{\text{net}} = B - B_{\text{eff}}$ if $\mathbf{B} \parallel x$ and $B_{\text{net}} = \sqrt{B^2 + B_{\text{eff}}^2}$ if $\mathbf{B} \perp x$. This result is in excellent agreement with our knowledge of Fe: in chapter 3 we found that the spin of an individual Fe atom on Cu_2N has the x -axis as its easy-axis along which it likes to magnetize even in the absence of an external magnetic field. If an external field is applied the Fe spin will always align with its x -component and therefore by symmetry the field lines of the Fe atom’s field must oppose the external field’s x -component at the position of the Co atom.

This qualitative ‘effective field’ picture also fits reasonably well for the results on $\text{Mn}_{\text{v}}\text{Co}$ (figs. 4.8 and 5.11b). Here the peaks cross around $B \simeq 1$ T if $\mathbf{B} \parallel y$ or $\mathbf{B} \parallel z$ but repel each other if $\mathbf{B} \parallel x$. With the exception of the crossing when $\mathbf{B} \parallel y$, again this agrees with our finding that Mn has an easy-axis along z . It should be noted, however, that the anisotropy energy of Mn is much weaker than that of Fe ($D = -0.039$ meV and -1.55 meV respectively). Therefore the preferred magnetization direction of the Mn spin might be more easily disturbed by a perpendicular field.

Thus a single Co atom acts as the world’s tiniest compass: it locally probes the direction and strength of the magnetic field around a single atomic spin. Clearly this picture is highly simplistic and incomplete in many ways: the concept of field lines is not applicable to quantum spins, the atoms can no longer be treated individually and as we will discuss in section 4.4 the dipolar field of such a spin system would be far too weak to be measured at a distance of 7.2 \AA . Yet the concept of such an effective magnetic field beautifully captures the essence of these experiments. It demonstrates the stunning amount of control with which individual atoms can be handled and proves that even deep inside the realm of quantum mechanics, as a first approximation our classical intuition may still guide us. And, as we will see shortly, it certainly is not incorrect.

⁴These measurements were performed with a special tip that will not be discussed until section 5.3. However, this is not expected to influence the energies at which the peaks and steps are encountered.

4.3.3 Full Heisenberg Model

In this section we will try to model the spin-coupled systems of the previous section quantitatively by combining the Zeeman effect, magneto-crystalline anisotropy and spin-coupling in one Hamiltonian. In order to do so we need to merge two spin systems that in general have Hilbert spaces with different dimensionalities. For this purpose we will use tensor multiplication as discussed in [82]. If for example we combine an $S = \frac{1}{2}$ system and an $S = 1$ system, being described by spin-state vectors

$$|m_a\rangle = \begin{pmatrix} a_1 \\ a_2 \end{pmatrix} \quad \text{and} \quad |m_b\rangle = \begin{pmatrix} b_1 \\ b_2 \\ b_3 \end{pmatrix}, \quad (4.15)$$

all resulting states are represented by the tensor product of $|m_a\rangle$ and $|m_b\rangle$:

$$|m_a\rangle \otimes |m_b\rangle = \begin{pmatrix} a_1 b_1 \\ a_1 b_2 \\ a_1 b_3 \\ \hline a_2 b_1 \\ a_2 b_2 \\ a_2 b_3 \end{pmatrix} \equiv |m_a m_b\rangle. \quad (4.16)$$

Here the horizontal line only acts as a guide to the eye and has no algebraic significance. Similarly one can tensor-multiply operators, e.g. \hat{A} (2×2) working on $|m_a\rangle$ and \hat{B} (3×3) working on $|m_b\rangle$:

$$\hat{A} \otimes \hat{B} = \begin{pmatrix} A_{11}\hat{B} & | & A_{12}\hat{B} \\ \hline A_{21}\hat{B} & | & A_{22}\hat{B} \end{pmatrix}, \quad (4.17)$$

where the A_{mn} 's refer to the matrix elements of \hat{A} . If we want to perform an operation on only one of the spins we should tensor-multiply with the identity $\hat{\mathbb{I}}$ on the other side, e.g.:

$$\begin{aligned} (\hat{S}_y |m_a\rangle) \otimes |m_b\rangle &= (\hat{S}_y \otimes \hat{\mathbb{I}}) |m_a m_b\rangle = \begin{pmatrix} 0 & -i \\ i & 0 \end{pmatrix} \otimes \begin{pmatrix} 1 & 0 & 0 \\ 0 & 1 & 0 \\ 0 & 0 & 1 \end{pmatrix} |m_a m_b\rangle \\ &= \begin{pmatrix} & | & -i \\ & | & -i \\ & | & -i \\ \hline i & | & \\ & | & i \\ & | & i \end{pmatrix} |m_a m_b\rangle \equiv \hat{S}_y^{(a)} |m_a m_b\rangle. \end{aligned} \quad (4.18)$$

Similarly, $\hat{S}_y^{(b)} |m_a m_b\rangle \equiv (\hat{\mathbb{I}} \otimes \hat{S}_y) |m_a m_b\rangle$, where now \hat{S}_y is the corresponding

spin operator with the dimension of $|m_b\rangle$. Using this formalism we can begin constructing our Hamiltonian. As in [19] we will model the interaction between the two spins with an isotropic Heisenberg coupling term:

$$\hat{\mathcal{H}} = J\hat{\mathbf{S}}^{(a)} \cdot \hat{\mathbf{S}}^{(b)} = J\left(\hat{S}_x^{(a)}\hat{S}_x^{(b)} + \hat{S}_y^{(a)}\hat{S}_y^{(b)} + \hat{S}_z^{(a)}\hat{S}_z^{(b)}\right), \quad (4.19)$$

where J is the coupling constant. The spins tend to align ferromagnetically for $J < 0$ whereas $J > 0$ leads to antiferromagnetic relative orientation.

Let us start with the case of $\text{Fe}_{\text{v}}\text{Co}$. Combining (4.19) with the Zeeman and anisotropy terms (3.3) for each of the two spins we can form the following Hamiltonian⁵:

$$\begin{aligned} \hat{\mathcal{H}} = & J\hat{\mathbf{S}}^{(\text{Fe})} \cdot \hat{\mathbf{S}}^{(\text{Co})} - \mu_B\mathbf{B} \cdot \left(g_{\text{Fe}}\hat{\mathbf{S}}^{(\text{Fe})} + g_{\text{Co}}\hat{\mathbf{S}}^{(\text{Co})}\right) \\ & + D_{\text{Fe}}\hat{S}_x^{2(\text{Fe})} + E_{\text{Fe}}\left(\hat{S}_y^{2(\text{Fe})} - \hat{S}_z^{2(\text{Fe})}\right) + D_{\text{Co}}\hat{S}_y^{2(\text{Co})}. \end{aligned} \quad (4.20)$$

Note that here we have adopted the axis assignments that we found for the single atoms: $(\mathcal{X}, \mathcal{Y}, \mathcal{Z}) = (y, z, x)$ for Fe and $\mathcal{Z} = y$ for Co. Again, we choose to model Co with uniaxial anisotropy (i.e. $E_{\text{Co}} = 0$). During the following analysis we will allow the other anisotropy parameters D_{Co} , D_{Fe} and E_{Fe} , as well as g_{Co} and g_{Fe} to deviate no more than 5% from their single atom values. This way the Heisenberg coupling parameter J remains as the only fully free fitting parameter of (4.20). Since the $\text{Fe}_{\text{v}}\text{Co}$ system has 20 eigenstates it is very difficult to fit all excitation energies simultaneously via an automated routine. The presented ‘fits’ were found by manually adjusting the parameter values and can therefore not be guaranteed to be optimal. However, we will see that the results are very convincing and cannot be far off.

The Low-Energy Case: One Spin Fixed

In fig. 4.9 the first four calculated energy levels, obtained by diagonalization of (4.20), are plotted for $J = 0.13$ meV and $\mathbf{B} \parallel x$ together with the peak positions extracted from fig. 4.7b (still neglecting the central peak). Except for an avoided crossing around 1.1 T, caused by the finite value of E_{Fe} , the diagram consists of two pairs of diverging levels that are shifted vertically relative to each other by $\sim J$. According to these pairs we label the states $|\psi_{\alpha 0}\rangle$, $|\psi_{\alpha 1}\rangle$, $|\psi_{\beta 0}\rangle$ and $|\psi_{\beta 1}\rangle$. Obviously this labelling is not defined at the avoided crossing, but we will only use it for field values well away from it. Due to the difference in slopes we see that at 2.1 T the ground state switches from $|\psi_{\alpha 0}\rangle$ to $|\psi_{\beta 0}\rangle$.

These four levels can almost entirely be expressed within the subspace spanned by the eight $|m_{\text{Fe}}| = 2$ states, i.e. $|m_{\text{Fe}} m_{\text{Co}}\rangle = |\pm 2 \pm \frac{1}{2}\rangle$ and $|\pm 2 \pm \frac{3}{2}\rangle$ where the m ’s refer to the eigenvalues of $\hat{S}_x^{(\text{Fe})}$ and $\hat{S}_x^{(\text{Co})}$. Table 4.1 lists the corresponding coefficients both for $B = 0$ T and for 4 T along x . Here some small

⁵For terms like $\hat{S}_x^{2(\text{Fe})}$ it does not matter whether the square is taken before or after the tensor product, i.e. $(\hat{S}_x \otimes \hat{\mathbb{1}})^2 = \hat{S}_x^2 \otimes \hat{\mathbb{1}}$.

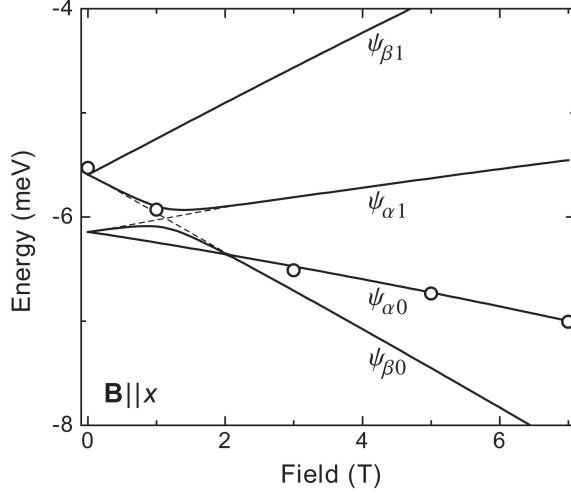


Figure 4.9: Lowest four eigenvalues of (4.20) with $J = 0.13$ meV, $g_{\text{Fe}} = 2.11$, $g_{\text{Co}} = 2.16$, $D_{\text{Fe}} = -1.53$ meV, $E_{\text{Fe}} = 0.31$ meV and $D_{\text{Co}} = 2.70$ meV for $B = 0$ to 7 T along x . Two crossing dashed lines indicate what the energy levels would be like if $E_{\text{Fe}} = 0$. The levels are labelled according to this situation: $\{\psi_{\alpha 0}, \psi_{\alpha 1}, \psi_{\beta 0}, \psi_{\beta 1}\}$ with ascending energy at $B = 0$. Open circles indicate the positions where peaks were encountered in the corresponding spectra of fig. 4.7b, all plotted with respect to the calculated ground state (i.e. as in fig. 4.5). Here the small zero-bias peak in the 0 T spectrum was omitted.

contributions of $m_{\text{Fe}} = 0$ resulting from finite E_{Fe} are neglected, the largest matrix element of which is 0.16. From the coefficients we can see that at either value of B the strongly diverging levels $|\psi_{\beta 0}\rangle$ and $|\psi_{\beta 1}\rangle$ have most weight in states where the two spins have parallel orientation (remember that the expectation value is the square of the matrix element), whereas $|\psi_{\alpha 0}\rangle$ and $|\psi_{\alpha 1}\rangle$ are mostly oriented antiparallel. Note that the higher values of $|m_{\text{Co}}|$ are preferred over the lower ones because \mathbf{B} points in the x -direction which is part of the easy-plane of Co.

The peak positions that were measured over the Co atom, the data points in fig. 4.9, coincide very well with $|\psi_{\alpha 0}\rangle \rightarrow |\psi_{\beta 0}\rangle$ excitations when $B < 2.1$ T, while above the change of ground state they closely follow $|\psi_{\beta 0}\rangle \rightarrow |\psi_{\alpha 0}\rangle$. This is not surprising since the $|\psi_{\alpha 0}\rangle$ and $|\psi_{\beta 0}\rangle$ states are almost identical through inversion of m_{Co} : by parking the tip over the Co atom we can flip its spin from antiparallel to parallel or vice versa with respect to the Fe atom's spin, while leaving the Fe spin itself untouched. Access to the other two states, $|\psi_{\alpha 1}\rangle$ and $|\psi_{\beta 1}\rangle$, requires exciting the Fe spin and can therefore not be gained while the tip is over the Co atom. At $B = 2.1$ T the ground state is incidentally degenerate as a result of which the Co spin can once more become Kondo-screened, leading to the reconstructed resonance peak we observed. This effect is not found if the tip is positioned over the Fe atom because in that situation the electrons do not tunnel directly into the resonance, which takes place only on the Co atom.

Table 4.1: Projection of eigenvectors for $\text{Fe}_{\text{v.v}}\text{Co}$, obtained by diagonalization of (4.20) with $J = 0.13$ meV, $g_{\text{Fe}} = 2.11$, $g_{\text{Co}} = 2.16$, $D_{\text{Fe}} = -1.53$ meV, $E_{\text{Fe}} = 0.31$ meV, $D_{\text{Co}} = 2.70$ meV and $B = 0$ T and 4 T along x , on the subspace of $|m_{\text{Fe}} m_{\text{Co}}\rangle$ states with $|m_{\text{Fe}}| = 2$. Matrix elements outside this subspace are no larger than 0.16. The states are labelled based on their physical significance rather than their eigenvalues (fig. 4.9): $\{\psi_{\alpha 0}, \psi_{\alpha 1}, \psi_{\beta 0}, \psi_{\beta 1}\}$ with ascending energy at $B = 0$ T and $\{\psi_{\beta 0}, \psi_{\alpha 0}, \psi_{\alpha 1}, \psi_{\beta 1}\}$ with ascending energy at $B = 4$ T.

State	$ +2+\frac{3}{2}\rangle$	$ +2+\frac{1}{2}\rangle$	$ +2-\frac{1}{2}\rangle$	$ +2-\frac{3}{2}\rangle$	$ -2+\frac{3}{2}\rangle$	$ -2+\frac{1}{2}\rangle$	$ -2-\frac{1}{2}\rangle$	$ -2-\frac{3}{2}\rangle$
$B = 0$ T								
$ \psi_{\alpha 0}\rangle$	0	0.46	0	-0.86	0	0	0	0
$ \psi_{\alpha 1}\rangle$	0	0	0	0	-0.86	0	0.46	0
$ \psi_{\beta 0}\rangle$	0.82	0	-0.53	0	0	0	0	0
$ \psi_{\beta 1}\rangle$	0	0	0	0	0	-0.53	0	0.82
$B = 4$ T								
$ \psi_{\alpha 0}\rangle$	0	-0.53	0	0.84	0	0	0	0
$ \psi_{\alpha 1}\rangle$	0	0	0	0	-0.90	0	0.40	0
$ \psi_{\beta 0}\rangle$	0.88	0	-0.46	0	0	0	0	0
$ \psi_{\beta 1}\rangle$	0	0	0	0	0	-0.61	0	0.78

Tip-Position Dependent Transition Intensities

We will now expand our analysis to include higher-energy excitations as well as excitations of the Fe spin. In order to accurately sort out which of the large set of eigenstates are accessible through inelastic electron excitations we will use the transition intensity calculations that were introduced in section 3.3.3. We simulate the position of the tip by assuming that only the spin closest to the tip can be excited, e.g.⁶:

$$I_{0 \rightarrow n}^{(\text{Fe})} = \left| \langle \psi_n | \hat{S}_x^{(\text{Fe})} | \psi_0 \rangle \right|^2 + \left| \langle \psi_n | \hat{S}_y^{(\text{Fe})} | \psi_0 \rangle \right|^2 + \left| \langle \psi_n | \hat{S}_z^{(\text{Fe})} | \psi_0 \rangle \right|^2, \quad (4.21)$$

where $I_{0 \rightarrow n}^{(\text{Fe})}$ is the transition intensity from the ground state to $|\psi_n\rangle$ when the tip is over the Fe atom. As the multitude of states is much larger than before it is worthwhile to combine the intensity information together with the energy levels in one single graph which will now be introduced step by step.

The small dots in figs. 4.10 and 4.11 show the lowest 12 eigenenergies of (4.20) in magnetic field intervals of 0.1 T along x and y respectively. As before, proper parameter values for these calculations were found by manual tuning. The dots representing the ground state $|\psi_0\rangle$ are colored black while the coloring of the remaining levels $|\psi_n\rangle$ is based on $I_{0 \rightarrow n}^{(\text{Co})}$ and $I_{0 \rightarrow n}^{(\text{Fe})}$ (see color key in fig. 4.11). Red

⁶Note that here we drop the suggestive labelling used in the previous section and once more number the states $|\psi_n\rangle$ with increasing energy.

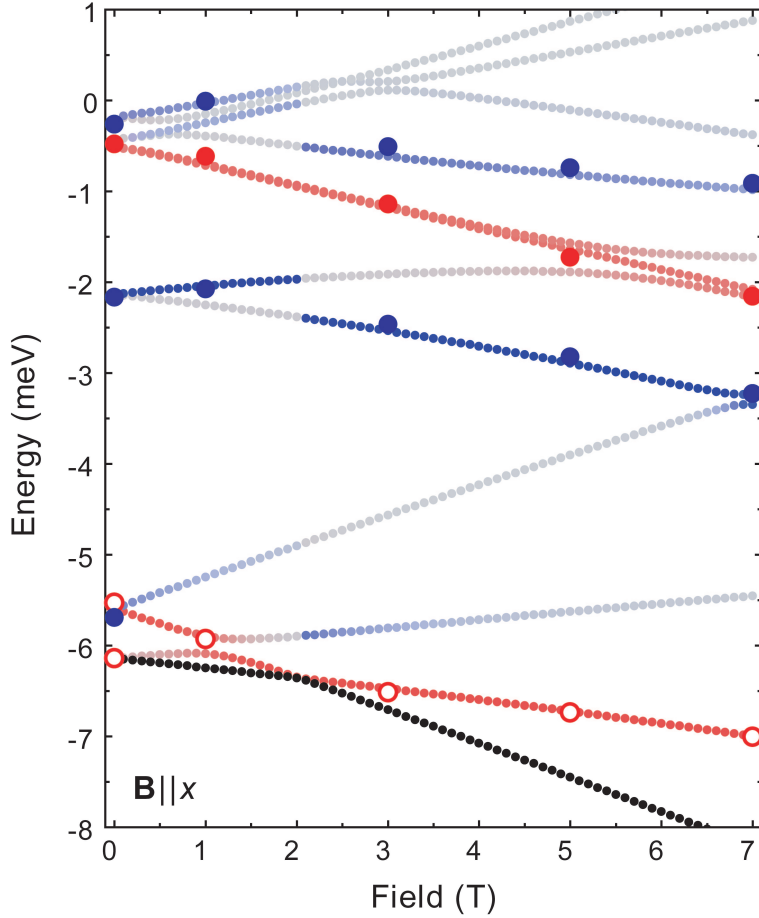


Figure 4.10: Small dots: lowest 12 eigenvalues of (4.20) with $J = 0.13$ meV, $g_{\text{Fe}} = 2.11$, $g_{\text{Co}} = 2.16$, $D_{\text{Fe}} = -1.53$ meV, $E_{\text{Fe}} = 0.31$ meV and $D_{\text{Co}} = 2.70$ meV for $B = 0$ to 7 T in increments of 0.1 T along x . Color indicates the values of $I_{0 \rightarrow n}^{(\text{Co})}$ (red) and $I_{0 \rightarrow n}^{(\text{Fe})}$ (blue); see fig. 4.11 for key. The ground state is colored black. Large dots: experimental data points indicating positions of peaks (open circles) and steps (filled circles) in figs. 4.7a (blue, Fe) and b (red, Co), all plotted with respect to the calculated ground state.

dots correspond to a high value of $I_{0 \rightarrow n}^{(\text{Co})}$ (i.e. a high transition intensity towards that level if the tip is positioned over Co) while blue dots have a high $I_{0 \rightarrow n}^{(\text{Fe})}$. If neither intensity is high the dot becomes grey: it represents a state that is not expected to be accessible through tunneling excitation through either atom. States that can be reached both via excitations on Co and on Fe are colored magenta. In both graphs the blue excitations between -3 and 0 meV represent excitations towards $|m_{\text{Fe}}| = 1$; the red line between -2 and 0 meV consists of

two excitations that involve rotating the Co spin towards its hard-axis⁷. Note that here we use our knowledge of the intensities only qualitatively: a transition is either possible or not.

Experimental data, taken from fig. 4.7, is added to the graph as larger dots: red for features found in Co spectra and blue for Fe. Open circles correspond to peak positions (local maximum in dI/dV) while closed circles refer to steps (maximum in $|d^2I/dV^2|$). The agreement is evident: data points appear almost exclusively on energy levels that have the appropriate color. In a few instances (such as the low-energy Fe step at $B = 1$ T along y) the dot ends up between two correctly colored lines (in this case magenta). In those situations the energy resolution of the measurement was insufficient to separately distinguish two individual excitations. The highest-energy Fe excitations for $\mathbf{B} \parallel y$ that lie close to lines that are only faintly blue correspond to steps that only have a relatively small height as seen in fig. 4.7c.

The point where the ground state changes, $B = 2.1$ T along x , has a very clear signature in the higher-energy excitations too: both Fe transitions suddenly switch to a different level. Let us focus on the lower of the two (around -2 meV) by expressing the involved levels at the critical field within the subspace of $|m_{\text{Fe}}| = 1$ states (in the $|m_{\text{Fe}} m_{\text{Co}}\rangle$ -basis, with ground state $|\psi_0\rangle$):

$$\begin{aligned} |\psi_4\rangle &= -0.65|+1+\frac{3}{2}\rangle - 0.30|+1-\frac{1}{2}\rangle + 0.59|-1+\frac{3}{2}\rangle + 0.35|-1-\frac{1}{2}\rangle, \quad \text{and} \\ |\psi_5\rangle &= -0.70|+1-\frac{3}{2}\rangle + 0.43|+1+\frac{1}{2}\rangle + 0.46|-1-\frac{3}{2}\rangle - 0.30|-1+\frac{1}{2}\rangle, \end{aligned}$$

where matrix elements ≤ 0.10 are ignored. Again, these two states almost only differ in the sign of m_{Co} . Comparing their coefficients to the ones listed in table 4.1, we see that through $\Delta|m_{\text{Fe}}| = 1$ transitions $|\psi_4\rangle$ is linked to $|\psi_{\beta 0}\rangle$ (ground state above 2.1 T) while $|\psi_5\rangle$ is linked to $|\psi_{\alpha 0}\rangle$ (ground state below 2.1 T). The external magnetic field flipping the nearby Co spin is felt on the Fe atom which is reflected beautifully in the corresponding spin excitations.

Let us do the same thing for $\text{Mn}_{\text{vV}}\text{Co}$. For this system the full Heisenberg Hamiltonian becomes:

$$\begin{aligned} \hat{\mathcal{H}} &= J\hat{\mathbf{S}}^{(\text{Mn})} \cdot \hat{\mathbf{S}}^{(\text{Co})} - \mu_B \mathbf{B} \cdot \left(g_{\text{Mn}} \hat{\mathbf{S}}^{(\text{Mn})} + g_{\text{Co}} \hat{\mathbf{S}}^{(\text{Co})} \right) \\ &\quad + D_{\text{Mn}} \hat{S}_z^{2(\text{Mn})} + D_{\text{Co}} \hat{S}_y^{2(\text{Co})}, \end{aligned} \quad (4.22)$$

where we neglect E_{Mn} which in the case of a single Mn atom was only 0.007 meV. This system has 24 eigenstates which are all plotted for $J = 0.06$ meV with the two in-plane field directions up to 7 T in figs. 4.12 and 4.13. In either case the states appear in two bundles of 12 that are separated by $2D_{\text{Co}}$. The color coding for the intensities is similar as before except that blue now refers to $I_{0 \rightarrow n}^{(\text{Mn})}$. On the Co atom excitations can be made towards the high bundle, which as before involves rotating the spin towards its hard-axis, whereas Kondo resonances only

⁷As the vertical scales of these graphs have an arbitrary zero, these specific energy values have no physical significance and are only mentioned for visual reference.

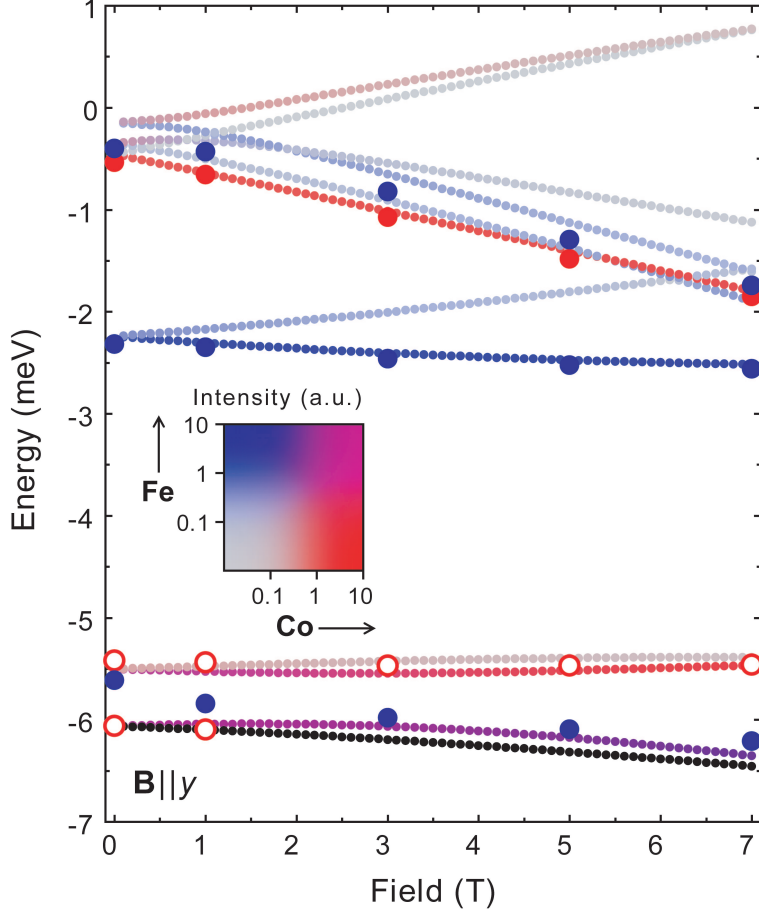


Figure 4.11: Lowest 12 eigenvalues of (4.20) with $J = 0.13$ meV, $g_{\text{Fe}} = 2.11$, $g_{\text{Co}} = 2.16$, $D_{\text{Fe}} = -1.48$ meV, $E_{\text{Fe}} = 0.33$ meV and $D_{\text{Co}} = 2.70$ meV for $\mathbf{B} \parallel y$, represented as in fig. 4.10. Experimental data points extracted from figs. 4.7c (blue) and d (red). **Inset:** key for the color representation of $I_{0 \rightarrow n}^{(\text{Co})}$ and $I_{0 \rightarrow n}^{(\text{Fe})}$.

occur within the lower bundle. The Mn spin can excite towards the $m_{\text{Mn}} = \frac{3}{2}$ states in the lower bundle where m_{Mn} refers to the eigenvalue of $\hat{S}_z^{(\text{Mn})}$. Each of these predicted transitions is observed exactly at the correct energy.

Although by far not as clear as with $\text{Fe}_{\text{VV}}\text{Co}$ also here a cancellation effect, giving rise to the reconstructed Kondo peak, can be discerned. When $B \simeq 1$ T along y , the red/magenta line that carries the low-energy Co excitation comes very close to the ground state – much closer than it does for $\mathbf{B} \parallel x$. It is this intersection of ground states that tells us the correct value of the Heisenberg constant: $J = 0.03 \pm 0.02$ meV for $\text{Mn}_{\text{VV}}\text{Co}$ and $J = 0.13 \pm 0.02$ meV for

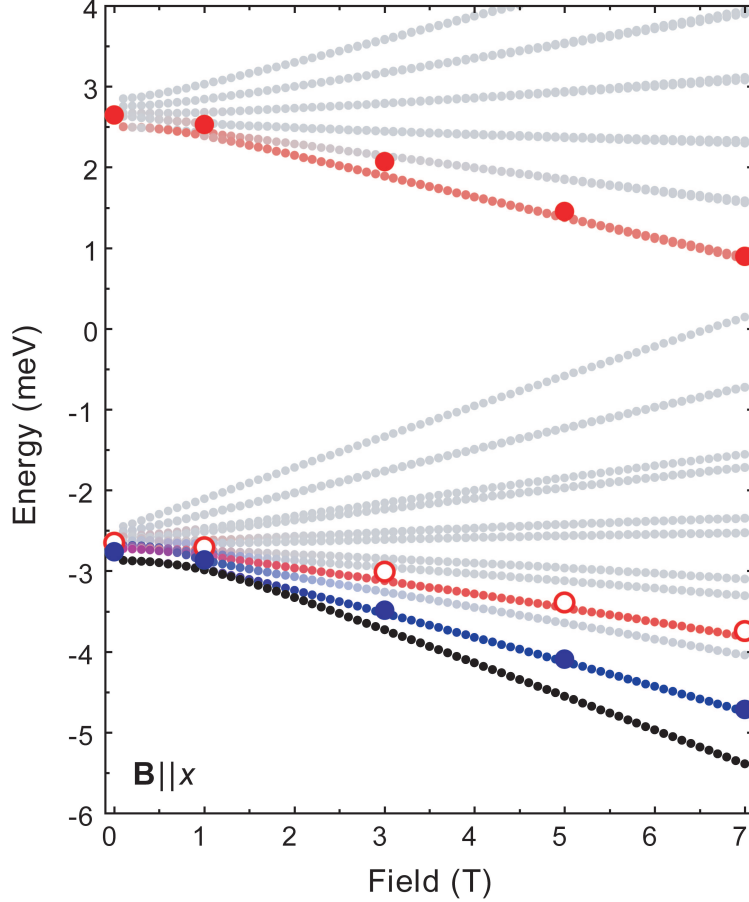


Figure 4.12: Eigenvalues of (4.22) with $J = 0.03$ meV, $g_{\text{Mn}} = 1.90$, $g_{\text{Co}} = 2.16$, $D_{\text{Mn}} = -0.04$ meV and $D_{\text{Co}} = 2.65$ meV for $\mathbf{B} \parallel x$. See fig. 4.13 for key of color representation of $I_{0 \rightarrow n}^{(\text{Co})}$ and $I_{0 \rightarrow n}^{(\text{Mn})}$. Experimental data points extracted from figs. 4.8a (blue) and b (red), plotted with respect to the calculated ground state. Open (*filled*) circles represent peak (*step*) positions.

$\text{Fe}_{\text{vV}}\text{Co}$. But what about the effective field that was introduced in section 4.3.2? Well, it really is the same thing. If we reduce either (4.20) or (4.22) to a single Co spin Hamiltonian by fixing the other spin (i.e. by throwing away all terms that contain no operators working on the Co spin) we find:

$$\hat{\mathcal{H}} = -g_{\text{Co}}\mu_B \left(\mathbf{B} - \frac{J\mathbf{S}^{(\text{X})}}{g_{\text{Co}}\mu_B} \right) \cdot \hat{\mathbf{S}}^{(\text{Co})} + D_{\text{Co}}\hat{S}_y^{2(\text{Co})}, \quad (4.23)$$

where (X) is either (Fe) or (Mn). Here $\mathbf{S}^{(\text{X})}$ no longer needs to be an operator as it does not work on the Co spin anyhow. The proximity of the second spin is

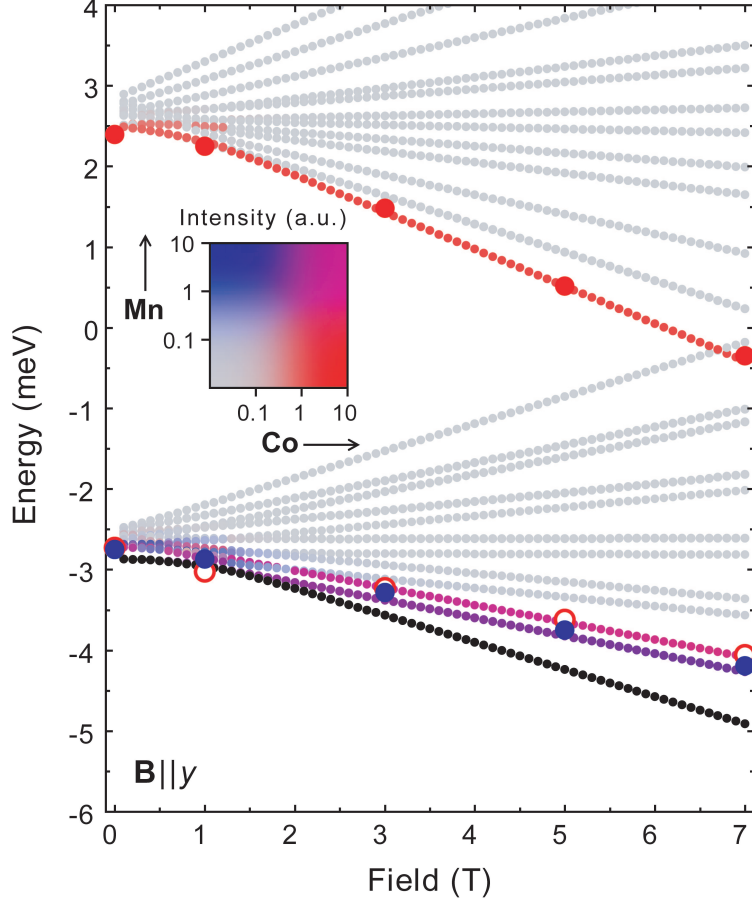


Figure 4.13: Eigenvalues of (4.22) with $J = 0.03$ meV, $g_{\text{Mn}} = 1.90$, $g_{\text{Co}} = 2.16$, $D_{\text{Mn}} = -0.04$ meV and $D_{\text{Co}} = 2.65$ meV for $\mathbf{B} \parallel y$. Experimental data points extracted from figs. 4.8c (blue) and d (red). **Inset:** key for the color representation of $I_{0 \rightarrow n}^{(\text{Co})}$ and $I_{0 \rightarrow n}^{(\text{Mn})}$.

thus represented by an effective field $\mathbf{B}_{\text{eff}} = -J\mathbf{S}^{(X)}/g_{\text{Co}}\mu_B$, corresponding to a magnitude of 2.1 T for Fe and 0.6 T for Mn.

The Heisenberg Kondo Dimer

The notion of coupling multiple Kondo systems has been considered by many theorists in a model that is known as the *Kondo Lattice* [83]. Especially interesting is the case where the coupling strength between spins can be tuned [84], which was realized experimentally in a quantum dot dimer [62]. Although tunable coupling is not readily available in our $\text{Co}_{\text{Vv}}\text{Co}$ structures, their properties

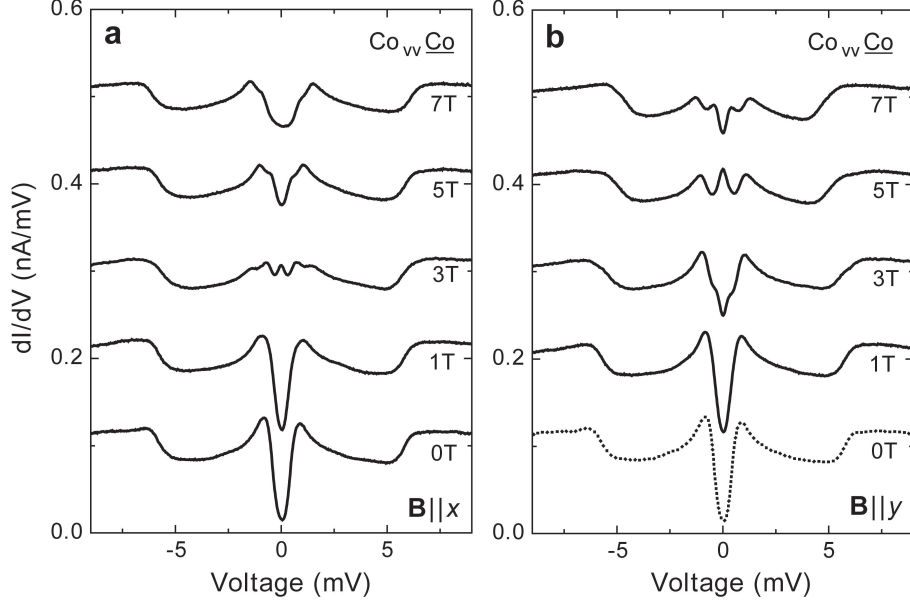


Figure 4.14: dI/dV -spectra measured on one of the Co atoms in $\text{Co}_{\text{vv}}\text{Co}$ at various magnetic fields oriented along x (**a**) and y (**b**). The dotted spectrum in (b) was taken on a different structure than the others in the same panel. Since the field direction is irrelevant at zero field, this particular curve was measured over the atom neighboring the one in panel (a).

might provide valuable insights in the context of Kondo Lattices. Figure 4.14 shows field-dependent measurements performed on one of the two Co atoms in either $\text{Co}_{\text{vv}}\text{Co}$ dimer of fig. 4.6b, i.e. for $\mathbf{B} \parallel x$ and y . The spectra taken at 0 T are characterized by a remarkably deep dip at zero bias that is somewhat reminiscent of a band gap. At higher field strengths multiple small peaks seem to cross each other at various energies. We will attempt to model this with yet another variation of the full Heisenberg Hamiltonian:

$$\begin{aligned} \hat{\mathcal{H}} = & J\hat{\mathbf{S}}^{(\text{Co1})} \cdot \hat{\mathbf{S}}^{(\text{Co2})} - g_{\text{Co}}\mu_B\mathbf{B} \cdot (\hat{\mathbf{S}}^{(\text{Co1})} + \hat{\mathbf{S}}^{(\text{Co2})}) \\ & + D_{\text{Co}} \left(\hat{S}_y^{2(\text{Co1})} + \hat{S}_y^{2(\text{Co2})} \right), \end{aligned} \quad (4.24)$$

where the superscript (Co1) or (Co2) indicates which of the two Co spins an operator works on. Surprisingly, as shown in figs. 4.15 and 4.16, this simple two-spin Hamiltonian can once again assign each observed spin excitation or resonance to an allowed transition within its eigensystem. Here the lower four states are all linear combinations of $|m_{\text{Co1}} m_{\text{Co2}}\rangle = |\pm \frac{1}{2} \pm \frac{1}{2}\rangle$ (where m_{Co1} and m_{Co2} refer to the eigenvalues of $\hat{S}_y^{(\text{Co1})}$ and $\hat{S}_y^{(\text{Co2})}$ respectively), whereas during the higher-energy excitations one of the two Co spins is rotated towards its hard-axis. In this situation a best fit is found for $J = 0.25 \pm 0.04$ meV.

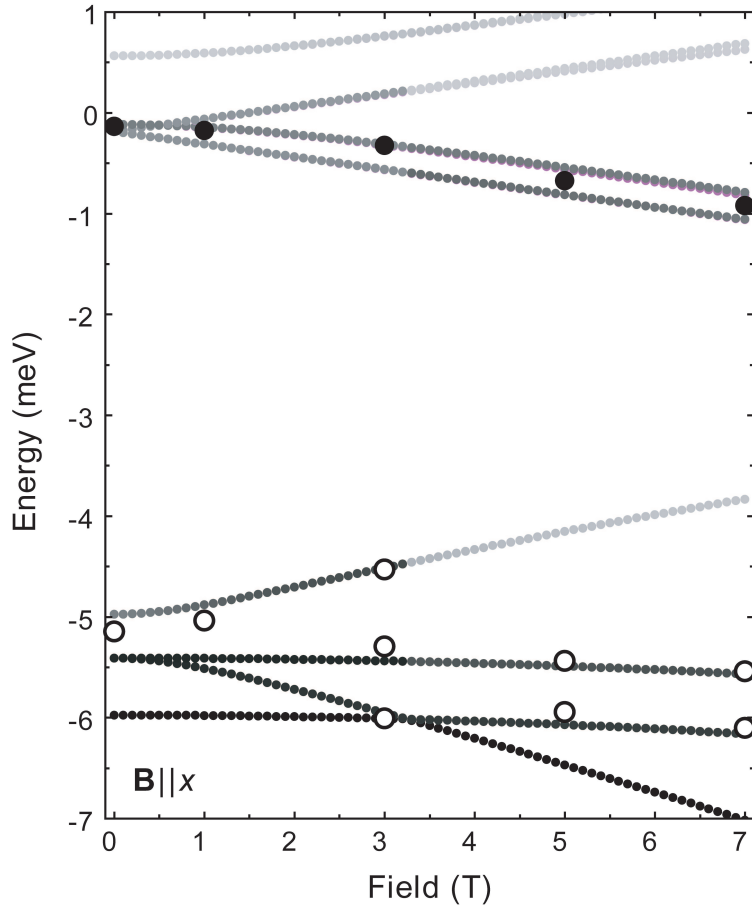


Figure 4.15: Lowest 12 eigenvalues of (4.24) with $J = 0.25$ meV, $g_{\text{Co}} = 2.16$ and $D_{\text{Co}} = 2.70$ meV for $\mathbf{B} \parallel x$. For each level $|\psi_n\rangle$ the corresponding transition intensity $I_{0 \rightarrow n}^{(\text{Co})}$ is shown in greyscale (see fig. 4.16 for key). Experimental data points extracted from fig. 4.14a plotted with respect to the calculated ground state where open (*filled*) circles represent peak (*step*) positions.

A remarkable exception to the overall good agreement between the measurements and the model occurs among the high-energy excitations for $B < 4.5$ T along y (fig. 4.16). According to the intensity calculations an additional excitation should take place between 6.0 and 6.5 meV. It is unclear why this is not observed through spectroscopy.

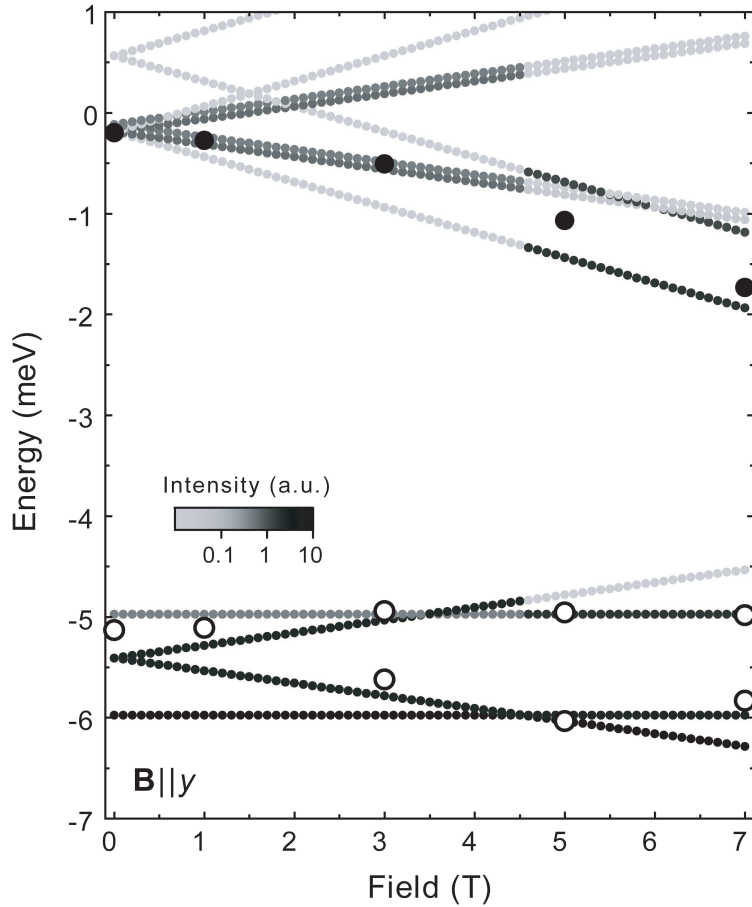


Figure 4.16: Lowest 12 eigenvalues of (4.24) with $J = 0.25$ meV, $g_{\text{Co}} = 2.16$ and $D_{\text{Co}} = 2.70$ meV for $\mathbf{B} \parallel y$. Experimental data points extracted from fig. 4.14b. **Inset:** key for the greyscale representation of $I_{0 \rightarrow n}^{(\text{Co})}$.

4.4 Discussion

The Kondo effect results from a resonant interaction between a spin and its surrounding conduction electrons. It is a complex many-body phenomenon that even after decades of research remains topic of debate. The work presented in this chapter might be a valuable contribution to this discussion. We have studied a single magnetic atom with a known high spin in an anisotropic environment that was thoroughly analyzed beforehand. We understand exactly how the crystal field anisotropy effectively reduces the spin to an $S = \frac{1}{2}$ Kramers doublet thus creating a Kondo system, and why other magnetic atoms in the same situation do not show such behavior. If a magnetic field is applied the Kondo resonance

splits in a manner that precisely reflects the magnetically anisotropic nature of the system consisting of the spin and its environment. And finally, if a second magnetic atom is positioned in the vicinity of the Kondo spin the resulting changes in the energies at which the resonances take place can be fully modelled by isotropic Heisenberg coupling of two anisotropic spins. Surprisingly, this is true even if the second spin is a Kondo spin itself.

The various $X_{VV}Co$ structures form a unique class of nano-objects. The energy scales involved in the coupling process (i.e. J) are of the same magnitude as all the other relevant processes in the system (D , E , $\mu_B B$), yet the spins are coupled weakly enough and are sufficiently far apart such that each can be addressed separately by the STM tip. As we have concluded from DFT studies in the previous chapter, the adatoms are incorporated into a large molecular network. Hence the dimers discussed here can be regarded as molecular magnets where each of the magnetic centers can be studied on its own.

While we can successfully model the interaction with an empirical Heisenberg constant J , the physics of the coupling remains unclear. According to classical electrodynamics the dipole $\boldsymbol{\mu} = -e\mathbf{S}/m_e$ formed by an electron spin \mathbf{S} (where m_e is the electron mass) sets up a magnetic field

$$\mathbf{B} = \frac{\mu_0}{4\pi r^3} \left(3(\boldsymbol{\mu} \cdot \hat{r})\hat{r} - \boldsymbol{\mu} \right) \quad (4.25)$$

at a position \mathbf{r} relative to the spin (if $r > 0$). Here μ_0 is the permeability of vacuum and $\hat{r} = \mathbf{r}/r$. In case of $S = 2$ and $r = 7.2 \text{ \AA}$ the magnitude of such a field cannot exceed $4 \times 10^{-2} \text{ T}$ which is 50 times lower than the 2.1 T we encounter. This rules out dipolar interaction as the dominant mediator for our J , which means that the spins have to be coupled somehow by exchange interaction through the Cu_2N surface. In the following chapter we will discuss some initial investigations into the mechanism of spin coupling on Cu_2N .

Chapter 5

Initial Results on Further Experiments

As we have seen in the previous chapters, the Cu_2N surface provides an excellent environment for doing experiments aimed at characterizing the interplay of atomic spins with their direct environment. Clearly we have only just begun exploring its full potential and further progress is currently being made rapidly. In the final chapter of this thesis some initial results of a few promising experiments will be presented.

5.1 Distance Dependence of Spin Interaction

We concluded chapter 4 with the observation that, although we can very well describe the coupling between the spins in the $X_{\text{vv}}\text{Co}$ structures of section 4.3.2 with an empirical Heisenberg parameter J , we still have no idea of the actual nature of the coupling (other than that it is not just dipolar interaction and therefore must be somehow mediated by the surface). As a first attempt towards identifying the physics behind this interaction, it is useful to investigate the variation of the coupling strength as a function of the distance between the spins. For example in the case of RKKY interaction [85], where the exchange coupling is carried by the conduction electrons in a Fermi sea (such as the bulk copper below the Cu_2N), its strength is expected to show a damped oscillation:

$$J_{\text{RKKY}}(\mathbf{r}) \propto \frac{r \cos(k_F r) - \sin(k_F r)}{r^4}, \quad (5.1)$$

where \mathbf{r} is the vector separating the spins and k_F is the length of the Fermi wave vector in the direction of \mathbf{r} .

The possibilities for varying the separation on Cu_2N are quite limited. Repeated attempts to build dimers where the atoms are separated by only one vacancy site (3.6 Å distance) were all unsuccessful, probably due to instability of the structure, while a separation of three vacancies or more yields no observable

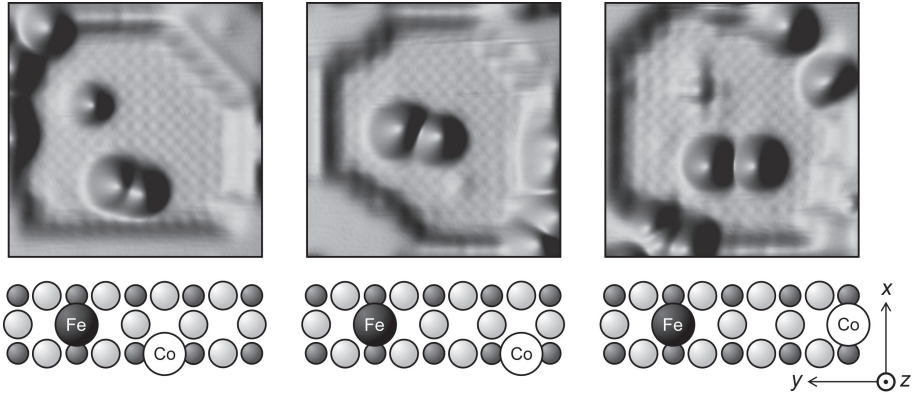


Figure 5.1: **Top row:** Topographic images (6×6 nm, 10 mV/1 nA) showing three Fe/Co dimers with different relative positions of the atoms; from left to right $\text{Fe}_{v\setminus}\text{Co}$, $\text{Fe}_{v\setminus\setminus}\text{Co}$ and $\text{Fe}_{v\setminus\setminus\setminus}\text{Co}$. In each case the left atom is Fe, located on a horizontal v-row. In the left image the distance from the Co atom to the missing N-row that forms the edge of the island is 10.8 \AA (i.e. 3 unit cells). **Bottom row:** Corresponding drawings of the structure of the dimers where, as before, light circles indicate Cu atoms and small dark circles are N atoms. The assignment of the axes applies to all three structures.

coupling. In order to somewhat appropriately characterize the distance dependence of the interaction, dimers with orientations other than exactly along a v-row have to be included. Fig. 5.1 shows three variations on the $\text{Fe}_{v\setminus}\text{Co}$ structure¹, two of which have its Co atom lying off the v-row. Using the \setminus symbol to indicate a single diagonal step, we will refer to these objects as “ $\text{Fe}_{v\setminus}\text{Co}$ ” and “ $\text{Fe}_{v\setminus\setminus}\text{Co}$ ”, with direct separation distances of 5.7 and 9.2 \AA respectively. In the third, “ $\text{Fe}_{v\setminus\setminus\setminus}\text{Co}$ ”, the atoms are spaced by 10.8 \AA along the v-row.

On each of these structures dI/dV -spectra have been measured over the Co atom at various fields oriented in the x -direction. These should be compared to fig. 4.7b, showing equivalent measurements performed on $\text{Fe}_{v\setminus}\text{Co}$: here we saw that the external field cancels the influence of the Fe spin around $B = 2$ T. Results for $\text{Fe}_{v\setminus}\text{Co}$ are shown in fig. 5.2a. Again the proximity of the Fe atom causes a splitting of the Kondo peak at zero field, but this time the ‘effective field’ is much stronger: the peaks seem to converge around 9 T. Also the spectra feature two steps at higher energy rather than only one. In the case of $\text{Fe}_{v\setminus\setminus}\text{Co}$ (fig. 5.2b) the effect of the coupling is much weaker such that no splitting can be observed at zero field.

When trying to model these two ‘semi-diagonal’ systems as we did in chapter 4 for $\text{Fe}_{v\setminus}\text{Co}$, we should bear in mind that not only the relative positions, but also the relative orientations of the two spins have changed. Previously the Co spin (having its primary anisotropy axis \mathcal{Z} oriented locally along the v-row) had its hard-axis perpendicular to the Fe spin’s easy-axis (oriented along the N-

¹This combination is most suitable: $\text{Mn}_{v\setminus}\text{Co}$ has a much smaller J and the spectra of $\text{Co}_{v\setminus}\text{Co}$ are somewhat confusing due to its many low-energy excitations.

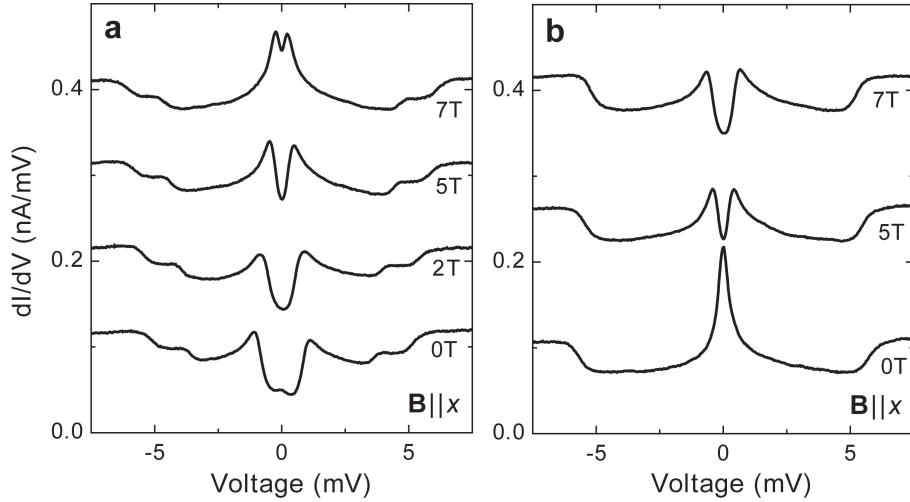


Figure 5.2: dI/dV -spectra measured over the Co atoms of $\text{Fe}_v\backslash\text{Co}$ (a) and $\text{Fe}_{vv}\backslash\text{Co}$ (b) at various fields with $\mathbf{B} \parallel x$. Curves obtained at non-zero fields are offset with 0.10 nA/mV in (a) and 0.15 nA/mV in (b).

row). However, in the current situations the local environment of the Co atom has rotated by 90° with respect to the Fe atom: both spins now have their primary anisotropy axis pointing in the x -direction. The proper Heisenberg model Hamiltonian thus becomes:

$$\begin{aligned} \hat{\mathcal{H}} = & J\hat{\mathbf{S}}^{(\text{Fe})} \cdot \hat{\mathbf{S}}^{(\text{Co})} - \mu_B \mathbf{B} \cdot \left(g_{\text{Fe}} \hat{\mathbf{S}}^{(\text{Fe})} + g_{\text{Co}} \hat{\mathbf{S}}^{(\text{Co})} \right) \\ & + D_{\text{Fe}} \hat{S}_x^{2(\text{Fe})} + E_{\text{Fe}} \left(\hat{S}_y^{2(\text{Fe})} - \hat{S}_z^{2(\text{Fe})} \right) + D_{\text{Co}} \hat{S}_x^{2(\text{Co})}, \end{aligned} \quad (5.2)$$

which differs from (4.20) only in the subscript of the very last term. Starting with $\text{Fe}_v\backslash\text{Co}$, we see in fig. 5.3 that with a J -value of 0.48 ± 0.02 meV, (5.2) very well reproduces the measured peak positions, as well as both of the steps. So by reducing the spacing between the atoms by merely 20%, their interaction has become almost four times stronger (Fe_{vv}Co has $J = 0.13$ meV). The appearance of the extra step around 4 mV is a direct consequence of this. If we express the two excited states corresponding to either step, $|\psi_5\rangle$ and $|\psi_7\rangle$, in the basis of $\hat{S}_x^{(\text{Fe})}$ and $\hat{S}_x^{(\text{Co})}$ eigenstates $|m_{\text{Fe}} m_{\text{Co}}\rangle$ at $B = 0$, we find:

$$\begin{aligned} |\psi_5\rangle &= -0.60|+2-\frac{3}{2}\rangle - 0.30|-1-\frac{1}{2}\rangle + 0.68|+1-\frac{1}{2}\rangle, \quad \text{and} \\ |\psi_7\rangle &= -0.77|+2-\frac{3}{2}\rangle + 0.44|-1-\frac{1}{2}\rangle - 0.39|+1-\frac{1}{2}\rangle, \end{aligned}$$

where other contributions up to 0.21 were neglected. Interestingly, the excitation to $|+2-\frac{3}{2}\rangle$ (from ground state $|+2-\frac{1}{2}\rangle$), which is expected to occur when the tip is placed over the Co atom, has strongly mixed with two excitations

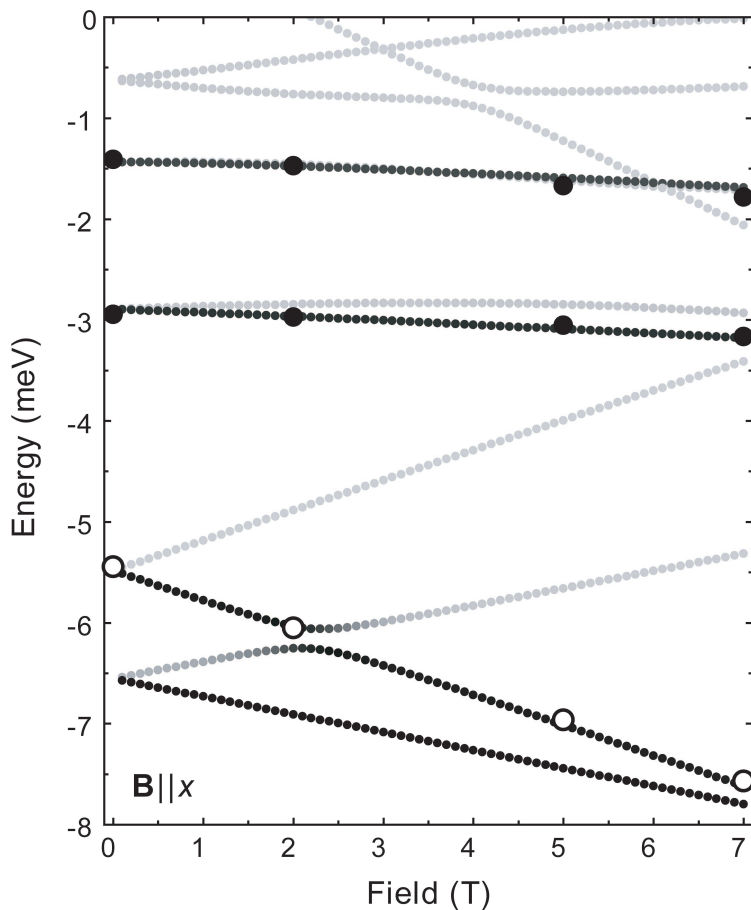


Figure 5.3: Lowest 11 eigenvalues of (5.2) with $J = 0.48$ meV, $g_{\text{Fe}} = 2.11$, $g_{\text{Co}} = 2.16$, $D_{\text{Fe}} = -1.55$ meV, $E_{\text{Fe}} = 0.31$ meV and $D_{\text{Co}} = 2.70$ meV for $\mathbf{B} \parallel x$. For each level $|\psi_n\rangle$ the corresponding transition intensity $I_{0 \rightarrow n}^{(\text{Co})}$, i.e. with the tip placed over the Co atom, is shown in greyscale (see fig. 5.4 for key and section 4.3.3 for an introduction into the representation used in this graph). Experimental data points extracted from fig. 5.2a.

of the Fe spin² and is now distributed over two transitions. This is an important result: apparently the two spins are now so strongly coupled that we can no longer make excitations on only one of them without influencing the other. Gradually the structure is becoming a single spectroscopic entity.

The longer semi-diagonal structure $\text{Fe}_{v,v} \setminus \text{Co}$ is more difficult to analyze properly, as we have only few data points on it and the energy resolution is insufficient to make out any zero-field splitting. However, due to the cal-

²Actually with only one Fe excitation: $|+1-\frac{1}{2}\rangle$. This one has in turn mixed with $|-1-\frac{1}{2}\rangle$ because of the finite value of E_{Fe} .

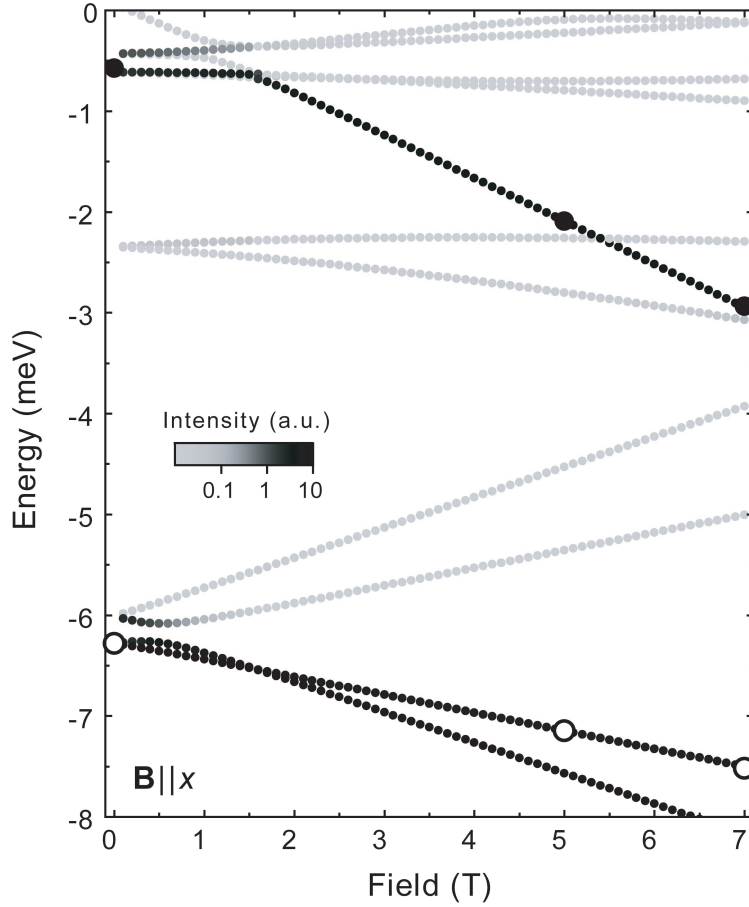


Figure 5.4: Lowest 11 eigenvalues of (5.2) with $J = 0.10$ meV, $g_{\text{Fe}} = 2.11$, $g_{\text{Co}} = 2.16$, $D_{\text{Fe}} = -1.55$ meV, $E_{\text{Fe}} = 0.31$ meV and $D_{\text{Co}} = 2.70$ meV for $\mathbf{B} \parallel x$. Experimental data extracted from fig. 5.2b. **Inset:** key for the greyscale representation of $I_{0 \rightarrow n}^{(\text{Co})}$.

culated higher-energy excitations evolving in a distinct nonlinear fashion we can extract a fitting value of J , albeit with a somewhat larger error margin: $J = 0.10 \pm 0.05$ meV. Figure 5.4 shows the corresponding energy level diagram.

Finally there is the 10.8 Å long $\text{Fe}_{\text{VVV}}\text{Co}$ structure. Spectra measured on its Co atom with $\mathbf{B} \parallel x$ (not shown here) look very similar to the results obtained on a free Co atom (i.e. fig. 4.4c). The only notable discrepancy – a slight downshift in energy for all excitations – indicates a marginally positive J , but might as well result from the usual 5% variations in the anisotropy parameters. It is best described with $J = 0.02 \pm 0.02$ meV.

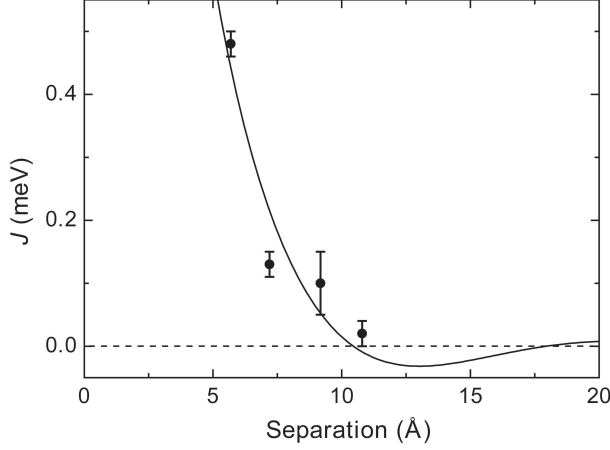


Figure 5.5: Plot of the experimentally determined values for J as a function of the direct separation distance between the atoms in various Fe/Co dimers on Cu_2N . The solid line shows a fit using (5.1) with $k_F = 0.43 \pm 0.06 \text{ \AA}^{-1}$.

We have now collected four data points characterizing the distance dependence of J , which are plotted in fig. 5.5. The measurements systematically indicate a very steep decline of the coupling strength. Several remarks should be made with respect to this graph. First, for the semi-diagonal structures we used the direct distance between the atoms, ignoring any possible anisotropies in the spin-interaction and in k_F arising from the Cu_2N lattice. In this context it is important to note that these structures are *not* invariant under switching the positions of the Fe and Co atoms, and were chosen arbitrarily. The inverted structures (e.g. $\text{Co}_v \setminus \text{Fe}$ instead of $\text{Fe}_v \setminus \text{Co}$) have not been investigated, but might give a different J at the same separation distance. Second, the available data points are still too few and too close to each other to make any claim concerning the nature of the coupling. The solid curve in fig. 5.5 only gives a best fit of J_{RKKY} , assuming that (5.1) is valid.

Having said that, the RKKY interaction proposed by the fit is certainly not unrealistic. It would explain the sharp increase of J below 7 \AA and the resulting value for the Fermi wave vector, $k_F = 0.43 \text{ \AA}^{-1}$, is reasonable. For comparison: in bulk copper (having the same lattice constant of 3.6 \AA) k_F varies along the Fermi surface from 1.36 to 1.51 \AA^{-1} . The reduction by a factor of ~ 3 may be caused by local deformations of the Fermi surface due to the loss of symmetry in Cu_2N , especially if that results in the creation of pockets of states at the Brillouin-zone boundary having lower effective wave vectors. Overall it is not unthinkable that with a few extra measurements in the range $r = 11 - 15 \text{ \AA}$ (e.g. $\text{Fe}_{vvv} \setminus \text{Co}$), where J is expected to become negative, the suggestion of RKKY interaction as presented can eventually be confirmed.

5.2 Coupling Along the N-Row

A different way of modifying the interaction between the atoms is to couple them along the N-direction rather than the v-direction. In contrast to previous work [19], where atoms were placed along an N-row at intervals of a single lattice spacing (3.6 Å), in this section we will focus on structures with 7.2 Å separation.

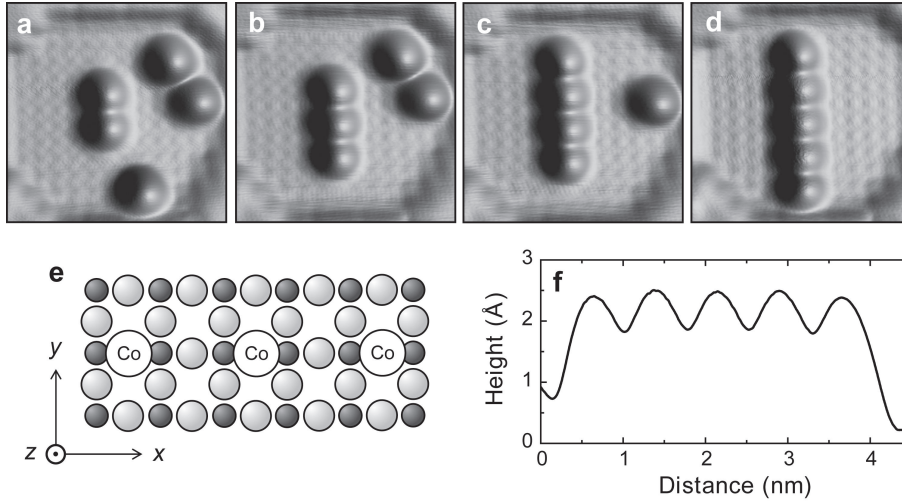


Figure 5.6: (a–d) Topographic images (5×5 nm, 10 mV/1 nA) of $\text{Co}_{(\text{NNCo})_{n-1}}$ for $n = 2, 3, 4$ and 5 respectively. Comparable structures made of Fe have similar topographic appearances. (e) Structural drawing of $\text{Co}_{(\text{NNCo})_2}$ with axis assignments. (f) Height profile extracted from (d) taken along the ridge of the structure (upward).

Figures 5.6a–d show topographic images recorded during the construction of a 28.8 Å long Co pentamer. To add a Co atom to the chain, it is first placed at the N site that is 9.0 Å away from the last atom of the chain, after which it is hopped in place (section 2.3.3). Although the atom can in principle hop two ways, the ‘success rate’ of the hopping procedure seems to increase with the length of the chain. As with the structures built along the v-rows at equal distance, atoms can be removed from the chain (both from the ends and from the center) without inflicting damage. We will refer to the subsequent structures shown in the figure as “ $\text{Co}_{(\text{NNCo})_{n-1}}$ ” with n , the number of atoms in the chain, ranging from 2 to 5. Comparable structures were made with Fe instead of Co, having a very similar topographic appearance as their Co counterparts. In the following we will discuss spectroscopic results obtained on either class of structures, starting with $\text{Fe}_{(\text{NNFe})_{n-1}}$.

5.2.1 The Ising Chain: Ferromagnetic Coupling?

Conductance spectra measured on all atoms of each of the four $\text{Fe}_{(\text{NNFe})_{n-1}}$ structures with $n \leq 5$ are shown in fig. 5.7, all at $B = 0$. The excitations in these cases appear at considerably higher energies than before (as a result of stronger coupling), such that the influence of a magnetic field would be much less prominent and will therefore not be considered here. What strikes immediately is that, except for a few details, there are only two kinds of spectra. Those measured over atoms located at either end of a structure (‘outer’ atoms) feature a single³ step around 7 mV, while the remaining spectra (taken over ‘inner’ atoms) have a step around 10 mV. It seems as if the excitation energies on each atom are determined only by the number of nearest neighbors: one or two respectively. The results can be modelled surprisingly well using a Hamiltonian based on Ising interaction combined with uniaxial anisotropy:

$$\hat{\mathcal{H}} = \sum_{i=1}^{n-1} J \hat{S}_x^{(i)} \hat{S}_x^{(i+1)} + \sum_{i=1}^n D \hat{S}_x^{2(i)}, \quad (5.3)$$

where J is the Ising interaction parameter and the operator $\hat{S}_x^{(i)}$ quantifies the x -component of the magnetization of the i -th spin in the chain. As before, D is the anisotropy parameter along x , the primary anisotropy axis for Fe.

Conveniently, this Hamiltonian is diagonal in the basis of all $\hat{S}_x^{(i)}$ eigenstates, expressed by the quantum numbers m_i , such that we can solve it analytically. Assuming D to be negative (as found for a single Fe atom), its ground state has $|m_i| = 2$ for all i , while the sign of J determines whether the spins have parallel or antiparallel alignment. One can easily demonstrate that in either situation a $|\Delta m_i| = 1$ transition on the spin of an outer atom will cost $2|J| - 3D$, while the same excitation on an inner spin costs $4|J| - 3D$. Combining this with the measured excitation energies we find $|J| \simeq 1.5$ meV and $D \simeq -1.3$ meV, which is not at all unreasonable (compared to $D = -1.55$ meV for single Fe). Within this model J can in principle have either sign, although based on what we have seen above it is unlikely to become negative.

The Ising Hamiltonian presented differs in two ways from the Heisenberg model we have successfully used so far. First, only the x -components of the spins are coupled rather than all components equally, and second, $E = 0$. Changing either of these two properties only slightly would sufficiently mix the eigenstates as to allow several additional excitations that are not observed. The sudden disappearance of E might be interpreted as a first observation of magnetic atoms significantly influencing each other’s local environment (although there is no particular reason for the coupling along x to lift the difference between the y and z -directions). Most intriguing, however, is the apparent change in the nature of the coupling mechanism: from fully isotropic to strongly directional.

³In case of the dimer, Fe_{NNFe} , the step actually consists of two smaller steps. We will ignore this for now.

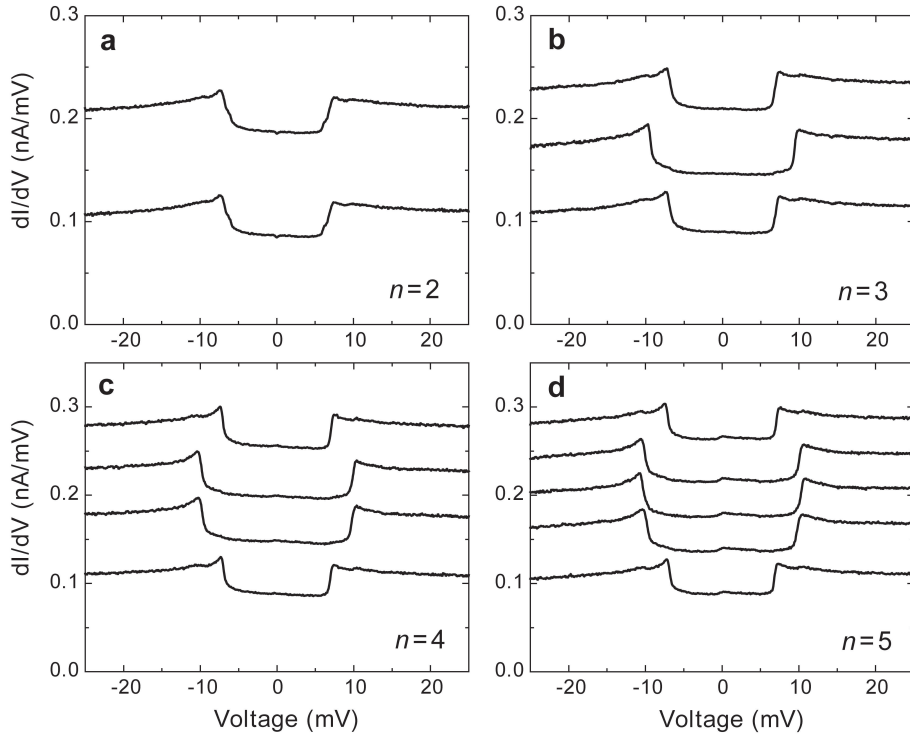


Figure 5.7: dI/dV -spectra measured over each of the Fe atoms in $\text{Fe}(\text{NNFe})_{n-1}$ structures with $n = 2, 3, 4$ and 5 . In each panel all curves except for the lowest are shifted upward by arbitrary amounts. The absolute conductance values are not relevant for the discussion presented here, but can be retrieved by considering that the integral of each spectrum up to 10 mV (quiescent voltage) should be equal. The vertical order corresponds to the positioning of the atoms within the structure (i.e. top and bottom curves were measured over the atoms on either end of the chain, etc.).

Interestingly, the results can be partly explained also *within* the framework of Heisenberg coupling by choosing J to be negative, i.e. by assuming ferromagnetic interaction. For instance in the case of the dimer ($n = 2$), the Heisenberg term does mix the $|m_1, m_2\rangle = |+2, -2\rangle$ and $|-2, +2\rangle$ states, but leaves $|+2, +2\rangle$ and $|-2, -2\rangle$ unchanged. This would justify the absence of a low-energy excitation, although additional excitations towards $|m_i| = 1$ states should still be expected.

Isn't the interpretation of ferromagnetic coupling inconsistent with the discussion on RKKY interaction of the previous section? After all, the separation distance is still 7.2 Å which according to fig. 5.5 should result in a positive J . Yes, but that graph is based on coupling along the v-row, and its resulting value for k_F is significantly lower than expected based on the lattice constant (which is equal to the bulk copper lattice constant). Possibly the anisotropy of the Fermi surface of Cu_2N is such that along the N-row k_F is much closer to the

value for bulk copper. In that case, at a distance of two lattice spacings we could already have reached the first negative part of the RKKY oscillation. A similar study of the distance dependence of the coupling along the N-row may help verify this. For starters: at 3.6 Å separation along the N-row the interaction between Mn atoms was found to be antiferromagnetic ($J = 6.2$ meV) [19].

5.2.2 Closure of the Inelastic Channel

⁴ Even more challenging are the results obtained on the $\text{Co}_{(\text{NNCo})_{n-1}}$ structures as shown in fig. 5.8. First of all, not a single Kondo peak is observed in any of the spectra. Second, the results for $n = 2$ are dramatically different from those for $n \geq 3$, in which case there is again a sharp distinction between spectra taken on inner and on outer atoms. But the most surprising is that the spectra corresponding to inner atoms appear to be completely flat. Additional measurements on these atoms up to ± 100 mV did not show any feature, other than a gradual rise in the dI/dV for negative voltage and perhaps two very weak bumps around -10 mV and $+30$ mV.

The excitations measured on the dimer Co_{NNCo} can be modelled reasonably successfully using a $J \simeq 3.2$ meV Heisenberg model⁵, but this is certainly not the case for any of the other spectra. Regardless of what values are chosen for all the spin parameters, there should always be at least one excitation having a large enough transition intensity based on (3.4) to be observed. So it seems like the excitations themselves are still possible, but that they cannot be accessed for a different reason.

It is important to observe that even on the inner atoms the elastic part of the conductance is still fully intact. This can be derived from fig. 5.6f showing the height profile of $\text{Co}_{(\text{NNCo})_4}$ taken at 10 mV: if the elastic conductance would have been suppressed, the three inner atoms would have appeared significantly smaller in topography. This means that whatever process is responsible for disabling the spin excitations, is selective and only applies to the inelastic conductance. Let us therefore look more closely into the mechanism of inelastic spin excitation. On a Co atom, the net spin is carried by the 7 electrons in the $3d$ -states which are localized relatively closely around the nucleus, while most elastic conductance is expected to pass through the more widely spread s and p -states. In order to make an inelastic spin excitation, conduction electrons from the tip may have to tunnel into one of the five $3d$ -states. Of these only $3d_{z^2}$ has a finite electron density straight above the atom, where as usual we choose z to be oriented perpendicular to the sample-surface. The others (i.e. $3d_{xy}$, $3d_{xz}$, $3d_{yz}$ and $3d_{x^2-y^2}$) all have nodes along the z -axis.

⁴The interpretation presented in this section was based on discussions with J. van den Brink and J. van Wezel.

⁵Choosing $D = -2.3$ meV and $E = 0.6$ meV reconstructs the energies of all four excitations as well as much of their relative intensities. Interestingly, the system appears to have changed from hard-axis anisotropy along y for single Co into a configuration with an easy-axis (presumably perpendicular to y). This might explain the sudden absence of Kondo behavior (see section 4.2.2). However, as these findings are not too relevant for the discussion in this section, they will not be presented in more detail.

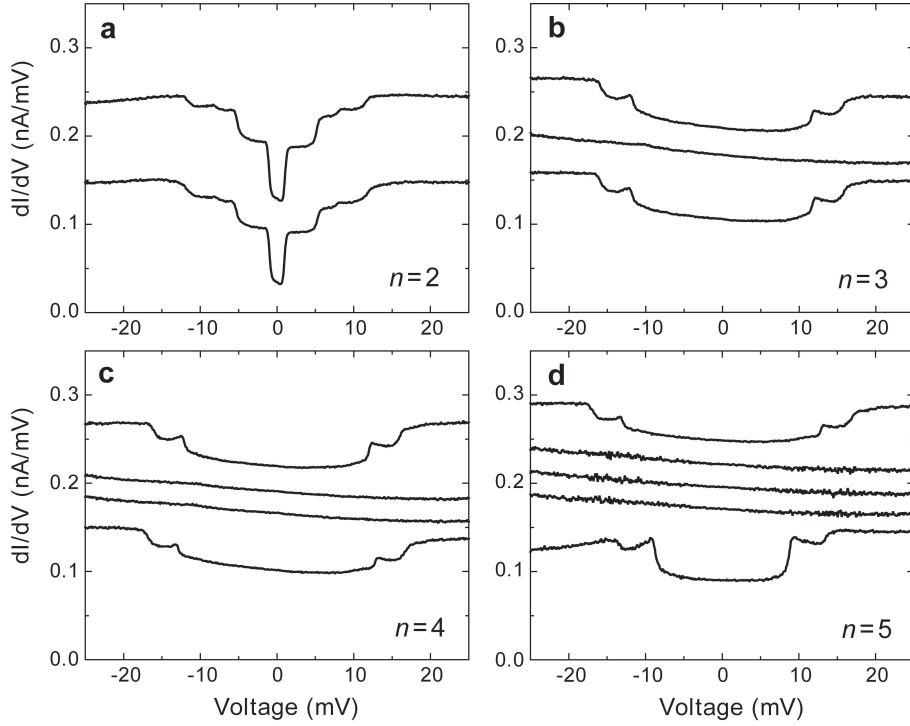


Figure 5.8: dI/dV -spectra measured over each of the Co atoms in $\text{Co}(\text{NNCo})_{n-1}$ structures with $n = 2, 3, 4$ and 5 ($10 \text{ mV}/1 \text{ nA}$ quiescent). In each panel all curves except for the lowest are shifted upward by arbitrary amounts. As before, the vertical order corresponds to the positioning of the atoms within the structure.

In this context the suppression of the excitations could – by way of speculation – be interpreted as a rearrangement of the $3d$ -orbitals due to spin coupling causing the $3d_{z^2}$ -state to shift away from the Fermi energy, thus becoming inaccessible for conduction electrons. Another way of looking at this is that the orbitals have rotated such that there no longer is a $3d_{z^2}$ -state (having been replaced by e.g. $3d_{x^2}$): now all orbitals have a node along z . None of this happens on the outer atoms as these are coupled to only one neighbor, leading to a different rearrangement of the orbitals. An obvious experiment to test this hypothesis would be to do spectroscopy while the tip is displaced horizontally with respect to the atom. Due to our automated atom-locking procedure (section 2.3.1), all present measurements were performed straight above the atom. If proven correct, this insight tells us that the $3d$ -orbitals play a prominent role in, or are at least strongly influenced by, the process of spin-spin coupling.

In the inner spectra of $\text{Co}(\text{NNCo})_4$ (fig. 5.8d) a remarkable noise is observed between 10 and 20 mV , symmetric around zero voltage. It is possible that this is somehow related to the excitations that are (supposedly) suppressed, although one can only speculate as to what mechanism is behind this.

5.3 Single-Atom Spin Filter

The art of filtering tunneling electrons based on their magnetic polarization was experimentally realized first by means of a ferromagnetic, or ferromagnetically coated tip [13]. This tool greatly expanded the scope of STM by making the magnetic structure of various surfaces directly visible [86, 87]. Further improvement to the technique was made through the introduction of antiferromagnetic tips [14], which strongly reduced the disturbing influence of the probe's dipolar stray field. In this section we will discuss an initial attempt towards the creation of the ultimate spin filter: a single magnetic atom attached to the apex of a non-magnetic tip.

Figure 5.9 shows the influence of a Co atom at the apex of the tip on its spectroscopic qualities. For this experiment a tip was formed (by repeated poking) that could reliably pick up and drop off atoms (section 2.3.3), each time reproducing the same atomic-scale tip geometry as seen from topography. With the tip in its 'empty' state a Cu atom (that could be identified as such

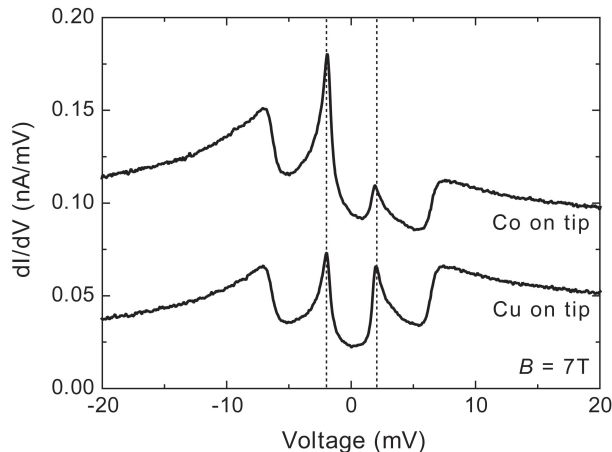


Figure 5.9: dI/dV -spectra taken over the same Co atom both before (lower curve) and after (upper curve) the Cu atom at the tip apex was replaced by a Co atom, at $B = 7$ T oriented out-of-plane. The lower spectrum was shifted down by 0.05 nA/mV.

through methods described in chapter 2) was picked up after which a standard spectrum at $B = 7$ T was taken over a Co atom, resulting in the lower curve. Next the Cu atom was replaced by a Co atom, with which the upper spectrum was taken over the same Co atom as before. The effect is striking: whereas for the neutral tip the two resonance peaks are equally high, with the magnetic tip the ratio of their heights is almost 4 : 1, while their position is not affected.

Although clearly the symmetry between the two spin polarizations is somehow broken, it is not easy to find a solid explanation for this phenomenon. It is tempting to say that if only electrons with one polarization (say \downarrow) are available

at the tip, these can tunnel into only one of the two resonances of the Kondo system. But as we have seen in section 4.3, the distinction between the two peaks is not at all made by spin polarization (\uparrow vs \downarrow), but by the fact that one belongs to the electron DOS and the other to the hole DOS. In each of the two resonances the localized spin continuously flips between either of the two excited states: \uparrow (with an electron-hole pair in the Fermi sea) and \downarrow (with the Fermi sea unexcited). Seeing that the ground state is \uparrow with an unexcited Fermi sea, arguably only the second of these excitations is directly accessible for electrons tunneling from the tip into the localized spin. Assuming that this can only be done by \downarrow electrons, the electron-hole symmetry might be broken in the case of a spin-selective tip.

A few points worth mentioning are that (1) the regular excitation steps in fig. 5.9 do not seem to be influenced too much by the magnetic tip (these are the excitations to $m = \pm\frac{3}{2}$) and that (2) the asymmetry of the peaks appears to be independent of field strength. Even at 2 T, the smallest field where the two peaks can still be discerned (not shown), the height ratio is close to 4 : 1.

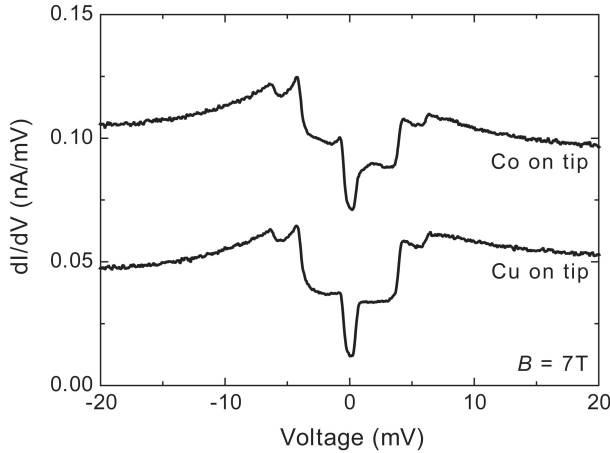


Figure 5.10: dI/dV -spectra taken over the same Fe atom both before (lower curve) and after (upper curve) the Cu atom at the tip apex was replaced by a Co atom, at $B = 7$ T oriented out-of-plane. The lower spectrum was shifted down by 0.05 nA/mV.

Interestingly, when doing the same experiment over an Fe atom as shown in fig. 5.10, the inner steps (between $|m| = 2$ states, see section 3.3.2) do become asymmetric, while those around 5 mV ($|m| = 2 \rightarrow 1$) seem to be unaltered. This is not at all surprising in view of that fact that the $|m| = 1$ states are mixed much stronger by the transverse anisotropy parameter E than those with $|m| = 2$, and have thereby lost much of their spin polarization (see table 3.1).

An intriguing situation occurs also when studying the Fe_{v_v}Co and Mn_{v_v}Co structures of chapter 4 with the Co-ended tip (fig. 5.11). In either case at strong fields it is the peak at negative tip-voltage that is highest, as we saw for the

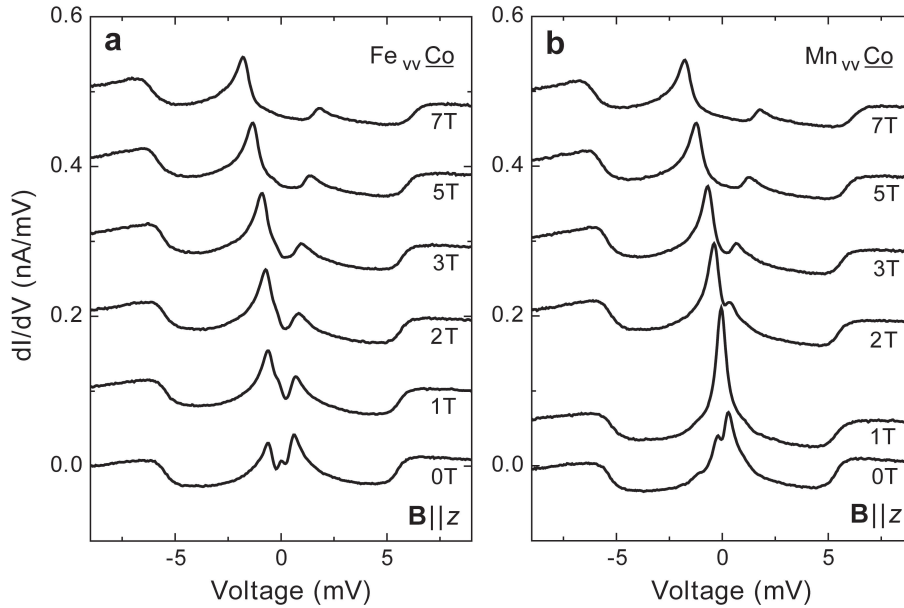


Figure 5.11: dI/dV -spectra measured over the Co atoms of $\text{Fe}_{\text{vv}}\text{Co}$ (a) and $\text{Mn}_{\text{vv}}\text{Co}$ (b) at various fields oriented along z (i.e. out-of-plane). The measurements were performed with the same Co-ended tip as used in fig. 5.9. Although this tip significantly alters the peak heights, their positions as well as those of the steps (being used for analysis in chapter 4) are not expected to be influenced by it. All non-zero field spectra are shifted for clarity.

single Co atom. But at low field strengths, e.g. in case of $\text{Mn}_{\text{vv}}\text{Co}$ below the point where the ground state changes to antiparallel around 1 T, suddenly the positive-voltage peak becomes dominant: the Co spin has flipped around.

The anomalous spectroscopic asymmetry presented in this section was occasionally encountered also when other magnetic atoms (Mn or Fe) were picked up instead of Co. In one instance it even was the neutral tip (i.e. with a Cu atom) that showed this behavior, albeit weaker, while the same tip with a Co atom produced symmetric spectra. This might have been caused by a second magnetic atom being incorporated in the tip structure close to the apex, such that its effects were cancelled when another magnetic atom was picked up.

All these tips could prove to be highly valuable spin filters, in the sense that the filtering aspect can be switched on or off simply by replacing the last atom. However, one thing we haven't considered at all is the question how strongly they are magnetized. A spin-polarized tip is hardly useful if the least stray field induced by the sample below it would reverse its filter. In order to answer this question, we should basically repeat the kind of experiments discussed in chapter 3 – to determine the magnetic anisotropy energies of an atomic spin in a certain environment – with the roles of tip and sample inverted.

5.4 Closing Remarks

The preliminary findings presented in this chapter demonstrate how we have only barely begun exploring the richness of this fascinating experimental system. Clearly spin excitation spectroscopy is a fantastic tool and Cu_2N an almost perfect study object to use it on. Among the countless parameters that one can tune during further experiments are the length and direction of the vector separating coupled spins, as well as the size, geometry and composition of larger spin structures. Additionally several other d -shell magnetic elements such as Ti, Cr and Ni can be studied to verify or expand our hypotheses on magnetic anisotropy and Kondo-screening for various values of S .

But why limit ourselves to Cu_2N ? There are bound to be numerous other surfaces just as useful for performing spin excitation spectroscopy experiments. While the square lattice of Cu_2N was found to be exquisite for anisotropy measurements, surfaces with a threefold symmetry such as triangular or hexagonal lattices might be ideal for building circular spin chains. Especially when anti-ferromagnetic rings can be constructed that contain an odd number of atoms, all sorts of spin frustration effects might be observed.

From a technological viewpoint it may be worthwhile to search for surfaces that present an even stronger magnetic anisotropy, allowing stable atomic bits to be realized at higher temperatures. In this respect it is important to understand as much as possible of the surface molecular network of Cu_2N and the impact it has on the orientation of atomic spins incorporated into the network, as well as its possibilities for coupling spins ferromagnetically.

The concept *spectroscopy* is used very widely throughout experimental physics. Auger spectroscopy, NMR spectroscopy, Raman spectroscopy and spectroscopy of visible and UV light absorption by atoms are only a few of the many examples. While their underlying mechanisms are quite different, all these techniques are based on the same general principle: to characterize a system by observing not only in what state it happens to be, but also what excitations can be made to it. With the developments of inelastic electron tunneling spectroscopy and spin excitation spectroscopy, similar characterization can now be performed in combination with the fabulous spatial resolution that only an STM can provide.

Bibliography

- [1] R. P. Feynman, *There's Plenty of Room at the Bottom*, California Institute of Technology, Pasadena, CA, December 29th 1959.
- [2] D. M. Eigler and E. K. Schweizer, *Nature* **344**, 524 (1990).
- [3] J. A. Stroschio and D. M. Eigler, *Science* **254**, 1319 (1991).
- [4] G. Binnig, H. Rohrer, C. Gerber, and E. Weibel, *Phys. Rev. Lett.* **50**, 120 (1983).
- [5] M. F. Crommie, C. P. Lutz, and D. M. Eigler, *Science* **262**, 218 (1993).
- [6] A. J. Heinrich, C. P. Lutz, J. A. Gupta, and D. M. Eigler, *Science* **298**, 1381 (2002).
- [7] B. E. Kane, *Nature* **393**, 133 (1998).
- [8] S. A. Wolf, D. D. Awschalom, R. A. Buhrman, J. M. Daughton, S. von Molnar, M. L. Roukes, A. Y. Chtchelkanova, and D. M. Treger, *Science* **294**, 1488 (2001).
- [9] J. M. Elzerman, R. Hanson, L. H. W. van Beveren, B. Witkamp, L. M. K. Vandersypen, and L. P. Kouwenhoven, *Nature* **430**, 431 (2004).
- [10] F. H. L. Koppens, C. Buizert, K. J. Tielrooij, I. T. Vink, K. C. Nowack, T. Meunier, L. P. Kouwenhoven, and L. M. K. Vandersypen, *Nature* **442**, 766 (2006).
- [11] Y. Manassen, R. J. Hamers, J. E. Demuth, and A. J. Castellano, *Phys. Rev. Lett.* **62**, 2531 (1989).
- [12] D. Rugar, R. Budakian, H. J. Mamin, and B. W. Chui, *Nature* **430**, 329 (2004).
- [13] M. Bode, M. Getzlaff, and R. Wiesendanger, *Phys. Rev. Lett.* **81**, 4256 (1998).
- [14] A. Kubetzka, M. Bode, O. Pietzsch, and R. Wiesendanger, *Phys. Rev. Lett.* **88**, 057201 (2002).

- [15] R. C. Jaklevic and J. Lambe, *Phys. Rev. Lett.* **17**, 1139 (1966).
- [16] B. C. Stipe, M. A. Rezaei, and W. Ho, *Science* **280**, 1732 (1998).
- [17] R. H. M. Smit, Y. Noat, C. Untiedt, N. D. Lang, M. C. van Hemert, and J. M. van Ruitenbeek, *Nature* **419**, 906 (2002).
- [18] A. J. Heinrich, J. A. Gupta, C. P. Lutz, and D. M. Eigler, *Science* **306**, 466 (2004).
- [19] C. F. Hirjibehedin, C. P. Lutz, and A. J. Heinrich, *Science* **312**, 1021 (2006).
- [20] C. F. Hirjibehedin, C. Y. Lin, A. F. Otte, M. Ternes, C. P. Lutz, B. A. Jones, and A. J. Heinrich, *Science* **317**, 1199 (2007).
- [21] J. Wiebe, A. Wachowiak, F. Meier, D. Haude, T. Foster, M. Morgenstern, and R. Wiesendanger, *Rev. Sci. Instr.* **75**, 4871 (2004).
- [22] H.-J. Güntherodt and R. Wiesendanger, *Scanning Tunneling Microscopy I* (Springer Verlag, Berlin/Heidelberg, 1992).
- [23] S. H. Pan, International Patent Publication Number WO 93/19494 (International Bureau, World Intellectual Property Organization), 30 September 1993.
- [24] S. H. Pan, E. W. Hudson, and J. C. Davis, *Review Of Scientific Instruments* **70**, 1459 (1999).
- [25] G. J. C. van Baarle, *Vortices in Superconductors Imaged by Scanning Tunneling Microscopy* (PhD Thesis, Leiden University, Leiden, 2005).
- [26] M. Tinkham, *Introduction to Superconductivity* (McGraw Hill, New York, 1996).
- [27] G. K. White, *Experimental Techniques in Low-Temperature Physics* (Clarendon Press, Oxford, UK, 1979).
- [28] J. Repp, G. Meyer, S. M. Stojkovic, A. Gourdon, and C. Joachim, *Phys. Rev. Lett.* **94**, 026803 (2005).
- [29] F. M. Leibsle, C. F. J. Flipse, and A. W. Robinson, *Phys. Rev. B* **47**, 15865 (1993).
- [30] With 2 kV acceleration voltage and emission current I_e , each target was preheated for 3 minutes after which the sample was exposed for a duration of t_e . **Mn:** $I_e = 5.0$ mA, $t_e = 75$ s; **Fe:** $I_e = 20.0$ mA, $t_e = 180$ s; **Co:** $I_e = 22.5$ mA, $t_e = 270$ s.
- [31] J. I. Pascual, N. Lorente, Z. Song, H. Conrad, and H. P. Rust, *Nature* **423**, 525 (2003).

- [32] Y. Sugimoto, P. Pou, M. Abe, P. Jelinek, R. Perez, S. Morita, and O. Custance, *Nature* **446**, 64 (2007).
- [33] L. Bartels, G. Meyer, and K. H. Rieder, *Phys. Rev. Lett.* **79**, 697 (1997).
- [34] J. A. Stroschio and R. J. Celotta, *Science* **306**, 242 (2004).
- [35] N. Nilius, T. M. Wallis, and W. Ho, *Science* **297**, 1853 (2002).
- [36] D. M. Eigler, C. P. Lutz, and W. E. Rudge, *Nature* **352**, 600 (1991).
- [37] M. Brandbyge and P. Hedegard, *Phys. Rev. Lett.* **72**, 2919 (1994).
- [38] R. L. White, *J. Mag. Mag. Mat.* **209**, 1 (2000).
- [39] P. Gambardella, S. Rusponi, M. Veronese, S. S. Dhési, C. Grazioli, A. Dallmeyer, I. Cabria, R. Zeller, P. H. Dederichs, K. Kern, C. Carbone, and H. Brune, *Science* **300**, 1130 (2003).
- [40] M. Bode, O. Pietzsch, A. Kubetzka, and R. Wiesendanger, *Phys. Rev. Lett.* **92**, 067201 (2004).
- [41] R. Sessoli, D. Gatteschi, A. Caneschi, and M. A. Novak, *Nature* **365**, 141 (1993).
- [42] J. R. Long, in: P. Yang, *Chemistry of Nanostructured Materials* (World Scientific Publishing, Hong Kong, 2003), pp. 241–315.
- [43] D. Gatteschi, R. Sessoli, and J. Villain, *Molecular Nanomagnets* (Oxford University Press, Oxford, UK, 2006).
- [44] P. Blaha, K. Schwarz, G. Madsen, D. Kvasnicka, J. Luitz, WIEN2k (Technische Univ. Wien, Vienna, 1999).
- [45] J. P. Perdew, K. Burke, and M. Ernzerhof, *Phys. Rev. Lett.* **77**, 3865 (1996).
- [46] The surface was simulated by a supercell of 5-layer slabs (7-layers for bare CuN) separated by 8 vacuum layers. Each slab had the CuN monolayers on both sides and three Cu layers in between (5 layers of Cu for bare CuN). Fe or Mn atoms were located on top of the CuN surface at 10.8 Å lateral separation. The crystal structure was optimized until the forces acting on any atom were below 10 mRy/ a_0 , where a_0 is the Bohr radius. From the calculated electronic states of the optimized structure, the charge on each atom was obtained by Bader analysis [47].
- [47] R. F. W. Bader, *Atoms in Molecules: A Quantum Theory* (Clarendon Press, Oxford, UK, 1994).
- [48] A. V. Postnikov, J. Kortus, and M. R. Pederson, *Phys. Stat. Sol. B* **243**, 2533 (2006).

- [49] J. Krzystek, A. Ozarowski, and J. Telsner, *Coord. Chem. Rev.* **250**, 2308 (2006).
- [50] S. Y. Ohno, K. Yagyu, K. Nakatsuji, and F. Komori, *Surf. Sci.* **547**, L871 (2003).
- [51] R. Caciuffo, G. Amoretti, A. Murani, R. Sessoli, A. Caneschi, and D. Gatteschi, *Phys. Rev. Lett.* **81**, 4744 (1998).
- [52] J. Lambe and R. C. Jaklevic, *Physical Review* **165**, 821 (1968).
- [53] A. Kogan, S. Amasha, D. Goldhaber-Gordon, G. Granger, M. A. Kastner, and H. Shtrikman, *Phys. Rev. Lett.* **93**, 166602 (2004).
- [54] W. J. de Haas and G. J. van den Berg, *Physica* **3**, 440 (1936).
- [55] J. Kondo, *Phys. Rev.* **169**, 437 (1968).
- [56] P. W. Anderson, *Phys. Rev.* **124**, 41 (1961).
- [57] J. R. Schrieffer and P. A. Wolff, *Phys. Rev.* **149**, 491 (1966).
- [58] A. C. Hewson, *The Kondo Problem to Heavy Fermions* (Cambridge University Press, Cambridge, UK, 1997).
- [59] D. Goldhaber-Gordon, H. Shtrikman, D. Mahalu, D. Abusch-Magder, U. Meirav, and M. A. Kastner, *Nature* **391**, 156 (1998).
- [60] S. M. Cronenwett, T. H. Oosterkamp, and L. P. Kouwenhoven, *Science* **281**, 540 (1998).
- [61] W. G. van der Wiel, S. De Franceschi, T. Fujisawa, J. M. Elzerman, S. Tarucha, and L. P. Kouwenhoven, *Science* **289**, 2105 (2000).
- [62] N. J. Craig, J. M. Taylor, E. A. Lester, C. M. Marcus, M. P. Hanson, and A. C. Gossard, *Science* **304**, 565 (2004).
- [63] R. M. Potok, I. G. Rau, H. Shtrikman, Y. Oreg, and D. Goldhaber-Gordon, *Nature* **446**, 167 (2007).
- [64] V. Madhavan, W. Chen, T. Jamneala, M. F. Crommie, and N. S. Wingreen, *Science* **280**, 567 (1998).
- [65] J. T. Li, W. D. Schneider, R. Berndt, and B. Delley, *Phys. Rev. Lett.* **80**, 2893 (1998).
- [66] P. Wahl, L. Diekhoner, M. A. Schneider, L. Vitali, G. Wittich, and K. Kern, *Phys. Rev. Lett.* **93**, 176603 (2004).
- [67] J. Nygard, D. H. Cobden, and P. E. Lindelof, *Nature* **408**, 342 (2000).
- [68] T. W. Odom, J. L. Huang, C. L. Cheung, and C. M. Lieber, *Science* **290**, 1549 (2000).

- [69] P. Jarillo-Herrero, J. Kong, H. S. J. van der Zant, C. Dekker, L. P. Kouwenhoven, and S. De Franceschi, *Nature* **434**, 484 (2005).
- [70] J. Park, A. N. Pasupathy, J. I. Goldsmith, C. Chang, Y. Yaish, J. R. Petta, M. Rinkoski, J. P. Sethna, H. D. Abruna, P. L. McEuen, and D. C. Ralph, *Nature* **417**, 722 (2002).
- [71] W. J. Liang, M. P. Shores, M. Bockrath, J. R. Long, and H. Park, *Nature* **417**, 725 (2002).
- [72] U. Fano, *Phys. Rev.* **124**, 1866 (1961).
- [73] K. Nagaoka, T. Jamneala, M. Grobis, and M. F. Crommie, *Phys. Rev. Lett.* **88**, 077205 (2002).
- [74] M. Ternes, *Scanning Tunneling Spectroscopy at the Single Atom Scale* (PhD Thesis N° 3465, École Polytechnique Fédérale de Lausanne, Lausanne, 2006).
- [75] A. Messiah, *Quantum Mechanics II* (North-Holland Publishing Co., Amsterdam, 1961).
- [76] O. Ujsaghy, A. Zawadowski, and B. L. Gyorffy, *Phys. Rev. Lett.* **76**, 2378 (1996).
- [77] C. Romeike, M. R. Wegewijs, W. Hofstetter, and H. Schoeller, *Phys. Rev. Lett.* **96**, 196601 (2006).
- [78] Y. Meir, N. S. Wingreen, and P. A. Lee, *Phys. Rev. Lett.* **70**, 2601 (1993).
- [79] J. E. Moore and X. G. Wen, *Phys. Rev. Lett.* **85**, 1722 (2000).
- [80] H. Jeong, A. M. Chang, and M. R. Melloch, *Science* **293**, 2221 (2001).
- [81] H. B. Heersche, Z. de Groot, J. A. Folk, L. P. Kouwenhoven, H. S. J. van der Zant, A. A. Houck, J. Labaziewicz, and I. L. Chuang, *Phys. Rev. Lett.* **96**, 017205 (2006).
- [82] R. I. Nepomechie, *A Spin Chain Primer*, arXiv:hep-th 9810032 v1 (1998).
- [83] H. Tsunetsugu, M. Sigrist, and K. Ueda, *Rev. Mod. Phys.* **69**, 809 (1997).
- [84] M. G. Vavilov and L. I. Glazman, *Phys. Rev. Lett.* **94**, 086805 (2005).
- [85] C. Kittel, *Quantum Theory of Solids* (Wiley, New York, 1987), pp. 360–363.
- [86] S. Heinze, M. Bode, A. Kubetzka, O. Pietzsch, X. Nie, S. Blugel, and R. Wiesendanger, *Science* **288**, 1805 (2000).
- [87] M. Kleiber, M. Bode, R. Ravlic, and R. Wiesendanger, *Phys. Rev. Lett.* **85**, 4606 (2000).

Samenvatting

Vrijwel alle eigenschappen die een vaste stof maken tot wat het is vinden hun grondslag op de schaal van de kleinste bouwsteen waaruit die stof is opgebouwd: het atoom. Dit geldt bijvoorbeeld voor soortelijke warmte (hoe makkelijk de atomen in trilling kunnen worden gebracht) en elektrische weerstand (in hoeverre ze hun elektronen loslaten), maar ook voor heel basale kenmerken als hardheid (hoe stevig de atomen aan elkaar gebonden zijn) en kleur (welke golflengten van het licht hun elektronen kunnen opnemen en welke niet). Een eigenschap die hier zonder meer bij hoort is magnetisme.

Of een atoom magnetisme kan vertonen wordt bepaald door de opvulling van de elektronschillen in het atoom. Ieder elektron heeft een gelijke hoeveelheid *spin*, de drager van magnetisme, maar in volledig opgevulde schillen heffen de spins van de elektronen elkaar exact op. Ook in het geval van deels gevulde schillen is magnetisme vaak uitgesloten doordat de overgebleven spin wordt ‘verbruikt’ in een chemische binding met een buuratoom. Niettemin is er een aantal atomen dat één of meer ongecompenseerde spins heeft, veelal door een onvolledig gevulde *d*-schil. Hiervan zijn ijzer, kobalt en nikkel de meest bekende voorbeelden, hoewel o.a. ook titanium en mangaan ertoe behoren.

De experimenten die in dit proefschrift worden beschreven laten zien hoe het magnetisme van één enkel atoom toegankelijk kan worden gemaakt – in eerste instantie voor wetenschappelijke studie maar op lange termijn wellicht ook voor technologische doeleinden. Toegang tot individuele atomen is al enige tijd mogelijk dankzij de ontwikkeling van de *Scanning Tunneling Microscope* (STM) in 1981. Hierin worden atomen afgetast door een scherpe naald waarmee ze niet alleen kunnen worden waargenomen, maar zelfs met uiterste precisie kunnen worden verplaatst. Dit revolutionaire instrument – de uitvinders Binnig en Rohrer ontvingen al in 1986 de Nobelprijs – vormt samen met de daarvan afgeleide *Atomic Force Microscope* (AFM) het voornaamste gereedschap voor nanotechnologisch onderzoek.

Om vervolgens ook de spin van een atoom te detecteren gebruiken we een veel recenter techniek (2004), Spin Excitatie Spectroscopie. Deze techniek is gebaseerd op een vertrouwd principe: magnetisme is weliswaar niet direct zichtbaar, maar je kunt het wel ‘voelen’. Door een alledaagse magneet op verschillende manieren uit zijn rusttoestand te halen (bijvoorbeeld door deze los te trekken van een koelkastdeur of op een andere magneet rond te draaien) en steeds te registreren hoeveel moeite dat kost (of fysisch: hoeveel arbeid daar-

voor moet worden verricht), kun je na enige inspanning een beeld vormen van zowel de magnetisatiesterkte als -richting van deze magneet. Iets soortgelijks kunnen we doen met een atomaire spin, hoewel er één belangrijk verschil is: doordat een spin zich gedraagt volgens de wetten van de quantummechanica is het aantal excitatiemogelijkheden beperkt. Met andere woorden, een spin kan niet op iedere willekeurige manier uit zijn grondtoestand worden gehaald, maar slechts via een paar exact gedefiniëerde overgangen. Deze eigenschap blijkt bijzonder goed van pas te komen om een nauwkeurig kwantitatief inzicht te krijgen in het gedrag van een spin.

Spin Excitatie Spectroscopie werkt als volgt. Een magnetisch atoom wordt op een dunne (één atoomlaag dik) isolerende laag geplaatst die het atoom scheidt van een metallische ondergrond. Hierdoor wordt voorkomen dat het atoom al te veel hybridiseert met de geleidingselektronen in het metaal, zodat het karakter van een geïsoleerde spin behouden blijft. Vervolgens wordt de STM-naald vlak boven het atoom gepositioneerd (slechts enkele tienden van een nanometer) waardoor elektronen vanuit de naald naar het atoom kunnen ‘tunnelen’. Door nu een steeds groter spanningsverschil aan te leggen tussen de naald en het oppervlak waarop het atoom ligt, nemen elektronen met steeds meer energie deel aan deze tunnelstroom. Op een gegeven moment hebben de elektronen voldoende energie beschikbaar om een door de quantummechanica toegestane excitatie van de spin op het atoom uit te voeren, hetgeen resulteert in een plotselinge verandering (doorgaans een toename) in de elektrische geleiding. Door te registreren bij welke spanningen dit gebeurt, kunnen we de energieën van zulke excitaties achterhalen. Bij deze toegestane excitaties gaat het overigens altijd om gehele of gedeeltelijke rotaties van de spin.

Dit alles vindt plaats bij extreem lage temperatuur. Hiervoor zijn twee redenen: allereerst om ervoor te zorgen dat de atomen op hun plaats blijven liggen, en ten tweede om een voldoende hoge energieresolutie te garanderen. Door de temperatuur te verlagen beperken we de spreiding in elektronenergiën waardoor er een zo eenduidig mogelijke relatie tussen spanning en energie ontstaat. Aangezien verschillende spinexcitaties in sommige gevallen minder dan 1 meV uit elkaar liggen is een hoge resolutie van groot belang. De experimenten in dit proefschrift werden uitgevoerd bij een temperatuur van 0.5 K in een speciale STM die wordt gekoeld met behulp van vloeibaar helium-3, de lichtere variant van helium. In **hoofdstuk 1** worden twee van dit soort apparaten beschreven.

Als ondergrond voor onze spin-excitatie experimenten gebruikten we een mono-atomaire laag kopernitride (Cu_2N) die gegroeid was op Cu(100), één van de facetten van een koperkristal. De karakterisatie van dit oppervlak is het onderwerp van **hoofdstuk 2**. Cu_2N blijkt om verschillende redenen bijzonder geschikt te zijn: het is relatief eenvoudig te prepareren en de dikte van de scheidingslaag biedt een ideale combinatie van enerzijds ontkoppeling en anderzijds transparantie voor geleidingselektronen, wat van groot belang is voor het goed functioneren van de STM. Daarnaast binden atomen van de magnetische elementen ijzer (Fe), mangaan (Mn) en kobalt (Co), die in onze experi-

menten centraal staan, uiterst reproduceerbaar op specifieke lokaties op Cu_2N (namelijk precies bovenop de Cu atomen) en kunnen ze eenvoudig worden verplaatst zonder het oppervlak te beschadigen. Dit laatste is overigens zeker niet vanzelfsprekend: bijna twee decennia na de eerste succesvolle demonstratie van ‘atoom-manipulatie’ is slechts een handvol oppervlakken bekend waarop atomen betrouwbaar kunnen worden rondgeschoven.

Hoofdstuk 3 staat in het teken van de magneto-kristallijne anisotropie die atomen ondervinden wanneer zij op Cu_2N worden geplaatst. Anisotropie speelt een belangrijke rol in magnetisme. Als een spin zich in een volledig isotrope omgeving bevindt zijn alle richtingen gelijk en kan het onmogelijk een magnetisatie-as kiezen. Er is dan geen noord- of zuidpool en dus ook geen magnetisme. Pas als de isotropie wordt verbroken – bijvoorbeeld door de aanwezigheid van een kristalstructuur – kan er sprake zijn van een voorkeursrichting voor magnetisatie. Ook hiervoor blijkt Cu_2N ideaal: een atoom dat bovenop één van de Cu atomen van Cu_2N is gebonden heeft in de ene richting twee stikstof (N) atomen als burens terwijl in de richting loodrecht daarop het atoom wordt begrensd door twee ‘vacatures’ (plekken in het oppervlak waar atomen lijken te ontbreken). Hierdoor wordt de lokale omgeving anisotroop.

Door de spin-excitaties van Fe en Mn atomen in deze situatie te bestuderen, en met name door te onderzoeken hoe de energieën van deze excitaties veranderen wanneer we een magnetisch veld aanleggen langs de verschillende symmetrieassen van het kristal, kunnen we de magnetische anisotropie in kaart brengen. Ook kunnen we de exacte hoeveelheid spin op het atoom vaststellen. Zo blijkt het dat een Mn atoom een spinwaarde van $\frac{5}{2}$ heeft (ofwel 5 ongecompenseerde elektronspins in de *d*-schil) die hij bij voorkeur loodrecht op het Cu_2N oppervlak richt, hoewel deze voorkeur erg licht is. Een veel sterker anisotropie-effect doet zich voor bij Fe met een spinwaarde van 2 (4 elektronspins). Hier richt de spin zich bij voorkeur in de richting van de naastgelegen N atomen en kost het behoorlijk veel energie (zo’n 6 meV) om hem 90° daarvandaan te draaien.

In beide gevallen betreft het anisotropie van het zogeheten *easy-axis* type. Dit houdt in dat één magnetisatieas geprefereerd wordt en dat het verschil in voorkeur tussen de overige twee assen relatief klein is. Dit in tegenstelling tot *hard-axis* of *easy-plane* anisotropie, waarbij de spin een uitgesproken afkeer heeft tegen één bepaalde as, maar verder weinig onderscheid maakt tussen de andere twee. Easy-axis anisotropie is de gewenste vorm voor technologische toepassingen in magnetische data-opslag, waarbij de beide polarisatierichtingen langs de voorkeurs-as de rollen van ‘0’ en ‘1’ in een bit kunnen aannemen. De spin van een Fe atoom op Cu_2N is daarmee een potentiële kandidaat voor de historische status van Eerste Atomaire Bit, hoewel de aanwezigheid van substantiële transversale anisotropie (het verschil tussen de twee overige assen) het geheel toch weer minder stabiel maakt. Ons voornaamste resultaat in deze technologische context is echter de onderzoeksmethode zelf, waarmee we demonstreren hoe de magnetische anisotropie van een atoom onomstotelijk en bovendien uiterst nauwkeurig kan worden vastgesteld.

In **hoofdstuk 4** betreden Co atomen het toneel. Deze onderscheiden zich van Fe en Mn doordat ze naast de inmiddels vertrouwde spinexcitatie stappen een scherpe resonantiepiek vertonen rond het nulniveau van de tunnelspanning. Deze resonantie schrijven we toe aan het Kondo effect: een complex samenspel van een plaatselijke spin (het Co atoom) en de collectieve spin van de geleidings-elektronen in een metaal (het onderliggende koper). Omdat het Kondo effect een ‘veel deeltjes’ effect is – alle naburige geleidings-elektronen doen er immers aan mee – is het ontzettend moeilijk een eenvoudige inzichtelijke beschrijving ervan te geven. Feitelijk komt het erop neer dat bij voldoende lage temperatuur het Co atoom er baat bij heeft voortdurend zijn ongecompenseerde elektron in te ruilen voor een elektron met tegengestelde spin waardoor deze onophoudelijk lijkt om te klappen. Het Kondo effect intrigeert wetenschappers al decennia lang en een goed begrip ervan is essentieel voor het begrijpen van magnetisme op de atomaire schaal.

In dit proefschrift richten we ons op de vraag waarom juist Co dit opmerkelijke gedrag vertoont en de andere atomen op Cu_2N niet. Om bovengenoemde resonantie mogelijk te maken moet de magnetisatie-richting omklapbaar zijn door de uitwisseling van slechts één elektron. Dit betekent dat in principe de spin niet groter dan $\frac{1}{2}$ mag zijn. Toch duiden de waargenomen spin-excitaties van Co op een grotere spin, namelijk $\frac{3}{2}$. Met behulp van de technieken uit hoofdstuk 3 kunnen we echter aantonen dat deze spin *hard-axis* anisotropie ondervindt op Cu_2N : hierdoor wordt de magnetisatie langs deze as geminimaliseerd waardoor de spinwaarde effectief reduceert tot $\frac{1}{2}$. Dit verklaart niet alleen waarom Co een Kondo resonantie heeft; het verklaart ook waarom Fe en Mn (met *easy-axis* anisotropie) het níet hebben.

Het Co atoom op Cu_2N biedt ons daarmee de unieke gelegenheid om het effect van magnetische anisotropie op een Kondo systeem te onderzoeken. Op een pure spin $\frac{1}{2}$ zou anisotropie onmogelijk invloed kunnen hebben, maar aangezien het hier feitelijk om een grotere spin gaat speelt het wel degelijk een belangrijke rol. Zo vinden we dat het aanleggen van magneetvelden langs de verschillende kristalrichtingen ook verschillende effecten in de Kondo resonantie teweeg brengt. In alle gevallen splitst de resonantiepiek in twee pieken (dat was al bekend), maar de mate van deze splitsing blijkt sterk te variëren met de veldrichting. En het interessante hierbij is dat deze richtingsafhankelijke splitsing kwantitatief kan worden beschreven enkel met behulp van eenvoudige ‘één deeltjes’ quantummechanica, dus zonder de complexiteit van het Kondo effect in rekening te brengen!

Iets soortgelijks doet zich voor wanneer een tweede spin (bijvoorbeeld een Fe atoom) op enige afstand naast het Co atoom wordt geplaatst. De spin van het Fe atoom, die zoals beschreven in hoofdstuk 3 door de kristalstructuur in een specifieke richting wordt gedwongen, creëert een effectief magnetisch veld om zich heen dat de Co spin ervaart zoals het ieder ander magnetisch veld ervaart: als opsplitsing van de Kondo resonantie. Zo kan het Co atoom gezien worden als een soort ‘nanokompas’, dat zowel de richting als sterkte van het magnetisch veld rondom één atoom lokaal kan detecteren. De juiste quantumfysische benaming voor dit verschijnsel is *exchange coupling*.

Als besluit van dit hoofdstuk presenteren we een analytisch model dat deze spinkoppeling verenigt met zowel de invloed van een extern magnetisch veld als de eerder genoemde magnetische anisotropie. Dit werkt bijzonder goed. Hoewel het aantal geëxciteerde toestanden van een gekoppelde spinstructuur veel groter is dan voor een enkele spin blijken we iedere waargenomen excitatie moeiteloos te kunnen identificeren. Hierbij maken we tevens onderscheid tussen excitaties die alleen kunnen plaatsvinden indien de STM naald zich boven het ene of juist boven het andere atoom bevindt. Dit laatste kan op termijn interessant zijn voor de ontwikkeling van een *quantum computer*, waarin het uitlezen van een enkele spin (als *quantum bit*) die deel uitmaakt van een gekoppeld spinnetwerk een essentieel onderdeel vormt.

Tot slot worden in **hoofdstuk 5** enkele open einden besproken. Om te beginnen een onderzoek naar de fysische oorsprong van de waargenomen exchange coupling tussen twee naburige spins. Door de afstand tussen de atomen te variëren vinden we de eerste aanwijzingen voor wisselwerking van het zogeheten RKKY type. Volgens dit principe is de koppeling voor verschillende afstanden afwisselend antiferromagnetisch (waarbij de spins bij voorkeur in tegengestelde richtingen wijzen) en ferromagnetisch (gelijke magnetisatie-richtingen) als gevolg van het bestaan van een korste beschikbare golflengte van de elektronen. Hoewel we een dergelijke wisseling niet direct waarnemen – de koppeling is vooralsnog enkel antiferromagnetisch – vinden we wel een bijzonder steile afname van de koppelingssterkte hetgeen een aanstaande wisseling suggereert voor iets grotere afstanden.

Ook bespreken we in dit hoofdstuk spins die langs een andere kristalrichting zijn gekoppeld (langs de N atomen in plaats van langs de vacatures). In dit geval is de wisselwerking veel sterker en vinden we bovendien een mogelijk geval van ferromagnetische koppeling tussen Fe atomen. Dit zou bijzonder interessant zijn voor de vorming van atomaire geheugenbits: door spins ferromagnetisch te koppelen zouden we de energiebarrière tussen de ‘0’ en ‘1’ toestanden kunnen verhogen terwijl we de transversale anisotropie verkleinen. Dit zou de bits veel stabiel maken zodat ze ook bij hogere temperaturen hun informatie kunnen vasthouden.

Soortgelijke koppeling langs de N atomen leidt voor Co spins in langere atoomstructuren tot een heel ander fenomeen: zowel het Kondo effect als alle spin-excitaties verdwijnen volledig! Hoewel de oorzaak hiervan volstrekt onduidelijk is, lijkt het erop dat dit het gevolg is van een verandering in het excitatiemechanisme (m.a.w., de excitaties zelf zijn nog wel mogelijk, maar niet meer toegankelijk voor tunnelende elektronen). Vervolgonderzoek hiernaar zou inzicht kunnen bieden in de rol van de verschillende elektronschillen in zowel het magnetisme van als de elektrische geleiding door atomen op Cu_2N .

We besluiten dit hoofdstuk met een poging tot het maken van een ‘spin-selectieve’ STM naald (d.w.z. een naald die enkel elektronen met één spinrichting injecteert) door het aanbrengen van een enkel magnetisch atoom aan het uiteinde van een verder niet-magnetische naald. Deze techniek zou de mogelijkheid openen om afwisselend spingevoelige en spin-ongevoelige experimenten uit

te voeren op magnetische nanosystemen. Het principe lijkt te werken, hoewel het vooralsnog onduidelijk is hoe kwetsbaar de magnetisatierichting van zulke naalden is.

Zoals de experimenten in dit proefschrift laten zien zijn technologische toepassingen van atomaire spins (data-opslag, *quantum computation*) weliswaar nog ver weg, maar zeker niet onbereikbaar. De voornaamste boodschap is echter dat eenvoudige quantummechanische spinsystemen nu relatief gemakkelijk toegankelijk zijn voor experimenteel onderzoek. De elektronspin (spin $\frac{1}{2}$) is het voorbeeldsysteem bij uitstek voor de schijnbare magie van de quantummechanica, waarbij voor iedereen de van kinds af aan zorgvuldig opgebouwde intuïtie plotseling waardeloos blijkt. De mogelijkheid om eenvoudige experimenten te doen met zo'n systeem biedt een uitstekende manier – misschien wel de enige manier – om geleidelijk een nieuwe ‘quantumintuïtie’ te ontwikkelen.

Curriculum Vitae

Alexander F. (*Sander*) Otte was born on November 24, 1979 in Ede, The Netherlands, where in 1998 he finished his secondary education at the Marnix College Gymnasium. In that same year he went to Leiden to start his studies in physics. After completing the undergraduate courses he studied the formation of metallic nanowires under the mentorship of Prof. Dr. J. M. van Ruitenbeek. He also spent several months in Prof. Dr. C. Dekker's research group at Delft Technical University, where he investigated carbon nanotubes by means of a low-temperature Scanning Tunneling Microscope (STM). In 2003 he received his MSc. degree from Leiden University averaging an 8.0 out of 10.

From June 2003 he was affiliated to Leiden University as a PhD student. Here he joined the research group of his promotor Prof. Dr. J. M. van Ruitenbeek, where he worked on the development of an STM that can be cooled down to liquid ^3He temperatures. Additionally he was involved – in cooperation with Prof. Dr. Yu. A. Kolesnichenko from the University of Kharkov, Ukraine – in the theoretical groundwork for several experiments on conductance fluctuations in metallic point-contacts. During this period he also lectured in the exercise classes belonging to an undergraduate course on quantum mechanics.

Starting November 2006 he spent six months in San Jose, CA, visiting the group of Dr. A. J. Heinrich, also copromotor, at the IBM Almaden Research Center. Using a ^3He STM he performed spin excitation experiments on individual magnetic atoms. Central theme of these experiments is the influence of crystal-field anisotropy, spin-coupling and the Kondo effect on the spins of these atoms.

List of Publications

- ◇ A. F. Otte, C. F. Hirjibehedin, K. von Bergmann, M. Ternes, C. P. Lutz, H. Brune and A. J. Heinrich – *The role of magnetic anisotropy in the Kondo effect of an atom with large spin* – Manuscript in preparation.
- ◇ C. F. Hirjibehedin, C.-Y. Lin, A. F. Otte, M. Ternes, C. P. Lutz, B. A. Jones and A. J. Heinrich – *Large magnetic anisotropy of a single atomic spin embedded in a surface molecular network* – *Science* **317**, 1199 (2007).
- ◇ Ye. S. Avotina, Yu. A. Kolesnichenko, A. F. Otte and J. M. van Ruitenbeek – *Magneto-quantum oscillations of the conductance of a tunnel point contact in the presence of a single defect* – *Phys. Rev. B* **75**, 125411 (2007).
- ◇ W. H. A. Thijssen, D. Djukic, A. F. Otte, R. H. Bremmer and J. M. van Ruitenbeek – *Vibrationally induced two-level systems in single-molecule junctions* – *Phys. Rev. Lett.* **97**, 226806 (2006).
- ◇ Ye. S. Avotina, Yu. A. Kolesnichenko, A. F. Otte and J. M. van Ruitenbeek – *Signature of Fermi-surface anisotropy in point contact conductance in the presence of defects* – *Phys. Rev. B* **74**, 085411 (2006).
- ◇ Ye. S. Avotina, Yu. A. Kolesnichenko, A. N. Omelyanchouk, A. F. Otte and J. M. van Ruitenbeek – *Method to determine defect positions below a metal surface by STM* – *Phys. Rev. B* **71**, 115430 (2005).
- ◇ A. I. Mares, A. F. Otte, L. G. Soukiassian, R. H. M. Smit and J. M. van Ruitenbeek – *Observation of electronic and atomic shell effects in gold nanowires* – *Phys. Rev. B* **70**, 073401 (2004).

Acknowledgements

First and foremost I am very thankful to the IBM Research Division for enabling me to use their facilities and resources at the Almaden Research Center between November 2006 and April 2007. In particular I would like to thank A. J. Heinrich for his generous hospitality and C. F. Hirjibehedin for the excellent advice I received from him, both during and after my rewarding visit to IBM. To M. Ternes and C. P. Lutz I am very grateful for their top quality scientific contributions and to B. Melior for his expert technical assistance. For their efforts in providing density functional calculations to help interpreting our observations I thank C.-Y. Lin and B. A. Jones.

In developing and running the ^3He STM system in Leiden I received much help from W. H. A. Thijssen, F. Galli, R. W. A. Hendrikx and J. Aarts. Special thanks go to M. J. Rost for sharing his knowledge and expertise in designing the STM scanner and to C. G. A. Pen, R. van Egmond and J. Mesman for their excellent craftsmanship in building it. I also thank G. J. C. van Baarle and R. H. M. Smit for their efforts in this project prior to my involvement.

Many people have been extremely helpful through general scientific discussions. These include, but are certainly not limited to: K. von Bergmann, H. Brune, D. M. Eigler, M. F. Crommie, J. E. Moore, A. C. Hewson, J. A. Stroscio, M. Bode, D. Rugar, S. S. P. Parkin, W.-D. Schneider, F. J. Giessibl, J. Zaanen, J. van den Brink, J. van Wezel, M. B. S. Hesselberth and many (former) members of the AMC research group, of which I would like to mention in particular Yu. A. Kolesnichenko, Ye. S. Avotina, S.-J. van der Molen, O. Tal, A. I. Yanson and M. Krieger. For granting me financial support for my visit to California I would like to acknowledge the Leiden University Fund (LUF).